LEABHARLANN CHOLÁISTE NA TRÍONÓIDE, BAILE ÁTHA CLIATH | TRINITY COLLEGE LIBRARY DUBLIN
Ollscoil Átha Cliath | The University of Dublin

Terms and Conditions of Use of Digitised Theses from Trinity College Library Dublin

Copyright statement

All material supplied by Trinity College Library is protected by copyright (under the Copyright and Related Rights Act, 2000 as amended) and other relevant Intellectual Property Rights. By accessing and using a Digitised Thesis from Trinity College Library you acknowledge that all Intellectual Property Rights in any Works supplied are the sole and exclusive property of the copyright and/or other IPR holder. Specific copyright holders may not be explicitly identified. Use of materials from other sources within a thesis should not be construed as a claim over them.

A non-exclusive, non-transferable licence is hereby granted to those using or reproducing, in whole or in part, the material for valid purposes, providing the copyright owners are acknowledged using the normal conventions. Where specific permission to use material is required, this is identified and such permission must be sought from the copyright holder or agency cited.

Liability statement

By using a Digitised Thesis, I accept that Trinity College Dublin bears no legal responsibility for the accuracy, legality or comprehensiveness of materials contained within the thesis, and that Trinity College Dublin accepts no liability for indirect, consequential, or incidental, damages or losses arising from use of the thesis for whatever reason. Information located in a thesis may be subject to specific use constraints, details of which may not be explicitly described. It is the responsibility of potential and actual users to be aware of such constraints and to abide by them. By making use of material from a digitised thesis, you accept these copyright and disclaimer provisions. Where it is brought to the attention of Trinity College Library that there may be a breach of copyright or other restraint, it is the policy to withdraw or take down access to a thesis while the issue is being resolved.

Access Agreement

By using a Digitised Thesis from Trinity College Library you are bound by the following Terms & Conditions. Please read them carefully.

I have read and I understand the following statement: All material supplied via a Digitised Thesis from Trinity College Library is protected by copyright and other intellectual property rights, and duplication or sale of all or part of any of a thesis is not permitted, except that material may be duplicated by you for your research use or for educational purposes in electronic or print form providing the copyright owners are acknowledged using the normal conventions. You must obtain permission for any other use. Electronic or print copies may not be offered, whether for sale or otherwise to anyone. This copy has been supplied on the understanding that it is copyright material and that no quotation from the thesis may be published without proper acknowledgement.

Investigation of Organic/Ferromagnet Interface and Magnetoresistive Characteristics of Small Molecule Organic Semiconductors

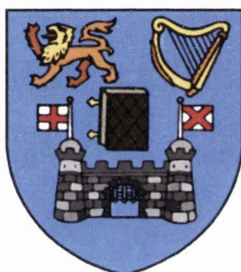

By

Huseyin Tokuc

A thesis submitted for the degree of Doctor of Philosophy

in the University of Dublin

School of Physics,

Trinity College Dublin,

August 2013

Declaration

I hereby declare that this thesis has not been submitted as an exercise for a degree in any other university.

This thesis is entirely my own work, except for the advice and assistance mentioned in the acknowledgements.

I agree to allow the library of Trinity College Dublin copy or lend a section or this entire thesis on request.

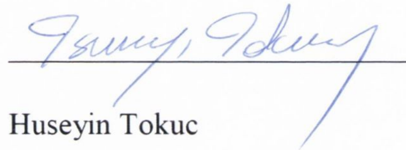

Huseyin Tokuc

29/08/2013

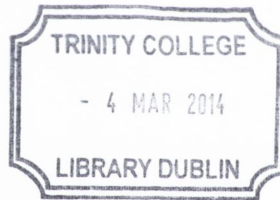

Thesis 10254

Summary

Spin injection, transport and dynamics in organic semiconductors are of growing interest as the field of organic spin electronics begins to take shape during the last decade. This new field of research aims to manipulate the electron spin degree of freedom in organic based electronic devices, such as organic-light emitting diodes, organic field effect transistors, and organic radio-frequency identification tags. Organic materials offer the promise to future lightweight, low-power, and inexpensive electronics on flexible substrates. However, to realize such device applications the fundamental processes that govern electron spin dependent injection into and transport with organic semiconductors must be understood. In general, organic semiconductors have long spin relaxation times (~ 10^{-6} s), weak hyperfine interactions, and little spin orbit scattering because the molecules are mainly composed of the elements carbon and hydrogen. However, the mobility in organics is too low, so it is unclear whether the spin-polarized electrons can travel distances over 100 nm, which is required for several device applications.

In this report, the focus is on the organic based magnetic tunnel junctions (MTJ) and quality of organic/ferromagnetic interfaces which directly govern the spin injection into organic semiconductor. The basic idea is to use organic films as a barrier between MgO or AlO_x and top ferromagnetic electrode in vertical spin valve stacks.

The interface quality of organic/ferromagnet and organic/insulator/ferromagnet multilayers were studied using a simple method called as *ferromagnetic film*

thickness magnetization (FFTM), where the organic layers are Alq_3, CuPc and Znq_2. The results clearly showed that a magnetic dead layer forms at organic/ferromagnet interface; ~ 0.9 nm for Alq_3, ~ 1nm for Znq_2, and ~ 1.3 nm for CuPc. Then, introducing an insulator layer at the organic/ferromagnet interface reduces the dead layer thickness by more than 50 %. Another remarkable observation is that the bottom ferromagnetic layer was oxidized through the organic layer when the ferromagnetic/organic bilayer was exposed to air.

Spin polarized transport properties of Alq_3, CuPc, ZnPc and Znq_2 were studied using MgO/organic and AlOx/organic based hybrid organic spin valves in a vertical structure. The stacks were fabricated using a combination of magnetron sputtering tool and an organic evaporation chamber. UV lithography and shadow masking processes were used to pattern the stacks into micron-size junctions. The key element in our lithographically patterned, exchange-biased tunnel junctions with an Alq_3 spacer layer, which enables them to exhibit useful MR at room-temperature, is the CoFeB/MgO spin injector.

Magnetoresistive characteristics of the CoFeB/MgO/organic based hybrid devices were studied and the results suggested that the devices showed better performance when the MgO layer was cleaned using Ar-ion etching before deposition of organic layer. In the case of air exposed MgO, the devices showed ~12 % MR which is independent of the Alq_3 thickness (t=2-8 nm). However, the devices showed maximum ~ 50 % MR in the presence of Alq_3 when the MgO layer was cleaned before depositing the Alq_3 layer.

Magnetotransport properties of Znq_2 and CuPc based hybrid devices were studied using an exchanged bias and bottom-pinned MTJ stack, where the barrier was air-

exposed MgO/Znq_2 (t=0-2 nm) or air-exposed MgO/CuPc (0-2 nm). In the case of Znq_2, the MR was independent of the organic thickness and ~ 15 % of MR was observed at 300 K for t = 1 and 2 nm respectively. However, the MR exhibit a strong thickness dependence when the organic was CuPc, where the MR at room temperature was 13 % and 6 % for t = 1 nm and t = 2 nm, respectively.

Magnetotransport properties of the AlO_x/organic/AlO_x based hybrid spin valves prepared by using in-situ shadow masking were studied, where the organic layer was Alq_3, CuPc, ZnPc and Znq_2. The full stack was CoFe (10 nm)/AlO_x (1.5 nm)/organic (t)/AlO_x (1.5 nm)/CoFe (18 nm). The results absolutely showed no MR at 300 K when t = 1 nm for Znq_2, ZnPc and CuPc and t=2 nm for Alq_3. The room temperature MR was 2 % for Alq_3 when t = 1 nm. At low temperature range (~ 20 K) the maximum organic thickness which showed a measurable MR signal was 3 nm for Alq_3 and 1 nm for the other organic barriers. The devices showed strong temperature dependent I-V. Furthermore, multi-step tunneling is considered to govern the transport mechanism and behaved as a source of spin precession when the electrons occupy the intermediate sites in the organic layer.

Acknowledgments

I would like to express my deepest gratitude to my supervisor Prof. Michael Coey who gave me the opportunity and the support to work in his lab and complete a PhD in Trinity College Dublin. As a supervisor, his fruitful suggestions, invaluable comments, positive attitude and friendly behaviour during my PhD motivated me for more focusing on my research.

I would like to thank Prof. Gregory J. Szulczewski, Assist. Prof. Huseyin Kurt, Dr. Kaan Oguz and Dr. Ciaran Fowley for their interest and skilful guidance during my PhD. Special thanks to Assist. Prof. Huseyin Kurt who helped me to design and set up a new deposition system and Dr. Kaan Oguz who shared his house with me in my first years in Dublin and became a good friend in my life.

I want to thank our postdocs Dr. Munusamy Venkatesan, Assist. Prof. Plamen S. Stamenov, Dr. Karsten Rode, Dr. Lorena M. Monzon and Dr. Rémy Lassalle-Balier for their invaluable comments and helps. Spacial thanks to Assist. Prof. Plamen S. Stamenov and Dr. Munusamy Venkatesan for spending too much time to measure my samples in SQUID or PPMS as well as scientific discussions.

I feel fortune have group members who made the time in my PhD enjoyable and shared the any sort of problem, Dr. Simone Alborghetti, Dr. Damaris Fernandes, Davide Betto, Jong C. Lau, Kiril Borisov, Amir Sajad Esmaeily and Hongjun Xu. I am especially thankful to Dr. Inam M. Mirza for being a nice housemate and invaluable discussions about the science and life.

CONTENTS

SUMMARY III

ACKNOWLEDGMENTS VI

CHAPTER 1 1

1.1 INTRODUCTION 1

1.2 SPIN ELECTRONICS 2

1.2.1 *Electron tunneling* 2

1.2.2 *Tunneling criteria* 5

1.2.3 *Anisotropic magnetoresistance and giant magnetoresistance* 6

1.2.4 *Tunneling magnetoresistance* 8

1.2.5 *Physical origin of tunneling magnetoresistive effect* 8

1.2.6 *Spin electronics: overview* 11

1.3 ORGANIC SEMICONDUCTORS 12

1.3.1 *Introduction* 12

1.3.2 *π-conjugation* 14

1.3.3 *Charge conduction in π-conjugated systems* 15

1.3.4 *Carrier injection and transport in organics* 17

1.3.5 *Materials for organic electronics* 20

1.4 ORGANIC SPIN ELECTRONICS 25

1.4.1 *Life of spin in organics* 26

1.4.2 *Organic spin valves: overview* 28

1.5 SUMMARY 35

1.6 BIBLIOGRAPHY 37

CHAPTER 2 45

2.1 INTRODUCTION 45

2.2 THIN FILM DEPOSITION 46

2.2.1 Sputtering process and its basics *46*

2.2.2 Magnetron sputtering *48*

2.2.3 Thermal evaporation *49*

2.3 THIN FILM DEPOSITION SYSTEMS 50

2.3.1 The Shamrock magnetron sputtering system *50*

2.3.2 Ultra high vacuum organic & metal thermal evaporation system *52*

2.3.3 Other organic evaporation systems *65*

2.4 DEVICE FABRICATION TECHNIQUES 69

2.4.1 Photolithography technique *69*

2.4.2 In-situ shadow masking technique *76*

2.5 CHARACTERIZATION TECHNIQUES 77

2.5.1 The Resistance-Temperature (R-T) rig *77*

2.5.2 SQUID magnetometer *78*

2.5.3 X-ray diffraction and X-ray reflectivity *79*

2.5.4 Atomic Force Microscopy *82*

2.6 BIBLIOGRAPHY 84

CHAPTER 3 85

3.1 INTRODUCTION 85

3.2 OVERVIEW 86

3.3 ELECTRONIC STRUCTURE OF METAL/ORGANIC INTERFACE 87

3.3.1 Metal-organic semiconductor contact *87*

3.3.2 Metal-insulator-organic semiconductor contact *88*

3.4 CARRIER INJECTION MECHANISM INTO AN ORGANIC SEMICONDUCTOR FROM A METAL 89

3.4.1 *Thermionic emission mechanism* 90

3.4.2 *Field emission mechanism* 91

3.4.3 *Back-flow tunneling* 92

3.5 SPECTROSCOPIC AND PHYSICAL CHARACTERIZATION OF METAL/ORGANIC INTERFACE **93**

3.6 MAGNETIC AND PHYSICAL PROPERTIES OF ORGANIC-FERROMAGNET AND ORGANIC-INSULATOR-FERROMAGNET INTERFACES **98**

3.6.1 *Ferromagnetic film thickness magnetisation method (FFTM)* 99

3.6.2 *SiO_2/Alq_3-Co interface* 100

3.6.3 *SiO_2/Alq_3-LiF-Co interface* 104

3.6.4 *The effect of an AlO_x layer at the Alq_3/CoFe interface* 111

3.6.5 *TEM, EDX and EELS analysis of CoFe-AlO_x-Alq_3-AlO_x-CoFe structure* 114

3.6.6 *SiO_2/Znq_2-Co interface* 118

3.6.7 *SiO_2/CuPc-CoFe interface* 121

3.7 CONCLUSION **127**

3.8 BIBLIOGRAPHY **129**

CHAPTER 4 .... **133**

4.1 INTRODUCTION **133**

4.2 SPIN VALVE TEST STACKS **135**

4.2.1 *Calibration of AlO_x barrier prepared by using shadow masking technique* 135

4.2.2 *Calibration of the MgO cleaning process* 142

4.2.3 *Magnetoresistive characteristics of MgO/LiF based MTJs* 144

4.3 ALQ_3 BASED HYBRID ORGANIC SPIN VALVES **146**

4.3.1 *Magnetoresistive characteristics of air exposed MgO/Alq_3 based hybrid devices* 147

4.3.2 *Magnetoresistive characteristics of argon ion cleaned MgO/Alq_3 based hybrid devices* 152

4.3.3 *Magnetoresistive characteristics of $AlO_x/Alq_3/AlO_x$ based hybrid devices prepared by using in-situ shadow masking* 161

4.4 CuPc based hybrid organic devices **169**

4.4.1 *Magnetoresistive characteristics of MgO/CuPc based hybrid devices prepared using UV lithography* 169

4.4.2 *Magnetoresistive characteristics of AlO_x/CuPc/AlO_x based hybrid devices prepared by in situ shadow masking* 174

4.5 Magnetoresistive characteristics of AlO_x/ZnPc/AlO_x based hybrid devices prepared by in situ shadow masking **177**

4.6 Znq_2 based hybrid organic devices **180**

4.6.1 *Magnetoresistive characteristics of MgO/Znq_2 based hybrid devices prepared using UV lithography* 180

4.6.2 *Magnetoresistive characteristics of $AlO_x/Znq_2/AlO_x$ based hybrid devices prepared by using in-situ shadow masking* 183

4.7 Conclusion **186**

4.8 Bibliography **188**

CHAPTER 5 .... **191**

5.1 Conclusion **191**

5.2 Future work **192**

LIST OF FIGURES

Figure 1.1. Wave function decays exponentially within the energy barrier......................3

Figure 1.2. Band diagram of metal/insulator/metal structure..5

Figure 1.3. A GMR spin valve structure. The dashed arrow shows the free layer while the continuous arrow shows the pinned layer. The current flows perpendicular to the plane. 6

Figure 1.4. The figure of conduction in a GMR structure (a) in parallel alignment and (b) in antiparallel alignment..7

Figure 1.5. Schematic representation of DOS: (a) for a normal metal and (b) for a ferromagnetic metal (arrows show majority and minority spin states)................9

Figure 1.6. Schematic diagram of spin dependent tunneling via the Jullière model. The top (a) and bottom (b) panels show the parallel and antiparallel alignment of the ferromagnetic electrodes, respectively. 10

Figure 1.7. Band structure of p-type Si (a) and rubrene (b) [22]....................................14

Figure 1.8. sp^2 hybridization of a carbon atom and π / σ bonds between neighbouring carbon atoms. 15

Figure 1.9. Molecular structure of Alq_3 (a) and two geometrical isomers: meridional (b) and facial (c). 22

Figure 1.10. Molecular structure and atomic orientations of metal phthalocyanine.......23

Figure 1.11. Bis(8-hydroxyquinoline) zinc(II), dihydrate (a) and anhydrous bis(8-hydroxyquinoline) zinc(II) (b)..25

Figure 1.12. Spin diffusion length, l_s, versus spin relaxation time, τ_s, for different classes of materials [22]. 28

Figure 1.13. Schematic view of an hybrid state at a ferromagnet/organic molecule interface, showing the density DOS of a ferromagnetic metal and an organic molecule when they are isolated (a) or in the contact (b,c) [90]. **35**

Figure 2.1. Sputtering process, showing the ejected atoms from the target surface as a result of striking energetic ions to the target surface. **46**

Figure 2.2. DC sputtering system showing the sputtered target atoms and formation of a thin film on the substrate surface. **48**

Figure 2.3. The magnetron sputtering system showing the plasma confined near the target area where the magnetic field is strong **49**

Figure 2.4. The Shamrock system, showing chamber B, C and D as well as a schematic drawing of the whole system **51**

Figure 2.5. Overall view of the organic UHV chamber **53**

Figure 2.6. The bottom plate of the organic UHV chamber, showing the triple molecular organic evaporation assembly, metal heating sources and a schematic drawing of one of the evaporation pockets in the organic evaporation assembly. **54**

Figure 2.7. Thermal evaporation sources, showing alumina coated boat (top left panel), baffled tantalum box heater (bottom left panel), tantalum microelectronics box heater (bottom right panel) and metal plated tungsten rods (top right panel). **56**

Figure 2.8. Showing the tools for Al deposition. Firstly, single Al pellet is put inside the BN crucible and the crucible is then surrounded by molybdenum thin sheet. **56**

Figure 2.9. The bottom side of the organic UHV chamber showing the electrical and cooling connections 57

Figure 2.10. The thickness/rate monitor (QCM) 58

Figure 2.11. The picture of the load-lock showing its assembly 60

Figure 2.12. Sample mounting and transferring. A 25 mm SiO_2 wafer is attached on the copper substrate holder (a), the substrate holder is mounted on the transfer arm in the load-lock (b) and the rotational assembly to hold the substrate in the main chamber (c). 60

Figure 2.13. Picture of the shadow mask and linear motion mechanism 62

Figure 2.14. Picture of the ion gun and its power supply. 64

Figure 2.15. Picture of Camellia 66

Figure 2.16. Picture of the organic evaporator. 67

Figure 2.17. The bell-jar evaporation system and a schematic drawing 68

Figure 2.18. UV exposure, showing the UV light passing only from some specific areas through the metal mask; the features on the mask are transferred to the substrate after developing. 70

Figure 2.19. The picture of the OAI mask aligner 71

Figure 2.20. Picture of the Millatron 72

Figure 2.21. A picture of the first UV photomask (a) and zoom in (b). (c) shows the spinner and the hot plate for soft-baking. 75

Figure 2.22. Device patterning process 75

Figure 2.23. Junctions produced by shadow masking technique and an SEM image (the scale bar is 100 μm) 77

Figure 2.24. The picture of the R-T rig 78

Figure 2.25. SQUID magnetometer 79

Figure 2.26. X-ray diffraction **80**

Figure 2.27. a) FWHM for a real and b) ideal XRD peak [7] **80**

Figure 2.28. Phillips X-Pert Pro system **82**

Figure 2.29. Nanoscope 3a Multimode Atomic Force Microscope **83**

Figure 3.1. Formation of a metal-semiconductor interface and energy level alignments in separate (a) and contact (b) positions. **88**

Figure 3.2. Energy levels alignment of Al/Alq_3 interface (a) and $Al/LiF/Alq_3$ interface. **89**

Figure 3.3. Illustrating different injection mechanism for the metal-semiconductor interface where JTE, JEF and Jback represent the thermionic emission, field emission and back scattering, respectively. **90**

Figure 3.4. Comparison of the XPS spectra of the Alq_3 core levels before and after deposition of Co layers with different thicknesses [20] **93**

Figure 3.5. Showing the XPS spectra of Co ($2p_{3/2}$) core levels of the Co layers of various thicknesses deposited on Alq_3 [20]. **94**

Figure 3.6. TEM images showing the metal/organic interface (a) taken from ref. [20] and (b) taken from ref. [2] **96**

Figure 3.7. Showing the interface feature of the $Alq_3/Co/Au$ structure (a) TEM image, (b) EELS image [10]. **97**

Figure 3.8. a) Schematic illustration of different magnetic interfaces: (i) sharp, atomically flat interface, (ii) diffuse interface with a reached interlayer where the metal is no longer all ferromagnetic, (iii) a rough but sharp interface, and (iv) very rough but sharp interface. b) The magnetic moment is plotted as a function of the nominal thickness of ferromagnetic metal, t. **100**

Figure 3.9. The stacks used for magnetic dead layer investigation showing uncapped (a) and capped (b) Co layer. 101

Figure 3.10. Room temperature magnetization curves for cobalt layers of different nominal thicknesses on SiO_2 (a) and FFTM plot of the data, showing the effect of introducing a 3.5 nm Al capping layer (b). 101

Figure 3.11. FFTM plots of the Alq_3/Co interface showing the effect of the Al capping layer (a) and the bilayer with Alq_3 on top (b). 103

Figure 3.12. AFM image of SiO_2/Alq_3 (20 nm) (a) and SiO_2/Alq_3(20 nm) LiF (2 nm) (b) 105

Figure 3.13. TEM image of SiO_2/ Alq_3(40nm)/LiF(2nm)/Co(5nm)/Al(7) multilayer in normal dark field mode (a) and high resolution mode (b). 106

Figure 3.14. The XRR reflectivity of the SiO_2/Alq_3(40)/LiF(2)/Co(5)/Al(7) stack. The black line is the experimental data and the red line is the fit. 107

Figure 3.15. Magnetisation curves of Co layer with varying LiF thickness and corresponding multi-layer. 108

Figure 3.16. FFTM plots of the Alq_3/Co interface showing the effect of the LiF buffer layer a) at 300 K and b) at 4 K 109

Figure 3.17. Magnetisation switching curves of Co layers at 4 K showing the effect of the LiF buffer layer a) with LiF and b) without LiF. 109

Figure 3.18. Related multi-layer stacks for Figure 3.17, showing the Co layer deposited either on LiF or Alq_3. 110

Figure 3.19. Magnetisation curves of the CoFe layer showing the effect of AlO_x at the Alq_3/CoFe interface. 113

Figure 3.20. Showing the TEM, EDX and EELS data of SiO_2/CoFe(8)-AlO_x(1.5)-Alq_3(10)-AlO_x(1.5)CoFe(18) stack. 115

Figure 3. 21. TEM, EDX and EELS data, showing the elemental composition in the middle of the Alq_3 layer. 116

Figure 3.22. Electron intensity profiles taken from different regions of the top and bottom interfaces of SiO_2/CoFe(8)-AlO_x(1.5)-Alq_3(10)-AlO_x(1.5)CoFe(18). . 117

Figure 3.23. The stacks showing that the Co layer is either deposited on SiO_2 or Znq_2. 119

Figure 3.24. Room temperature magnetisation curves of Co layers with different under layer and top layer (a) and FFTM plot of the data, showing the related magnetic dead layers (b). 119

Figure 3.25. AFM (a) and XRR (b) measurements of a 10 nm thick Znq_2 film showing smooth surface. 120

Figure 3.26. TEM and electron intensity profile showing the sharp interface between Znq_2 and Co. 121

Figure 3.27. Room temperature magnetisation switching curves of SiO_2/CuPc(5)-CoFe(t)-AlO_x(1.5) (a) and SiO_2/CuPc(5)-AlO_x(1.5)-CoFe(t)-AlO_x(1.5) (b). 123

Figure 3.28. Showing the room temperature magnetisation switching curves of CoFe layer with the combination of different bottom and top layers (a) and FFTM plot showing the effect of AlO_x on the formation of the magnetic dead layer (b). 124

Figure 3.29. AFM image of SiO_2/CuPc(2nm) single layer and RMS roughness of the different CuPc single layers with thickness ranging from 2 to 8 nm. 126

Figure 3.30. TEM image of an unpatterned stack. 126

Figure 4.1. TMR response of the AlO_x based MTJ devices, comparing the formation of AlO_x in different preparation conditions. 137

Figure 4.2. TMR response of the stack D, showing the effect of the positions and types of ferromagnetic electrodes in the stack. **138**

Figure 4.3. The I-V and conductance graphs of the J-4 in set 1 (a,b) and J-5 in set 2 (c,d).......... **140**

Figure 4.4. TMR and I-V responses of the stack of CoFe (10nm)/AlO_x (D)/CoFe (18nm) as a function of temperature. **141**

Figure 4.5. Schematic representation of sample preparation using Ar-ion cleaning process **143**

Figure 4.6. RA and TMR response of the samples with different cleaning time for MgO surface. **144**

Figure 4.7. I-V characteristics of MgO (2.5 nm)/LiF (t) based hybrid devices when *t*=0 nm (a) and *t*=1 nm (b). **146**

Figure 4.8. TMR characteristics of MgO (2.5 nm)/LiF (t) based hybrid devices when *t*=0 nm (a) and *t*=1 nm (b). **146**

Figure 4.9. Evolution of air exposed MgO/Alq_3 based stack. **148**

Figure 4.10. TMR characteristics of air exposed MgO (2 nm)/Alq_3 (*t*) based hybrid devices with different thicknesses of Alq_3 at 10 mV. Also, the curve for *t*= 2 nm at 500 mV is included.......... **149**

Figure 4.11. Resistance-area product plotted as a function of Alq_3 barrier thickness in MgO/Alq_3 MTJs. The red curve shows the fitting. **150**

Figure 4.12. Bias dependent TMR characteristics of MgO/Alq_3 based hybrid devices. **152**

Figure 4.13. Evolution of the cleaned MgO (2.5 nm)/Alq_3 (t) based stacks. **153**

Figure 4.14. Room temperature TMR characteristics of argon ion cleaned MgO (2.5 nm)/Alq_3 (t) based hybrid devices. **154**

Figure 4.15. The left panel shows our experimental data while the right panels show the data taken from Ref. [21]. In both data, an exponential increase of RA with Alq_3 thickness was seen and the RA changed slightly with temperature. The stack used in Ref. [21] was Co (8 nm)/AlO_x (0.6 nm)/Alq_3 (1.6 nm)/NiFe (10 nm). **155**

Figure 4.16. Magnetoresistance curves as a function of applied bias measured from contaminated or uncontaminated MgO based tunnel junctions, where the data taken from our study (a) and literature (b) [11] (note that the scales on the graphs are different). The black solid lines in both figures represent the TMR of devices which have contaminated interfaces. **157**

Figure 4.17. Bias dependent TMR curves of the MgO (2.5 nm)/Alq_3 (t=0, 1, 2 and 3 nm) based hybrid devices. **158**

Figure 4.18. Comparison of the normalized bias dependent TMR curves, where the data is taken from our study (a) and Ref. [22] (b). Note that the polarity of the applied bias in both figures is reversed and the bias scales are different. **159**

Figure 4.19. Two-step tunneling and spatial distribution of Gaussian DOS of the intermediate sites under an applied bias with different electrical polarity [22]. **161**

Figure 4.20. MR (a) and I-V (b) curves of the device as a function of temperature when t=1 nm. The inset shows the variation of junction resistance and MR as a function of temperature. **162**

Figure 4.21. MR and I-V characteristics of the device when t = 2 nm. The MR data was measured at 15 K and the inset figure shows the variation of device resistance as a function of temperature. **163**

Figure 4.22. MR, I-V and dI/dV characteristics of the device when t=3 nm. The inset shows the variation of device resistance with temperature. **164**

Figure 4.23. Thickness dependent resistance of organic devices, where the data in (a) represent our study while the data in (b) is taken from Ref. [23]. The dashed line in (a) is an eyes-to-guide plot. The stack in (b) is Ta (2)/CoFeB (2)/AlO_x (~ 1.5)/Alq_3 (t)/Co (20), where the numbers in parentheses are the layer thicknesses in nanometre. The junction size in (a) and (b) is 250x250 μm^2 and 300x300 μm^2, respectively. **166**

Figure 4.24. Schematic band diagram ferromagnet/Alq_3/ferromagnet structure (a) and inverse current density as a function of Alq_3 thickness (b) [23]. **167**

Figure 4.25. Evolution of MgO/CuPc based MTJ stacks. **170**

Figure 4.26. TMR characteristics of the first set of sample at 300 K (a) and at 50 K (b). The inset in (b) shows the variation of TMR with temperature for all samples. **171**

Figure 4.27. Temperature dependent resistance behavior of the first set of sample (a) and RA product versus square root of area plot (b). **172**

Figure 4.28. MR characteristics of the second set of samples at 300 K (a) and at 20 K (b). **173**

Figure 4.29. TMR characteristic at 18 K (a) and the temperature dependent I-V characteristics (b) of CuPc based device when t=1 nm. The dI/dV curve was calculated from the I-V data measured at 18 K (c). The inset in figure (b) shows the variation of MR and resistance as a function of temperature. **175**

Figure 4.30. MR (a), I-V (b) and dI/dV (c) characteristics of 2 nm thick CuPc based device, where the MR curve was measured at 17 K. **176**

Figure 4.31. MR (a), I-V (b) and dI/dV (c) characteristics of 1 nm thick ZnPc based device, where the MR curve was measured at 15 K. The inset in figure (c) shows the MR and normalized resistance of the device as a function of temperature. **178**

Figure 4.32. MR (a), I-V (b) and dI/dV (c) characteristics of 3 nm thick ZnPc based device, where the MR curve was measured at 15 K. The inset in (c) shows the normalized resistance of the device as a function of temperature. **179**

Figure 4.33. Resistance of a set of junctions with increasing ZnPc thickness. **180**

Figure 4.34. Evolution of MgO/Znq_2 based MTJ stacks. **181**

Figure 4.35. TMR characteristics of MgO (2 nm)/Znq_2 (t) based MTJs (a) and variation of RA as a function of temperature (b). **182**

Figure 4.36. Bias dependent TMR curves of MgO (2 nm)/ Znq2 (t) based junctions.. **182**

Figure 4.37. MR (a) and I-V (b) characteristics of Znq_2 based device when t=1 nm, where the MR curve in (a) was measured at 20 K. **184**

Figure 4.38. MR curves of Znq_2 based device when t=2 nm at 18 K for 50 mV (a) and 100 mV (b). **184**

Figure 4.39. MR (a) and I-V (b) characteristics of Znq_2 based device when t=10 nm, where R-H curve was measured at 18 K applying 500 mV. Also, a zoom in view of the I-V curve is shown in (c). **185**

Chapter 1

INTRODUCTION

1.1 Introduction

Magnetism features in many research areas not only as a branch of science but also due to its important applications in areas such as magnetic sensors and magnetic memories. In the 21st century, technological development is providing denser, faster and smaller electronic devices as well as low power consumption in order to improve device functionalities. Techniques such as UV lithography and electron beam lithography allow fabrication of micron or nano-scale magnetic devices. These tiny devices enable to study of basic magnetic phenomena such as magnetoresistive [1,2] and spin torque effects [3]. Magnetic effects add to the functionality of electronic devices. Hence, the use of the spin property of the electrons in devices gives rise to the name *spin electronics*.

1.2 Spin electronics

Spin is the intrinsic angular momentum of electrons and it is a purely quantum mechanical phenomena. Electrons have two different spin states, spin up and spin down corresponding to the angular momentum states $m_s = -1/2$ and $m_s = +1/2$. It is possible to build devices in which the spin property of electrons is controlled. Spin electronic devices may have small operation size which can offer high information storage density and fast operation speed because direction of spins can switch on times of the order of a nanosecond. Moreover, spin electronic devices such as magnetic random access memories (MRAMs) are non-volatile, so that when the power goes off, the spins can keep their polarization directions, whereas in the conventional devices such as in dynamic random access memories (DRAMs) capacitors lose their charges. In DRAM chips all the memory elements are refreshed by reading and re-writing the contents. This situation requires a constant power supply, which is the reason why DRAMs lose their memory when the power turns off. However, MRAM does not need to be refreshed and no continuous power is required to keep the information. All these consideration mean that spin electronics is an attractive research area for the information storage industry.

1.2.1 Electron tunneling

The transport mechanism of electrons within an insulating layer is the tunneling phenomenon which is a purely quantum mechanical effect. Electrons have both particle

and wave like properties. Tunneling is a wave like effect of electrons. When electrons come across an energy barrier, their wave functions do not end abruptly but can pass through the barrier even though the electron energy is less than the energy barrier height. Then, same electrons have a probability of appearing on the other side of the barrier. This effect has no classical counterpart. Figure 1.1 shows the tunneling effect.

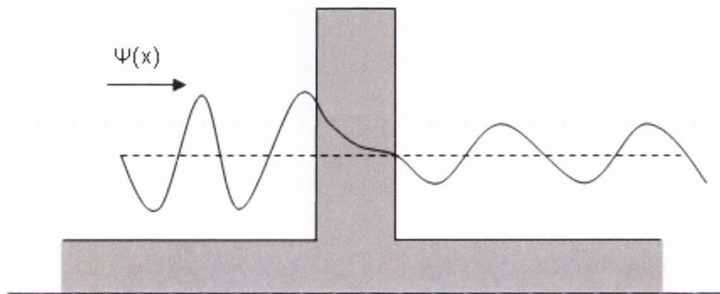

Figure 1.1. Wave function decays exponentially within the energy barrier

In a metal/insulator/metal contact, electrons tunnel from one electrode to the other and there exists a tunnel current if a potential difference is created between the electrodes. The typical band diagram of metal/insulator/metal junction under a bias voltage is shown in Figure 1.2. The tunneling current from the left electrode to the right electrode depends on the density of states of the first electrode, ρ (E), and that of the second electrode, ρ (E+eV), the square of matrix element $|M|^2$, which represents the probability of transmission through the barrier, occupation probabilities that states in the left electrode, f (E), and probability [1-f(E+eV)] that the states in the right electrode are empty. The resulting tunneling current is given by the following expression;

$$I_{l\rightarrow r} = \int_{-\infty}^{+\infty} \rho_l(E).\rho_r(E+eV).|M|^2.f(E).[1-f(E+eV)]dE \tag{1}$$

and the total tunneling current is described as

$$I_{total} = I_{l\rightarrow r} - I_{r\rightarrow l} \tag{2}$$

For this type of junctions, Simmons generalized a tunnel current density and expressed it as following formula [4];

$$J(V) = \frac{j_0}{d^2}\left(\varphi - \frac{eV}{2}\right)e^{\left[-Ad\sqrt{\varphi - \frac{eV}{2}}\right]} - \frac{j_0}{d^2}\left(\varphi + \frac{eV}{2}\right)e^{\left[-Ad\sqrt{\varphi + \frac{eV}{2}}\right]} \tag{3}$$

where $J(V)$ is the tunnel current density as a function bias voltage V. A and j_0 are the constant terms of $4\pi\sqrt{2m_e^*/h}$ and $e/2\pi h$, respectively, where m_e^* is the effective mass of the electron. φ is the average barrier height, d is the barrier thickness. This term shows a linear response at small voltages. However, it has a non-linear characteristic for larger voltages, which is evidence that current is due to tunneling electrons in M/I/M structures. It can also be seen that tunneling current shows exponential dependence on the barrier thickness and average barrier height. This expression can be used only for symmetric structures, the left and right electrodes are identical. For asymmetric structures, Brinkman's calculation is used [5].

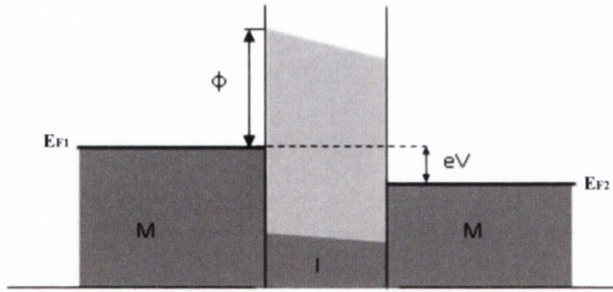

Figure 1.2. Band diagram of metal/insulator/metal structure

1.2.2 Tunneling criteria

As it is discussed in section 1.2.1, tunneling is a purely quantum mechanical effect that occurs on the atomic scale. This event can be clearly observed in many tunnel junction devices in laboratory conditions. Therefore, it is worthwhile to outline the criteria for the expected tunneling behavior. First of all, exponential dependence of the tunnel current on the barrier thickness, barrier height and applied bias will result in a non-linear current/voltage curve in the tunneling limit. Also the differential conductance will be quadratically dependent on the applied bias. Next, the resistance-area product should remain constant for the same barrier thickness, indicating of a uniform barrier without any hot-spots. Furthermore, the resistance of a device, in the tunneling regime, should not change excessively with the temperature. The criterion accepted for the tunneling model is slight increase with decreasing temperature (~10-20 %). If the resistance decreases with the decreasing temperature, it is more likely due to the metallic shorts in the barrier [6]. It is important to satisfy these criteria when the observed TMR in molecular junctions is being interpreted.

1.2.3 Anisotropic magnetoresistance and giant magnetoresistance

The effect of spin on the electrical resistance was firstly observed by Thomson [7]. He demonstrated that the electrical resistance of a ferromagnetic conductor depended on whether the current flowing through the conductor was perpendicular or parallel to the magnetization of the sample. When the current flows parallel to the magnetization direction of the sample, a stronger scattering process occurs and higher resistance is observed, $\rho_{\parallel}$. However, when the current and magnetization direction are perpendicular to each other, lower scattering and lower resistivity are observed, $\rho_{\perp}$. This effect has been called as anisotropic magnetoresistance effect (AMR). The effect is of order 1% in ferromagnetic metals. Although the AMR effect had previously shown the relationship between magnetization and electrical resistance, the discovery of Giant Magnetoresistance (GMR) effect in 1988 is considered as the birth of spin electronics. It was independently discovered for Fe/Cr multilayers [1] and for Fe/Cr/Fe trilayers [2]. A typical GMR device consists of two ferromagnetic layers (FM) separated by a nonmagnetic (NM) spacer layer which behaves as a 'spin valve'. The schematic of spin valve structure is shown in Figure 1.3.

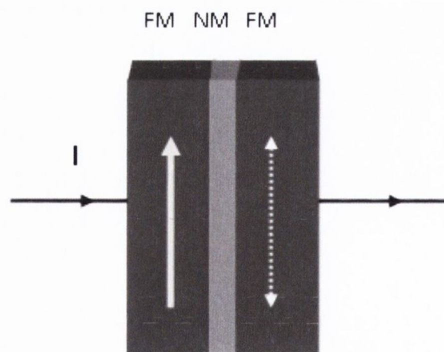

Figure 1.3. A GMR spin valve structure. The dashed arrow shows the free layer while the continuous arrow shows the pinned layer. The current flows perpendicular to the plane.

The operation principle of these devices depends on the relative alignment of magnetizations of the two FM layers one of which is pinned while the other one is free to rotate under external magnetic field. If the magnetization directions of the magnetic layers are antiparallel, the system shows high resistance. When they are aligned parallel, the resistance reaches its minimum value. Figure 1.4 summarizes the operating principle of a simple GMR structure. In Figure 4a, only the spin up electrons can pass without any scattering through the whole structure and spin down electrons scatter within the both layers then conduction is supplied by spin up electrons. However, in Figure 4b, while only the spin down electrons scatter within the first layer, the spin up electrons do not scatter and for the second FM layer vice versa then system has a big resistance. The significant change of the resistance has been called as giant magnetoresistance and the value of the GMR is defined by the following expression;

$$GMR = \left(\frac{R_{\uparrow\downarrow} - R_{\uparrow\downarrow}}{R_{\uparrow\downarrow}}\right) \text{x}100 \tag{4}$$

where $R_{\uparrow\downarrow}$ and $R_{\uparrow\uparrow}$ are the resistances of the antiparallel and parallel alignment, respectively.

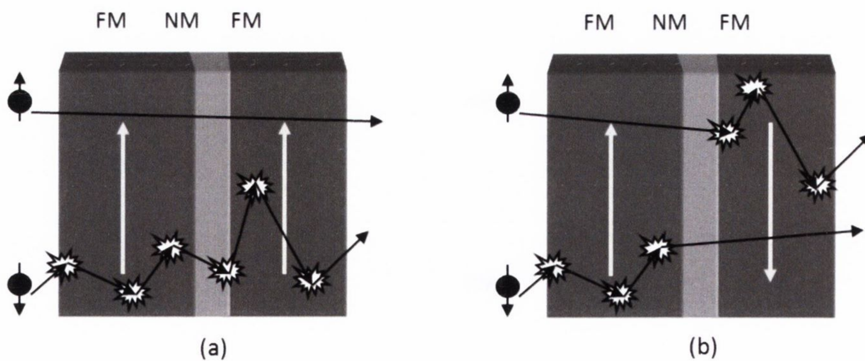

Figure 1.4. The figure of conduction in a GMR structure (a) in parallel alignment and (b) in antiparallel alignment

1.2.4 Tunneling magnetoresistance

The development of the spin electronics has been helped by the discovery of tunneling magnetoresistance (TMR) effect. A simple TMR device consists of two FM layers which are separated by a NM insulating spacer layer. In the TMR devices, the insulating layer should be very thin so that electrons can tunnel easily without any scattering. The thickness of the insulating layers generally is about 1-2 nm. The operating principle of the TMR devices like that of the GMR devices is based on the relative alignment of the FM electrodes. However, the physical origin of TMR depends on the quantum mechanical tunneling phenomena of the wave function of the electrons.

1.2.5 Physical origin of tunneling magnetoresistive effect

The physical origin of the operation of TMR structures is based on spin dependent scattering process of the tunnel electrons at the insulator/ferromagnet interface. It is well known that ferromagnetic materials such as Fe, Co and Ni have a different density of states (DOS) for the spin up (majority electrons) and spin down electrons (minority electrons) at the Fermi level because of the exchange interaction between the electrons. These electrons at the Fermi level are *spin polarized*. In contrast, for normal metals the number of the spin up and down electrons is the same at the Fermi level (Figure 1.5).

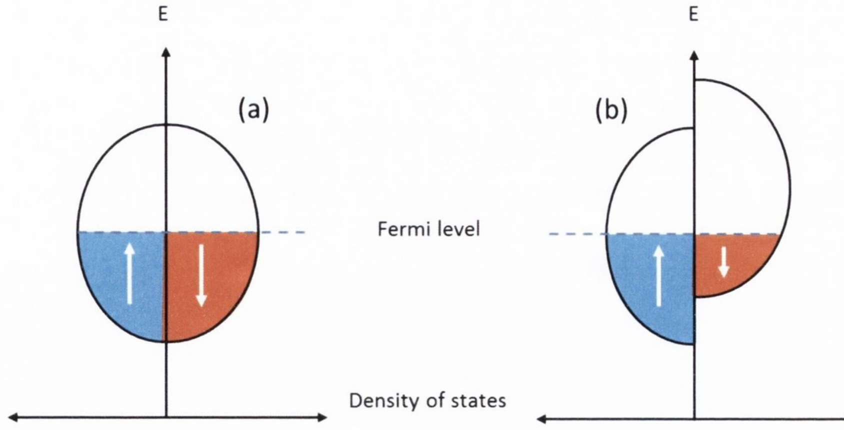

Figure 1.5. Schematic representation of DOS: (a) for a normal metal and (b) for a ferromagnetic metal (arrows show majority and minority spin states)

The different DOSs lead to different transport behavior of the majority and minority spin electrons in a FM material. Considering a spin polarized tunneling in a FM/I/FM structure in a parallel magnetization alignment and large DOS for the majority electrons (up-spin). The up-spin and down-spin electrons create two conductance channels in a different flow rate due to the different amount of spin polarized electrons and they can find themselves in a region of the same spin state in the other FM layer. In the antiparallel case, magnetization direction of the second FM layer is reversed and the spin dependent DOS changes, resulting in large amount of majority electrons scatter due to the lack of available spin states at the Fermi level. In the Jullière model, it is assumed that the conductance is proportional to the density of states of the ferromagnetic electrodes and a formula showing the relation between tunneling

$$TMR = \frac{2P_1P_2}{1 - P_1P_2}, \tag{5}$$

magnetoresistance and spin polarization of the ferromagnetic electrodes can be written as [8]:

with $P_{1,2}$ denotes the spin polarizations of the ferromagnetic electrodes and it is given by

$$P_{1,2} = \left(\frac{D_{1,2}^{\uparrow} - D_{1,2}^{\downarrow}}{D_{1,2}^{\uparrow} + D_{1,2}^{\downarrow}} \right) \quad (6)$$

where $D_{1,2}^{\uparrow}$ and $D_{1,2}^{\downarrow}$ are the densities of states of the electrodes at the Fermi energy (E_F) for the majority-spin and minority-spin bands, respectively. Figure 1.6 illustrates the spin dependent tunneling in a FM/I/FM structure in the case of parallel and antiparallel alignment of the ferromagnetic electrodes.

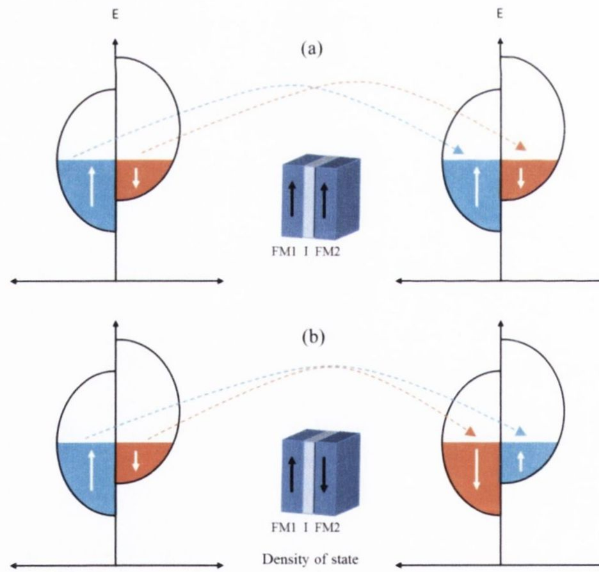

Figure 1.6. Schematic diagram of spin dependent tunneling via the Jullière model. The top (a) and bottom (b) panels show the parallel and antiparallel alignment of the ferromagnetic electrodes, respectively.

1.2.6 Spin electronics: overview

Although the first experiment reported by Jullière at low temperature showed 14% TMR ratio for Co/oxidized Ge/Fe stack but his results were not reproduced [8]. Significant changes in the magnetoresistance at room temperature were observed for a CoFe/Al_2O_3/Co stack with TMR ratio of 11% [9] and Fe/Al_2O_3/Fe junctions with a TMR ratio of 20% [10]. Since that time scientists have been trying to improve the TMR ratios of MTJs by using different ferromagnets (Fe, Co, Ni alloys), different barriers and different physical treatments. One of the most widely used approaches is subsequent annealing of the multilayers. Annealing of multilayers under the suitable conditions can greatly enhance the TMR ratio [11]. Furthermore, polycrystalline CoFe [12] and amorphous CoFeB [13] electrodes show a TMR ratio of 50% and 70%, respectively with an AlO_x barrier. Another method in order to obtain a high TMR ratio is to use of electrodes which have higher spin polarization at the Fermi level. Some materials such as CrO_2, Fe_3O_4, $La_{0.7}Sr_{0.3}MnO_3$, $La_{0.7}Ca_{0.3}MnO_3$, Sr_2FeMoO_6 types and Heusler alloys like NiMnSb or Co_2MnSi [14] shows half metallic behavior with electrodes of only one spin sub-band at the Fermi level. By using this type of electrodes, it has been possible to obtain very large TMR ratios at low temperatures. However, the TMR ratio decreases and vanishes at near the room temperature for many of them [15]. The last method to achieve high TMR ratios is to use a crystalline MgO barrier instead of an amorphous Al_2O_3 spacer layer. It is well known that crystalline structures have perfectly ordered atoms in space and the number of structural defects is less than for amorphous materials. To use a crystalline MgO barrier results in coherent tunneling with low scattering in the barrier. Thus, it is possible to obtain large TMR ratios compared to the MTJs with an amorphous Al_2O_3 barrier. This was predicted by

Butler et al. [16]. In 2004, giant tunneling magnetoresistance was observed in MTJs using crystalline MgO barrier [17,18]. Yuasa et al. observed 180 % TMR at room temperature and 250 % at low temperature in a Fe/MgO/Fe MTJs grown by molecular beam epitaxy [17]. Independently, Parkin et al. also reported 220 % TMR ratio at room temperature using the stack of CoFe/MgO/CoFe [18]. Furthermore, Djayaprawira et al. obtained 300 % at low temperature and 230 % at room temperature with CoFeB/MgO/CoFeB multilayer grown by magnetron sputtering, where CoFeB layers are amorphous but MgO layer is (001) textured [19]. Later, TMR ratios was achieved the value of 500 % for CoFeB/MgO/CoFeB stack at room temperature [20]. Hence, single crystalline MgO has been widely used as a barrier layer in many magnetic tunnel junctions. At 300 K, the highest TMR, 604%, has been observed in CoFeB/MgO/CoFeB structure by performing some critical annealing treatments and suppressing the Ta diffusion into the active region in the TMR stack [21].

1.3 Organic semiconductors

1.3.1 Introduction

In organic semiconductors the most attractive point for spin electronic applications is the weakness of the spin scattering mechanism. In general, organic semiconductors consist of mostly light elements (C, H, N or O) and the strength of the spin-orbit interaction is proportional to Z^4, where Z is the atomic number. Long spinlife time due to the low spin-orbit coupling and weak hyperfine interactions should allow the spin polarized carriers to travel over large distances in the organic semiconductors despite

their small mobility [22]. One of the fundamental differences between organic and inorganic semiconductor is the charge transport mechanism. In inorganic semiconductors charge carriers are delocalized and moves in broad bands. Electrons and holes move with high mobility. However, in organic semiconductors the overlap of the orbitals of adjacent molecules is small, leading to narrow band width with little dispersion. Therefore, electrons move with low mobility. For example, the hole mobility of rubrene, one of the best organic semiconductor, is about 10 $cm^2V^{-1}s^{-1}$ at room temperature while the mobility of p-type Si is about 450 $cm^2V^{-1}s^{-1}$. Charge carrier transport in organics can be described by either band or hopping transport depending on the temperature and the degree of order in the material. Highly pure molecular crystals tend to conform to band transport at low temperatures. Hopping transport dominates in amorphous organic semiconductors and tends to occur between localized molecular states. Figure 1.7 compares the band structure of inorganic p-type Si and organic rubrene. These fundamental differences between organic and inorganic materials arise from the nature of the bonding properties. Whereas the organic materials are van de Waals bonded solids leading to a weaker intermolecular bonding, inorganic semiconductors are covalently bonded. This difference shows up in the mechanical and thermodynamic properties of those materials such as reduced hardness or lower melting point for the organics, and even more importantly, in the different optical or charge transport properties

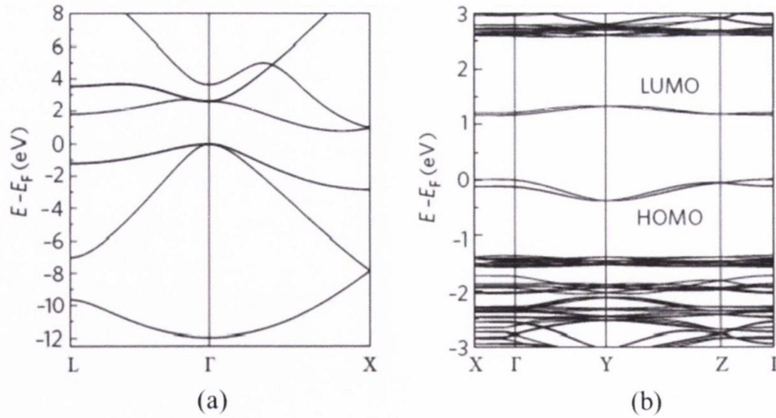

Figure 1.7. Band structure of p-type Si (a) and rubrene (b) [22]

1.3.2 π-conjugation

In an organic semiconductor, carbon atoms are connected by single or double bonds which are formed from a combination of *s* and *p* atomic orbitals. In the ground state, the electronic configuration of the carbon atom is $1s^2 2s^2 2p^2$. When two carbon atoms come closer, covalent bonds form between them and *2s* and *2p* orbitals mix to form new hybrid *sp*, sp^2 and sp^3 orbitals which are suitable for the qualitative description of atomic bonding properties. In the case of *sp* and sp^3 hybridization, all the electrons are strongly localized resulting in extremely poor charge conduction. In the case of sp^2 one *s* orbital combines with two *p* orbitals (p^x and p^y) orbitals and this combination creates three hybrid sp^2 orbitals. However, p^z orbital which is perpendicular to the plane of sp^2 orbitals remains unhybridized. In a carbon chain the overlapping sp^2 orbitals create σ-bonds while the p^z overlapping orbitals create π-bonds. In a carbon chain the p^z electrons delocalize across all the contiguous π-bonds in the molecule, resulting in conducting properties of the molecules.

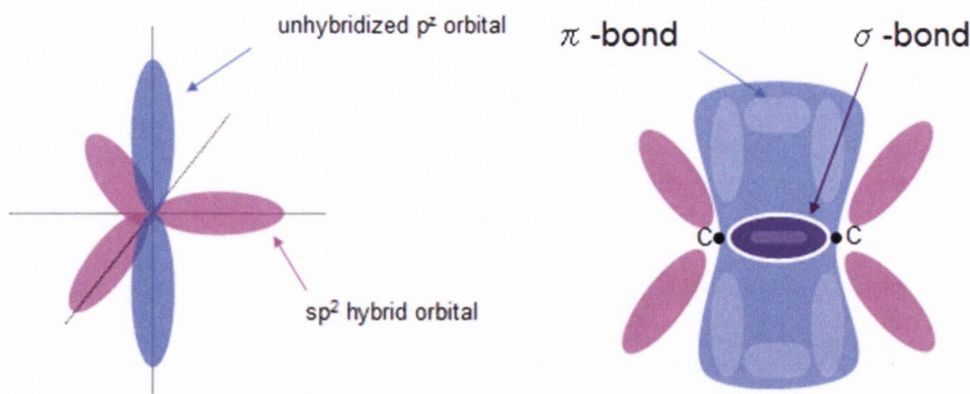

Figure 1.8. sp^2 hybridization of a carbon atom and π / σ bonds between neighbouring carbon atoms.

1.3.3 Charge conduction in π-conjugated systems

In organic materials, van der Waals forces are responsible for the intermolecular binding and those forces are much weaker than the covalent and ionic bonds of inorganic crystals. Therefore, organic materials are less rigid than the inorganics. Thus, electrical injection of charge carriers into the organic materials can create a distortion of the surrounding lattice due to the Coulomb interaction. Conduction electrons attract the positively charged ions and repel the negatively charged ions in the surrounding lattice on their path. The lattice distortion accompanies the charge carriers through the organic material, resulting in formation of a quasi-particle called *polaron*. Polarons can be either positively or negatively charged and they carry the spin of the accompanying electrons. On the other hand, the movement of the conduction electrons is hindered by the resulting lattice distortion which behaves as a potential well, and decreases the mobility.

Hopping and band type transport are possible transport mechanisms in organic materials. The band type conduction is expected for highly ordered organic materials at low temperature when the mean free path of the charge carriers exceeds the intermolecular distance [23]. Valance and conduction bands form by overlapping the HOMO and LUMO levels of the molecules, respectively. For disordered systems such as organic thin films, charge transport between the localized molecular states is via the hopping mechanism which strongly depends on the temperature, electric field, trap states in the material and carrier concentration [24-28]. Vapor deposited amorphous organic materials have a disordered structure, resulting in disordered HOMO and LUMO levels [29]. Therefore, the band conduction mechanism does not apply in these materials due to the disordered energy levels. The charges are localized on the molecular sites due to the disorder so the conduction mechanism becomes via phonon-assisted tunneling or hopping from one localized site to another site. The hopping probability from one site to another was formulated by Mott in his variable range hopping model [30];

$$P_{ij} \approx \begin{cases} e^{\left(-2\alpha R_{ij} - \frac{E_j - E_i}{kT}\right)} & if\ E_j > E_i \\ e^{\left(-2\alpha R_{ij}\right)} & if\ E_j \leq E_i \end{cases} \tag{7}$$

where P_{ij} is the hopping probability of the electrons from the i site to the j site, R is the distance between the two sites, E_i and E_j are the energy levels of an electron at the two sites and α corresponds to the exponential decay of the wave function in a potential barrier. From the equation one can deduce that the transport of the charge carriers is affected by the disorder of the position and energy of the hopping sites. In disordered systems, conduction is dominated by hopping process and at low temperatures conductance is satisfactorily explained by Mott's variable range hopping model. In

general, conductance, proportional to the probability of such a hop, as a function of temperature is given by [30]

$$G \propto e^{-(2\alpha R)} \approx e^{-\left(\frac{T_0}{T}\right)^{\frac{1}{1+d}}} \tag{8}$$

where T is the temperature, T_0 is the characteristic temperature and d is the dimension. The model predicts that variable range hopping length, R, increases with decreasing temperature as $T^{(1/1+\mathrm{d})}$, where d is the dimension.

1.3.4 Carrier injection and transport in organics

In the organic based electronic devices such as OLEDs, two different mechanisms govern the device operation, namely carrier injection limitation at the interfaces and space-charge limitation of the current in the organic. The injection limiting process occurs when the interface barrier is so high as to control injection of the carriers from metal to the organic layer. The three mechanisms which govern the injection limitation process are Fowler-Nordheim tunneling, Richardson-Schottky thermionic emission and backflow of the injected carriers. These mechanisms are briefly explained in Chapter 3. In contrast, space-charge limitation occurs when the charge carriers are injected from a good metallic contact which acts as an inexhaustible carrier reservoir. Using some basic equations such as the Poisson equation, the continuity equation together with the boundary conditions, drift-diffusion equation, and related equations for free and trapped charge carrier densities the relation between the current density and external voltage can be found by making analytical solutions in some special cases and the result is shown in the following Mott-Gurney equation [31];

$$J_{SCLC} = \frac{9}{8}\varepsilon\varepsilon_0\mu\frac{V^2}{d^3} \tag{9}$$

where ε is the dielectric constant of the material, ε_0 is the permeability of free space, μ is the charge carrier mobility which is independent of electric field and d is the width of the organic spacer between two electrodes. This relation is obtained in the case of perfect insulator without intrinsic carriers and traps as well as neglecting the diffusion. In the case of traps which have discrete energy levels, the current is generally lower and the quadratic field dependence is retained and the equation (9) is modified by a factor θ which is the ratio of free carriers to the total number of carriers;

$$\theta = \frac{n}{(n + n_t)} \tag{10}$$

where n and n_t are the number of free and trapped charges, respectively. If the traps are energetically distributed in the spacer, they will be filled with electric field and the current will increase faster than quadratic until all traps are filled. Thus, taking account these assumptions a relation between the trap-charge limited current density (TCLC) and voltage in the presence of the exponential trap distribution can be expressed as following;

$$J_{TCLC} = N_c\mu q\left(\frac{\varepsilon\varepsilon_0 l}{N_t q(l+1)}\right)^l\left(\frac{2l}{l+1}\right)^{l+1}\frac{V^{l+1}}{d^{2l+1}} \tag{11}$$

where N_c is the density of states in the conduction band, N_t is the effective density of traps, $l = E_t/k_BT$ and E_t is the trap energy [32]. On the other hand, electron mobility obeys the Poole-Frenkel model in the organic semiconductors. In general, charge carriers which move in an insulator are trapped in the localized states, and random thermal fluctuations may assist them by giving enough energy to escape from the trap states and move in the conduction band. Basically, the Poole-Frenkel model explains the effect of electric field which moves the charge carriers to the conduction band in the

absence of large thermal fluctuations. So, the field dependent mobility obeys the following Poole-Frenkel (PF) relation;

$$\mu(F) = \mu_o e^{(\beta\sqrt{F})} \tag{12}$$

where β is a constant , μ_0 is the zero-field mobility and F is the electric field. If the field dependent mobility is taken into account, the trap-free SCLC is given by the Murgatroyd approximation [33];

$$J_{SCLC}^{PF} \approx \frac{9}{8}\varepsilon\varepsilon_0\mu_0\frac{V^2}{d^3}e^{\left(0.89\beta\sqrt{V/d}\right)}. \tag{13}$$

Another important parameter which must be involved to understand the J-V characteristics of the devices is the temperature-dependent mobility. In the SCLC regime with an exponential trap distribution, the field and temperature dependent mobility can be expressed by the modified PF equation;

$$\mu(F,T) = \mu_{PF} e^{\left(-\frac{\Delta E - \beta_{PF}\sqrt{F}}{k_B T_{eff}}\right)}, \tag{14}$$

with

$$\frac{1}{T_{eff}} = \frac{1}{T} - \frac{1}{T_0}. \tag{15}$$

where ΔE is the activation energy for hopping at zero-electric field, T_0 is an empirical parameter and μ_{PF} is the mobility at $T=T_0$ and

$$\beta_{PF} = \sqrt{\frac{q^3}{\pi\varepsilon\varepsilon_o}}. \tag{16}$$

This model shows results comparable with the literature data, apart from the prefactor μ_{PF}. For example in Ref. [32] the calculated parameters from experimental data for

electron-only devices are that $\mu_{PF} = 1.2x10^{-4}cm^2/V.s$, $T_0 = 430$ K, $\Delta E = 0.43$ eV and $\beta_{PF} = 4.1x10^{-23}$ $J(cm/V)^{0.5}$, whereas those parameters for hole only devices in Ref. [34,35] are $\mu_{PF} = 3.5x10^{-4}cm^2/V.s$, $T_0 = 600$ K, $\Delta E = 0.48$ eV and $\beta_{PF} = 4.6x10^{-23}$ $J(cm/V)^{0.5}$.

1.3.5 Materials for organic electronics

Organic semiconductors can be classified into two major groups such as low molecular weight materials and polymers. The low molecular weight materials consist of small molecule or oligomers, made of a single monomer or a few repetitions. On the other hand, polymers are made of an unlimited sequential repeat of the monomer units. Both types of materials are π-conjugated system formed by p^z orbitals of sp^2-hyridized carbon atoms in the molecules. However, an important difference between those two classes of organic materials is seen when it comes to process them to form thin films. Whereas the thin film form of the small molecule organic materials can be obtained from the gas phase by sublimation or evaporation, polymer based thin films are processed from a solution by spin coating [36]. In this thesis, small molecule organic semiconductors are used in the experiments. Here, the general properties of some famous small molecule organic semiconductors used in this thesis are briefly mentioned.

1.3.5.1 Tris (8-hydroxiquinoline) Aluminum

Tris (8-hydroxiquinoline) Aluminum (Alq_3) is a coordination complex wherein Al is bounded to three 8-hydroxyquinoline ligands, giving the chemical formula $Al(C_9H_6NO)_3$ and it is a π-conjugated small molecule organic semiconductor. Alq_3 is most commonly used in OLEDs as an electron transport/light emitting layer [37]. Also, it is classified as an n-type organic semiconductor with the low charge carrier mobility: ~ 10^{-5} $cm^2V^{-1}s^{-1}$ for electrons and ~ 10^{-6} $cm^2V^{-1}s^{-1}$ for holes. HOMO and LUMO positions are 5.7 eV and 2.7 eV, respectively [38] with respect to the vacuum level. The melting point of crystalline Alq_3 is 419 °C and its decomposition temperature is above 430 °C [39]. There are two possible geometrical isomers of Alq_3: meridional (mer-Alq_3) and facial (fac-Alq_3) which is more insulator than the mer-Alq_3 due to the larger HOMO-LUMO gap [40]. It is generally believed that the meridional isomer, which is more stable than the facial phase, is the dominant species in most of the cases such as thermally evaporated amorphous thin films or crystalline state of Alq_3 [41]. Whereas the meridional phase had been experimentally clarified, there was no direct experimental evidence for the fac-Alq_3 until the last decade when it was reported that a facial isomer has been experimentally isolated in pure form [42-44]. The facial isomer which emits blue light has higher dipole moment than the meridional phase which emits green light, and the facial isomer is expected to influence the morphology of the thin films and injection of charge carriers at the interface in an OLED device. Furthermore, the difference of the HOMO-LUMO levels for the two phases influences the injection barrier and could acts as a trap for charge carriers [45-47].

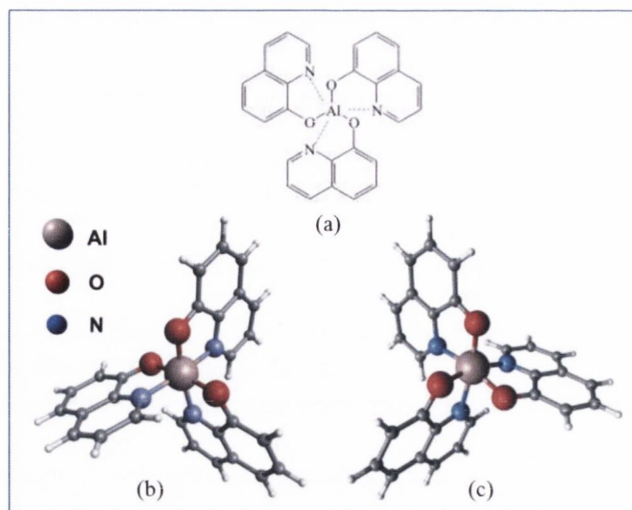

Figure 1.9. Molecular structure of Alq_3 (a) and two geometrical isomers: meridional (b) and facial (c).

1.3.5.2 Metal phthalocyanines

Phthalocyanine (Pc) is a polyaromatic porphyrin derivative molecule ($C_{32}H_{18}N_8$), characterized by high symmetry, planarity and electron delocalization. It can form coordination complexes with various metal elements by accommodating them in its central cavity. Almost every metallic atom in the periodic table can bind to the π-conjugated Pc molecule to form metal phthalocyanines ($C_{32}H_{18}N_8M$) (see Figure 1.10). The valance and spin state of the incorporated metal ions determine the electronic and magnetic properties of the structure so these properties can be controlled by changing the central atom. Therefore, it is of great interest to examine the effect of various chemical modifications on the electrical and magnetic properties of the metal substituted molecules. Most of the metal phthalocyanines (M-Pcs) exhibit excellent thermal and chemical stability [48] and they are used in a wide variety of applications such as light emitting diodes (LEDs) [49], solar cells [50], field effect transistors [51] and gas sensors [52]. The M-Pcs are classified as p-type organic semiconductors except

for copper hexadecafluorophthalocyanine ($F_{16}CuPc$) which is n-type. Among a number of different M-Pcs, copper phthalocyanine (CuPc) has been most extensively studied. Some electrical properties of CuPc and FePc are summarized in Table 1.1 for comparison, such as thin film device mobility, single crystal device mobility and resistivity.

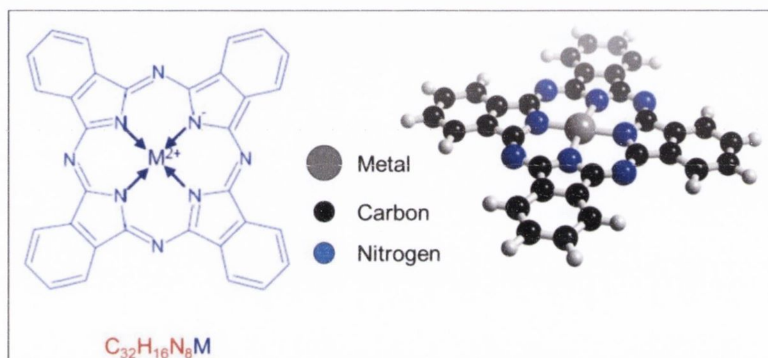

Figure 1.10. Molecular structure and atomic orientations of metal phthalocyanine.

	CuPc	Ref.	FePc	Ref.
Single crystal mobility ($cm^2/V.s$	1.0 0.3	[53,54]	0.3	[54]
Thin film mobility ($cm^2/V.s$)	0.01 0.04	[55,56]	0.02	[57]
Resistivity (Ω.cm)	$5x10^9$ $0.2\text{-}1x10^8$	[58,59]	$1\text{-}7x10^8$ $1\text{-}3x10^8$	[60,61]

Table 1.1. Some electrical properties of CuPc and FePc.

1.3.5.3 Bis(8-hydroxyquinoline) Zinc(II)

Metal 8-hydroxyquinoline chelates (Mq_n) have been extensively studied for many different research fields especially in OLEDs, where M stands for metal, n is the oxidation state of the metal and q is the 8-quinolinol complex. Bis(8-hydroxyquinoline) Zinc(II) (Znq_2) is one of the Mq_2 complexes which is used an electron transport layer in the electroluminescent devices. The studies showed that Znq_2 has better injection efficiency and higher quantum yields than the Alq_3 in device performance, resulting in a lower operating voltages [62,63]. In the atmospheric conditions, Znq_2 can be exist in the form of dihydrate ($Znq_2 \cdot 2H_2O$), two water molecules axial to the Zn atom with the in-plane hydroxyquinoline ligands while it forms as tetramer $(Znq_2)_4$ in the anhydrous conditions where four Znq_2 molecules are bridged together through the oxygen atoms [62]. Unlike Alq_3, the tetramer form of Znq_2 is a symmetrical molecule around its center. The general advantages of the Znq_2 in OLEDs are that the devices are thermally more stable than the case of other electron transport layers, and the in-plane structure of Znq_2 and lack of the polymorphism in the thin film of Znq_2 then result in higher electron mobility than Alq_3 leading to lower turn-on voltages in the OLED devices. Also the devices made of Znq_2 are more stable under the influence of high operating voltages [64,65]. In this respect, Znq_2 is a useful organic complex from the application point of view, it is then of great interest to examine the spin transport properties of this organic compound for possible organic based spin electronic devices.

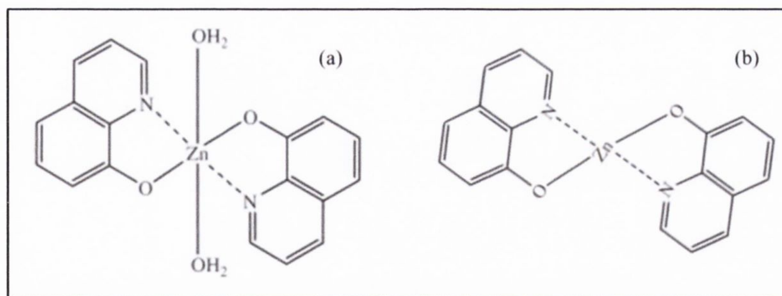

Figure 1.11. Bis(8-hydroxyquinoline) zinc(II), dihydrate (a) and anhydrous bis(8-hydroxyquinoline) zinc(II) (b).

1.4 Organic spin electronics

Organic spin electronics is the combination of two different research fields, spin electronics and organic electronics. In the last two decades, research in these two fields has resulted in some new technological developments and it brought two Nobel Prizes, in chemistry in 2000 (conducting polymers) and in physics in 2007 (giant magnetoresistance). The research in spin electronics involving GMR and TMR is mainly used for the development of information technology to make denser data storage assemblies and non-volatile magnetic random access memories (MRAMs), while the research in the organic electronics (organic light emitting diodes and organic field effect transistors) is used for the development of display technology to make thinner and brighter displays and some other electronic devices. Organic semiconductors offer also many technological advantages thanks to the low cost and easy fabrication process as well as their chemical tunability.

Organic spin electronics combines these two attractive fields adding electron spin functionality the organic semiconductors and investigating the electron spin injection,

transport and detection dynamics in these materials. The weakness of the spin scattering mechanism in organic semiconductors is the exciting point and it is basic to field of organic spin electronics. Ideally, charge carriers would propagate over long distances in the organic semiconductors without losing their spin polarization, if they could be injected properly. This idea promises to make new functional spin based organic devices such as organic spin transistors which could govern future electronic devices.

1.4.1 Life of spin in organics

The spin relaxation times, t_s, and the spin diffusion lengths, l_s, and spin, in organic and inorganic materials are summarized in Figure 1.12, where the data from the published reports is plotted [66-74]. One can see that organic materials occupy the top-left corner of the l_s-τ_s plot, indicating rather long spin lifetime but short spin diffusion length on account of their poor mobility. The spin diffusion length, l_s, in OSCs was often estimated from the modified Jullière's model [66,67];

$$\frac{\Delta R}{R} = \frac{2P_1P_2e^{-\left(\frac{d-d_0}{l_s}\right)}}{1-P_1P_2e^{-\left(\frac{d-d_0}{l_s}\right)}} \tag{17}$$

where P_1 and P_2 are the spin polarization of the ferromagnetic electrodes at the Fermi level, d is the total width of organic layer and d_0 is the total width of the of the Schottky barriers forming at the organic/ferromagnet interface. Injected carriers tunnel through the Shottky barrier into the organic spacer, where they drift and diffuse with exponentially decaying spin polarization. Finally, carriers arrive at the second ferromagnetic layer by tunneling through the second interface. However, some

conceptual and practical problems with this scheme make the estimate l_s unclear [75]. First of all, the conduction mechanism is dominated by the diffusive transport in the organic spacer and exponential decrease of the spin polarization might not be appropriate for organics while Jullière's model describes the tunneling event. Secondly, the model ignores the effects of interfaces which are very important for spin injection. The spin polarization of the ferromagnetic electrodes at both interfaces can be changed by the interfacial effects and the meaning of P_i becomes unclear. Even with these uncertainties, the spin diffusion length could be roughly estimated from the variation of the magnetoresistance of organic spin valves with different organic barrier thickness [76]. However, it is not easy to measure the spin relaxation time directly, but it can be extracted from the layer mobility and spinlife time in a working device. The relation between the spin diffusion length and the spin relaxation time is given by Equation (18).

$$l_s = \sqrt{\frac{k_B T \tau_s \mu(T)}{e}} \qquad (18)$$

where k_B is the Boltzman constant, T is the temperature, e is the elementary charge and $\mu(T)$ is the temperature dependent drift mobility [67].

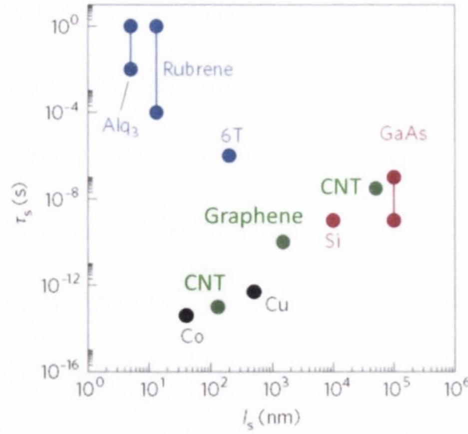

Figure 1.12. Spin diffusion length, l_s, versus spin relaxation time, τ_s, for different classes of materials [22].

1.4.2 Organic spin valves: overview

In the last two decades, organic materials gain much attention in research for new materials which have improved properties for coherent spin transport. The longer spin relaxation time with respect to inorganic semiconductors is the point of attraction for making organic-based spin electronic devices. A large set of experiments has been made on different organic semiconductors to try to study the spin transport mechanism. The most widely used technique is the magnetoresistive effect mentioned in the section 1.2. The room temperature magnetoresistance in an organic compound was firstly reported by Dediu *et al.* on a lateral structure using sexithienly (T_6) which was one of the pioneering materials in OFETs [69]. Basically, the device consists of two 100 nm thick $La_{0.7}Sr_{0.3}MnO_3$ (LSMO) electrodes as spin injector and detector, separated by various sizes of channels ranging from 70 nm to 500 nm. The channels are covered by T_6 thin films to provide electrical connection between the electrodes. Then, the

magnetoresistance is derived from the I-V characteristics which are measured at zero field and high field. They observed a significant room temperature magnetoresistance (30 %) when the channel length was 140 nm and reduced to 10 % at 200 nm, and finally disappeared at 300 nm. This promising result opened an idea that organic materials can offer superior performances in making organic based spin devices. However, some unclear points in the experiment were the absence of the antiparallel alignment of the magnetic layers, and also the linear magnetoresistance displayed by LSMO itself. Later, studies have focused on Alq_3, which is most commonly used in organic light emitting diodes (OLEDs). The possibility of spin injection and detection in Alq_3 was first shown by Xiong *et al.* [66]. The new approach is that the Alq_3 layer (130 nm) is sandwiched between LSMO (100 nm) and Co (3.5 nm) layers making a vertical organic spin valve stack with 2x3 mm^2 junction size. The results showed a clear sign of MR at 11 K (-40 %) for 130 nm thick Alq_3 layer and the MR is persistent up to the 240 nm at the same temperature. There is no clear sign of MR above 200K. This result has brought considerable attention to the spin electronic applications of OSCs. However, the weak temperature dependence of the I-V curve and also the low bias (2.5 mV) across the 130 nm thick barrier cast doubt on the transport mechanism. The interface quality and penetration of the Co atoms into the organic layer presumably influence the transport mechanism. Room temperature MR of -0.15% across a 100 nm thick Alq_3 layer was subsequently observed at room temperature in stacks by Dediu using an AlO_x barrier to separate the Co electrode from the Alq_3 layer [77]. The full stack of LSMO (20 nm)/Alq_3 (100 nm)/AlO_x (2 nm)/Co (35 nm) was deposited into 1x1 mm^2 junction for electrical and magnetotransport measurements and the stack shows a maximum of 11 % negative MR at 20 K. Later, Xu *et al.* [78] studied the spin transport mechanism on a similar stack [66,77]. The stack, LSMO (50 nm)/organic (10-20

nm)/Co (5 nm), was patterned into 0.2x0.2 mm^2 junctions through a shadow mask, where the organic was Alq_3 or TPP (tetraphenyl porphyrin). They observed negative 24 % MR at 11 K and the MR disappeared at 300 K. A new approach is used by Santos *et al.* for spin injection into OSCs to improve the device performance of a tunnel junction by inserting a thin amorphous AlO_x insulating layer at the interface between a bottom Co electrode and the Alq_3 [79]. The stack of Co (8 nm)/AlO_x (0.6 nm)/Alq_3 (t)/NiFe (10 nm) where t = 1, 2, 3 and 4 nm is deposited through in-situ shadow masks into 0.2x0.2 mm^2 junctions and magnetotransport studies have been done in different temperatures ranging from 4.2 K to 300 K. The maximum room temperature MR is recorded as positive 6 % for the 1.6 nm Alq_3 barrier. The positive sign of MR is consistent with the known spin polarization of Co and NiFe thin films [80]. However, Santos et al. noted that 20 nm films of Alq_3 grown directly on Co layer without the AlO_x barrier did not show proper tunneling characteristics and they speculated that the adhesion of Alq_3 was better on AlO_x than the clean Co surface. However, another group was unable to detect any magnetoresistance in Fe/Alq_3/Co structures, where Alq_3 is 25-100 nm and the thickness of the electrodes is 15 nm [81]. The stack is deposited through a shadow mask and the device area is defined by the perpendicular slits resulting in various size junction areas ranging from 2x2 mm^2 to 0.1x0.1 mm^2. First of all, they observed that all devices with Alq_3 thinner than 50 nm were shorted. However, the devices showed 70% yield in the presence of a thin layer of AlO_x at the metal/organic interface even though the thickness of the Alq_3 is 25 nm. This might be due to the better adhesion of organic layer onto the oxide layer [82] or formation of short channels through the organic layer due to the interdiffusion of the metallic atoms deposited on the organic layer [83]. Magnetotransport measurement suggested the absence of the spin transport through the Alq_3 layer in the entire temperature range from 300K to 5 K. Furthermore, the

conductivity mismatch at metal/organic interface prevented the spin injection, and introducing a thin layer of AlO_x at the interface did not improve the spin injection. The contradiction between these earlier results has focused attention to the organic/metal interface.

Vinzelberg *et al*. studied the magnetotransport properties and the physical feature of the LSMO (100 nm)/Alq_3 (0-200 nm)/Co (10 nm) layer stack [83]. They mainly observed that the devices with Alq_3 thinner than 100 nm were shorted and the devices showed 18 % negative MR at 4.2 K when the thickness of the Alq_3 is 150 nm. Furthermore, even though the devices were prepared under the same conditions, same size and same thickness, the resistance changed a few orders of magnitude from junction to junction (from 60 Ω to 1 MΩ). Interestingly, the sign and magnitude of MR also depend on the junction resistance and applied current. They proposed that the inconsistent result was due to the different amount of penetration of the Co atoms into the organic barrier layer. The interface studies proved the formation of Co chains through the organic layer ~ 50 nm deep inside. A one careful study, showing the effect of impurities, defects or pinholes on the magnetotransport or electrical measurements, was made by Yoo et al. using an LSMO (50 nm)/LAO (1.2 nm)/organic (5-20 nm)/Fe (30 nm) layer stack, where LAO is the lanthanum aluminum oxide ($LaAlO_3$) and organic is the rubrene ($C_{42}H_{28}$) [76]. First of all, they made two identical junctions with the size of 0.2x0.2 mm^2 and studied the transport properties in the tunneling regime using a 5 nm rubrene barrier. They measured the dI/dV curves of the devices at 10 K and they observed a zero-bias dip in one of them. The zero-bias anomaly can result from several mechanisms such as localized paramagnetic impurities in the barrier which could serve as scattering centres at low temperature [84], presence of metallic nanoparticles in the barrier which can serve as capacitors resulting in maximum resistance at zero-bias [85]

or localized magnetic excitations in the barrier (magnons) produced by hot electrons [86]. Yoo et al. measured the the MR curves at different biases (10 mV-500 mV) and change of MR sign was only observed for the sample which showed the zero-bias anomaly when the applied bias was 500 mV [76]. Thus, they showed a relation between the change of sign of MR and imperfection of organic barrier. On the other hand, theoretical studies showed that nano-scale pinhole channels introduced in the barrier can even change the sign of MR [87]. An imbalance of transfer rate between the majority and minority spins in the current through the pinhole channels introduces inversion of sign of MR. This was experimentally observed by Mukhopadhyay and Das [88]. Therefore, Yoo *et al*. concluded that changing the MR sign with increasing bias is due to the competition of the pinhole channels and TMR channels in the 5 nm rubrene barrier [76]. Yoo *et al*. also study the magnetotransport through a thick organic barrier layer (20 nm rubrene). They observed very high junction resistance at low-bias at 10 K, and strong temperature dependence of the resistance. In contrast to the earlier reports, they could not see any clear sign of MR at low-bias due to negligible carrier injection and large device resistance. Furthermore, the sign of MR was independent of the applied bias and maximum 14 % MR observed at 10 K when the bias was 0.6 V, suggesting a pinhole free rubrene layer. They could not observe any clear sign of MR at any bias when the thickness of the rubrene layer was 40-50 nm. Overall their results suggest that, in the tunneling regime, nanoscale pinhole channels result in the sign change of MR and beyond the tunneling limit it is possible to inject the spins into the pinhole free rubrene layer (up to the 20 nm) at 10 K.

In general, the size of the active region in the organic spin valves to date ranges from a few hundreds of μm^2 to mm^2, meaning that different effects at the nanometer scale are possible. To rule out any undesirable effect in a large size device and understand

whether the transport is dominated by tunneling or spin injection, Barroud *et al.* introduced a new technique, nano-indentation, which allows one to obtain cross sections a few nm in diameter [89]. An LSMO/Alq_3/Co stack was used in this experiment, similar to most of the earlier works, and the cross section is defined by the diameter of a Co atomic force microscope conducting tip, with a radius less than 10 nm, where a few molecules of Alq_3 covers the interface with the electrodes. The advantage of this method is to allow the well-characterize the transport mechanism in local areas by excluding the many hot-spots in the junction. They reported a maximum 300 % positive magnetoresistance across a 2 nm Alq_3 barrier layer at 2 K, which is the highest MR measured in an organic device. The MR was strongly bias dependent and it dropped to the half value at only 25 mV bias. Furthermore, the MR disappeared completely at 180 K. This experiment makes some critical points about obtaining reliable information and understanding the spin dynamics in organic devices. First of all, in contrast the large size of devices, positive MR was observed, which is expected from canonical spin polarized tunneling theory. This suggests that, in large size devices, different portion of devices contribute the magnetoresistance differently, due to narrow hot-spots in the barrier, which make it difficult to obtain consistent results in organic devices. However, the hot spots do not themselves explain the sign chance of the MR in the organic devices made from the same materials. On this point, Barroud *et al.* developed a model which explains the sign change of MR in the organic devices and Sanvito helped us to understand the physical meaning of the model [90]. The model suggests the formation of new hybrid electronic states which acts as a spin filter when two materials are brought contact, resulting in a change of the spin polarization of the tunnel current. The picture of the DOS of a metal and an organic molecule is presented in Figure 1.13 with and without contact. Whereas the ferromagnet has a broad spin-split

DOS for majority and minority spin subbands, a molecule has discrete molecular energy levels, assuming that only the highest molecular orbital (HOMO) is responsible for conduction. When there is no contact, the Fermi level of the ferromagnet does not interact with any molecular states and the spin polarization of the tunnel current in the hybrid state coincide with the DOS of the ferromagnet. However, the situation is different when they are brought into contact, which broadens the energy levels of the molecule or both broaden and shifts the levels. The broadening arises from the leaking in and out of the electrons in the molecular levels and the lifetime of the each molecular orbital becomes finite. Furthermore, the amount of the broadening for the spin-up and down energy levels in the molecule is different due to the energy offset of the spin-up and spin-down bands in the ferromagnetic electrode. Thus, the broadening of the molecular levels at the Fermi level can present opposite spin polarization with respect to the ferromagnetic electrode. As a second result, the molecular DOS can shift due to the interaction between the molecule and ferromagnetic metal with respect to the Fermi level of the electrodes. In that case, a new spin polarized molecular orbital may appear at the Fermi level of the hybrid state and dominate the current. In Figure 1.13c, the largest DOS at the Fermi level belongs to the majority spins which again dominate the spin current as it is shown in Figure 1.13a. Importantly, the energy scale of the spin filtering effect can be set by the strength of the interaction between the molecule and electrodes, which determines the polarization of the spin current. This results can explain why the MR drops to half value at only 25 mV bias voltage (the corresponding value is ~ 0.5 V in Fe/MgO/Fe tunnel junctions) and about the strong temperature dependence of the MR in the experiments of Barroud *et al.* Also, this model may explain the bias dependence of the MR sign in organic spin valves.

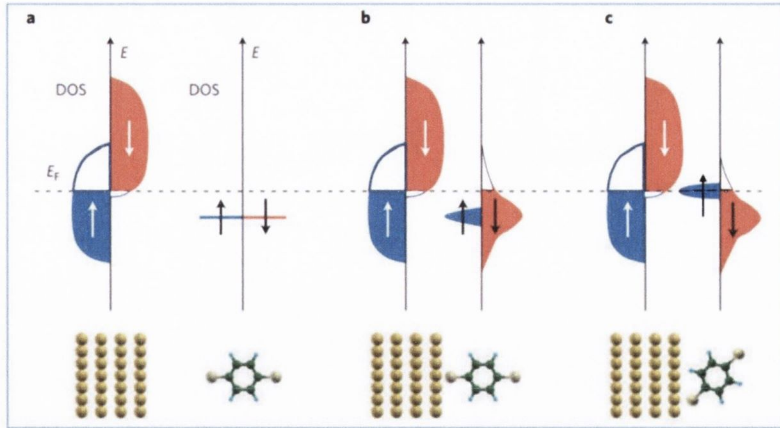

Figure 1.13. Schematic view of an hybrid state at a ferromagnet/organic molecule interface, showing the density DOS of a ferromagnetic metal and an organic molecule when they are isolated (a) or in the contact (b,c) [90].

1.5 Summary

Organic spin electronics is a new and promising research field in its early stage. The experiments so far have shown that the spin dynamics in organic semiconductors are still under debate in terms of spin life time, spin diffusion length, spin scattering mechanisms and spin injection and transport. The discrepancies between the literature data which are obtained from the organic based devices made from same materials push the researchers to study the ferromagnetic/organic interface, which plays an important role for injecting the spins into the organic media. Thus, a parallel research field along with the organic spin electronics arises in order to improve the device performance and understand the possible mechanisms which influence the spin dynamics, namely the 'spinterface'. The works in these fields still continue with the interface engineering and theoretical modeling.

In this thesis, we focus on the organic/ferromagnet interface in order to understand the interface picture, applying the ferromagnetic film thickness magnetization method (FFTM), and we study then the magnetoresistance characteristics of the organic based hybrid devices to understand if it is possible or not to inject and transport the spins in an organic semiconductor. In chapter 2, we present the experimental tools and procedures, which are used to produce organic thin films and devices. In chapter 3, we present the magnetization data of some different ferromagnetic/organic multilayers to study the organic/ferromagnet interfaces using the FFTM method, which reveals the magnetic dead layer when a ferromagnet and an organic semiconductor come into contact. In chapter 4, magnetoresistive and electrical characteristics of the micron-size organic based hybrid devices studied. The devices are produced in two different ways either using photolithography or shadow masking. Future prospects are discussed in Chapter 5.

1.6 Bibliography

[1] M.N. Baibich, J.M. Broto, A. Fert, F.N. Van Dau, F. Petroff, P. Etienne, G. Creuzet, A. Friederich, J. Chazelas, Physical Review Letters 61 (1988) 2472.

[2] G. Binasch, P. Grünberg, F. Saurenbach, W. Zinn, Physical Review B 39 (1989) 4828.

[3] D.C. Ralph, M.D. Stiles, Journal of Magnetism and Magnetic Materials 320 (2008) 1190.

[4] J.G. Simmons, Journal of Applied Physics 34 (1963) 1793.

[5] W.F. Brinkman, R.C. Dynes, J.M. Rowell, Journal of Applied Physics 41 (1970) 1915.

[6] G. Szulczewski, in: R.M. Metzger (Ed.), Unimolecular and Supramolecular Electronics I, Springer Berlin Heidelberg, 2012, p. 275.

[7] W. Thopmson, The Royal Society of London 8 (1856) 546.

[8] M. Julliere, Physics Letters A 54 (1975) 225.

[9] J.S. Moodera, L.R. Kinder, T.M. Wong, R. Meservey, Physical Review Letters 74 (1995) 3273.

[10] T. Miyazaki, N. Tezuka, Journal of Magnetism and Magnetic Materials 139 (1995) L231.

[11] R.C. Sousa, J.J. Sun, V. Soares, P.P. Freitas, A. Kling, M.F. da Silva, J.C. Soares, Applied Physics Letters 73 (1998) 3288.

[12] X.-F. Han, M. Oogane, H. Kubota, Y. Ando, T. Miyazaki, Applied Physics Letters 77 (2000) 283.

[13] W. Dexin, C. Nordman, J.M. Daughton, Z. Qian, J. Fink, Magnetics, IEEE Transactions on 40 (2004) 2269.

[14] A. Schuhl, D. Lacour, Comptes Rendus Physique 6 (2005) 945.

[15] M. Bowen, M. Bibes, A. Barthelemy, J.P. Contour, A. Anane, Y. Lemaitre, A. Fert, Applied Physics Letters 82 (2003) 233.

[16] W.H. Butler, X.G. Zhang, T.C. Schulthess, J.M. MacLaren, Physical Review B 63 (2001) 054416.

[17] S. Yuasa, T. Nagahama, A. Fukushima, Y. Suzuki, K. Ando, Nat Mater 3 (2004) 868.

[18] S.S.P. Parkin, C. Kaiser, A. Panchula, P.M. Rice, B. Hughes, M. Samant, S.-H. Yang, Nat Mater 3 (2004) 862.

[19] D.D. Djayaprawira, K. Tsunekawa, M. Nagai, H. Maehara, S. Yamagata, N. Watanabe, S. Yuasa, Y. Suzuki, K. Ando, Applied Physics Letters 86 (2005) 092502.

[20] Y.M. Lee, J. Hayakawa, S. Ikeda, F. Matsukura, H. Ohno, Applied Physics Letters 90 (2007) 212507.

[21] S. Ikeda, J. Hayakawa, Y. Ashizawa, Y.M. Lee, K. Miura, H. Hasegawa, M. Tsunoda, F. Matsukura, H. Ohno, Applied Physics Letters 93 (2008) 082508.

[22] G. Szulczewski, S. Sanvito, M. Coey, Nat Mater 8 (2009) 693.

[23] K. Hannewald, V.M. Stojanović, J.M.T. Schellekens, P.A. Bobbert, G. Kresse, J. Hafner, Physical Review B 69 (2004) 075211.

[24] R.W.I. de Boer, M.E. Gershenson, A.F. Morpurgo, V. Podzorov, physica status solidi (a) 201 (2004) 1302.

[25] S.F. Nelson, Y.Y. Lin, D.J. Gundlach, T.N. Jackson, Applied Physics Letters 72 (1998) 1854.

[26] M.C.J.M. Vissenberg, M. Matters, Physical Review B 57 (1998) 12964.

[27] R. Coehoorn, W.F. Pasveer, P.A. Bobbert, M.A.J. Michels, Physical Review B 72 (2005) 155206.

[28] W.F. Pasveer, J. Cottaar, C. Tanase, R. Coehoorn, P.A. Bobbert, P.W.M. Blom, D.M. de Leeuw, M.A.J. Michels, Physical Review Letters 94 (2005) 206601.

[29] J. Mei, M.S. Bradley, V. Bulović, Physical Review B 79 (2009) 235205.

[30] N.F. Mott, Philosophical Magazine 19 (1969) 835.

[31] N.F.M.a.R.W. Gurney, Electronic processes in ionic crystals, Clarendon press, Oxford, 1940.

[32] W. Brütting, S. Berleb, A.G. Mückl, Organic Electronics 2 (2001) 1.

[33] P.N. Murgatroyd, Journal of physics D: Applied physics 3 (1970) 151.

[34] P.W.M. Blom, M.J.M. de Jong, M.G. van Munster, Physical Review B 55 (1997) R656.

[35] P.W.M. Blom, M.C.J.M. Vissenberg, Physical Review Letters 80 (1998) 3819.

[36] G.G. F. Farchioni, organic Electronic Materials, Springer 2001.

[37] C.W. Tang, S.A. VanSlyke, Applied Physics Letters 51 (1987) 913.

[38] V.A. Dediu, L.E. Hueso, I. Bergenti, C. Taliani, Nat Mater 8 (2009) 707.

[39] L.S. Sapochak, A. Padmaperuma, N. Washton, F. Endrino, G.T. Schmett, J. Marshall, D. Fogarty, P.E. Burrows, S.R. Forrest, Journal of the American Chemical Society 123 (2001) 6300.

[40] G.B. Kauffman, Coordination Chemistry Reviews 12 (1974) 105.

[41] G.P. Kushto, Y. Iizumi, J. Kido, Z.H. Kafafi, The Journal of Physical Chemistry A 104 (2000) 3670.

[42] M. Colle, R.E. Dinnebier, W. Brutting, Chemical Communications 0 (2002) 2908.

[43] M. Colle, S. Forero-Lenger, J. Gmeiner, W. Brutting, Physical Chemistry Chemical Physics 5 (2003) 2958.

[44] M. Brinkmann, G. Gadret, M. Muccini, C. Taliani, N. Masciocchi, A. Sironi, Journal of the American Chemical Society 122 (2000) 5147.

[45] R.L. Martin, J.D. Kress, I.H. Campbell, D.L. Smith, Physical Review B 61 (2000) 15804.

[46] A. Curioni, M. Boero, W. Andreoni, Chemical Physics Letters 294 (1998) 263.

[47] W. Humbs, H. Zhang, M. Glasbeek, Chemical Physics 254 (2000) 319.

[48] K. Kasuga, M. Tsutsuo, Coordination Chemistry Reviews 32 (1980) 67.

[49] J. Blochwitz, M. Pfeiffer, T. Fritz, K. Leo, Applied Physics Letters 73 (1998) 729.

[50] J. Xue, B.P. Rand, S. Uchida, S.R. Forrest, Advanced Materials 17 (2005) 66.

[51] R. Ben Chaabane, A. Ltaief, C. Dridi, H. Rahmouni, A. Bouazizi, H. Ben Ouada, Thin Solid Films 427 (2003) 371.

[52] M.I. Newton, T.K.H. Starke, M.R. Willis, G. McHale, Sensors and Actuators B: Chemical 67 (2000) 307.

[53] R. Zeis, T. Siegrist, C. Kloc, Applied Physics Letters 86 (2005) 022103.

[54] R.W.I. de Boer, A.F. Stassen, M.F. Craciun, C.L. Mulder, A. Molinari, S. Rogge, A.F. Morpurgo, Applied Physics Letters 86 (2005) 262109.

[55] J. Yuan, J. Zhang, J. Wang, X. Yan, D. Yan, W. Xu, Applied Physics Letters 82 (2003) 3967.

[56] J. Zhang, J. Wang, H. Wang, D. Yan, Applied Physics Letters 84 (2004) 142.

[57] H.S. Soliman, M.M. El Nahass, A.M. Farid, A.A.M. Farag, A.A. El Shazly, The European Physical Journal - Applied Physics 21 (2003) 187.

[58] L. Lozzi, S. Santucci, S. La Rosa, B. Delley, S. Picozzi, The Journal of Chemical Physics 121 (2004) 1883.

[59] Y. Choe, T. Kim, W. Kim, Molecular Crystals and Liquid Crystals 425 (2004) 273.

[60] K.P. Khrishnakumar, C.S. Menon, Materials Letters 48 (2001) 64.

[61] T.A. Jones, B. Bott, Sensors and Actuators 9 (1986) 27.

[62] L.S. Sapochak, F.E. Benincasa, R.S. Schofield, J.L. Baker, K.K.C. Riccio, D. Fogarty, H. Kohlmann, K.F. Ferris, P.E. Burrows, Journal of the American Chemical Society 124 (2002) 6119.

[63] N. Donzé, P. Péchy, M. Grätzel, M. Schaer, L. Zuppiroli, Chemical Physics Letters 315 (1999) 405.

[64] N. Du, Q. Mei, M. Lu, Synthetic Metals 149 (2005) 193.

[65] G. Giro, M. Cocchi, P. Di Marco, E. Di Nicolò, V. Fattori, J. Kalinowski, M. Ghedini, Synthetic Metals 102 (1999) 1018.

[66] Z.H. Xiong, D. Wu, Z. Valy Vardeny, J. Shi, Nature 427 (2004) 821.

[67] S. Pramanik, C.G. Stefanita, S. Patibandla, S. Bandyopadhyay, K. Garre, N. Harth, M. Cahay, Nature Nanotechnology 2 (2007) 216.

[68] J.H. Shim, K.V. Raman, Y.J. Park, T.S. Santos, G.X. Miao, B. Satpati, J.S. Moodera, Physical Review Letters 100 (2008) 226603.

[69] V. Dediu, M. Murgia, F.C. Matacotta, C. Taliani, S. Barbanera, Solid State Communications 122 (2002) 181.

[70] L.E. Hueso, J.M. Pruneda, V. Ferrari, G. Burnell, J.P. Valdes-Herrera, B.D. Simons, P.B. Littlewood, E. Artacho, A. Fert, N.D. Mathur, Nature 445 (2007) 410.

[71] N. Tombros, C. Jozsa, M. Popinciuc, H.T. Jonkman, B.J. van Wees, Nature 448 (2007) 571.

[72] K. Tsukagoshi, B.W. Alphenaar, H. Ago, Nature 401 (1999) 572.

[73] I. Appelbaum, B. Huang, D.J. Monsma, Nature 447 (2007) 295.

[74] J.M. Kikkawa, D.D. Awschalom, Nature 397 (1999) 139.

[75] S. Sanvito, Chemical Society Reviews 40 (2011) 3336.

[76] J.-W. Yoo, H.W. Jang, V.N. Prigodin, C. Kao, C.B. Eom, A.J. Epstein, Synthetic Metals 160 (2010) 216.

[77] V. Dediu, L.E. Hueso, I. Bergenti, A. Riminucci, F. Borgatti, P. Graziosi, C. Newby, F. Casoli, M.P. De Jong, C. Taliani, Y. Zhan, Physical Review B 78 (2008) 115203.

[78] W. Xu, G.J. Szulczewski, P. LeClair, I. Navarrete, R. Schad, G. Miao, H. Guo, A. Gupta, Applied Physics Letters 90 (2007) 072506.

[79] T.S. Santos, J.S. Lee, P. Migdal, I.C. Lekshmi, B. Satpati, J.S. Moodera, Physical Review Letters 98 (2007) 016601.

[80] R. Meservey, P.M. Tedrow, Physics Reports 238 (1994) 173.

[81] J.S. Jiang, J.E. Pearson, S.D. Bader, Physical Review B 77 (2008) 035303.

[82] H.W. Choi, S.Y. Kim, W.-K. Kim, K. Hong, J.-L. Lee, Journal of Applied Physics 100 (2006) 064106.

[83] H. Vinzelberg, J. Schumann, D. Elefant, R.B. Gangineni, J. Thomas, B. Buchner, Journal of Applied Physics 103 (2008) 093720.

[84] J. Appelbaum, Physical Review Letters 17 (1966) 91.

[85] I. Giaever, H.R. Zeller, Physical Review Letters 20 (1968) 1504.

[86] S. Zhang, P.M. Levy, A.C. Marley, S.S.P. Parkin, Physical Review Letters 79 (1997) 3744.

[87] T.-S. Kim, Physical Review B 72 (2005) 024401.

[88] S. Mukhopadhyay, I. Das, Physical Review Letters 96 (2006) 026601.

[89] C. Barraud, P. Seneor, R. Mattana, S. Fusil, K. Bouzehouane, C. Deranlot, P. Graziosi, L. Hueso, I. Bergenti, V. Dediu, F. Petroff, A. Fert, Nat Phys 6 (2010) 615.

[90] S. Sanvito, Nat Phys 6 (2010) 562.

Chapter 2

THIN FILM DEPOSITION, DEVICE FABRICATION AND CHARACTERIZATION METHODS

2.1 Introduction

Fabrication of well-defined thin films is one of the main challenges in thin film research. Quality of the thin films and interfaces are critical for many thin film applications because the physical properties of thin film devices can be modified by defects, impurities or contamination. Therefore, fabrication of devices requires the best deposition conditions such as using high purity source materials and UHV technology. Magnetron sputtering and thermal evaporation are the most widespread techniques for the good quality thin film deposition in UHV conditions. For micron size device fabrication, UV lithography is a suitable technique. In this study, all these techniques have been used for the device fabrication benefitting from the facilities in CRANN. In this chapter, thin film deposition, device fabrication as well as measurement methods will be outlined.

2.2 Thin film deposition

2.2.1 Sputtering process and its basics

Sputtering is one of the most commonly used techniques for thin film deposition. When a solid surface is bombarded by energetic ions (typically an inert gas such as Ar^+), it is seen that surface atoms are removed from the solid surface thanks to the collision with the energetic ions. Then, the ejected target atoms travel some distance in the vacuum chamber until they hit the substrate or chamber wall. Finally, they condense on a solid surface to form a thin film. This phenomenon is known as sputtering.

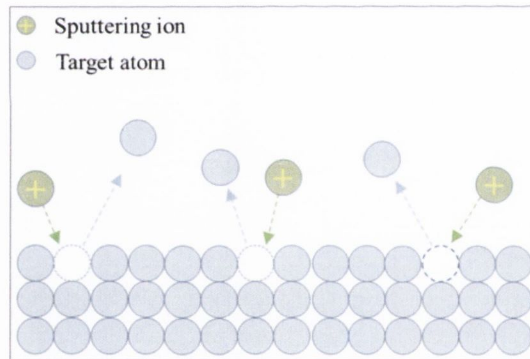

Figure 2.1. Sputtering process, showing the ejected atoms from the target surface as a result of striking energetic ions to the target surface.

Basically, in order to create a plasma which consists of ions and electrons between the target and substrate, argon gas (1-10 mTorr) which is electrically neutral is bled into the chamber and a large enough DC voltage (a hundreds of Volts) is applied between the substrate and target, holding the target at negative voltage and substrate at positive

voltage. Argon atoms are ionized under the electrical potential and they then accelerate towards the target surface and impact the target. Then, the target atoms are released from the surface due to the momentum transfer during the collision and they finally land on the substrate, resulting in growth of films. During this process some extra electrons are also released from the system and they make additional collisions with the argon atoms, which creates more argon ions and more free electrons in the system. The sputtering process is characterized by *sputter yield* (S) which is defined as number of target atoms released per incident argon ion in a certain kinetic energy;

$$S = \frac{\#\, ejected\ atoms\ or\ molecules}{\#\, incident\ ions}$$

The sputter yield depends on (i) the energy of the incident ions, (ii) the masses of the ions and target atoms, (iii) the binding energy of atoms in the solid and (iv) the incident angle of the ions. Furthermore, in thin film deposition, power and pressure are important parameters for the sputtered atoms, to control their initial energy and the number of collisions. The mean free path and also the energy of the atom which reaches the substrate surface can be adjusted by pressure, allowing us to control the thin film properties [1]. Depending on the electrical properties of the materials, DC or RF sputtering can be used. DC sputtering is used for conductors while RF sputtering is used for insulators. The only difference between DC and RF sputtering is that a high frequency (13.56 MHz) RF power supply is used instead of DC power supply. It electrically reverses the anode and cathode in order to prevent the accumulation of charge on the insulator target.

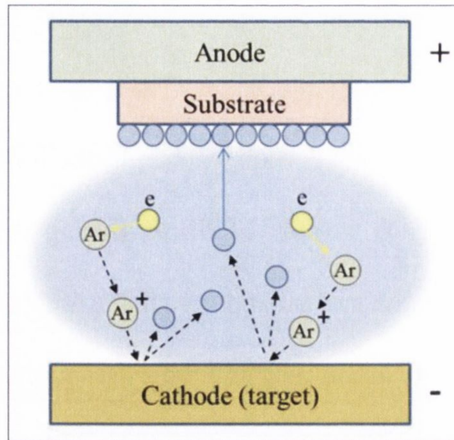

Figure 2.2. DC sputtering system showing the sputtered target atoms and formation of a thin film on the substrate surface.

2.2.2 Magnetron sputtering

Magnetron sputtering is the sputtering method most widely used to enhance the sputtering process. The main difference from normal DC sputtering is that an additional strong magnetic field is created near the target area by placing permanent magnets behind the target to trap and accelerate the electrons around the target. The trapped electrons confine the plasma close to the target area resulting in an increase in the rate of ionization without damaging to the thin film being formed. Using this process it is also possible to get high deposition rates in low argon pressure, which makes for more directional and energetic deposition flux due to the low mean free path of the sputtered atoms. Figure 2.3 shows a schematic picture of the magnetron sputtering system.

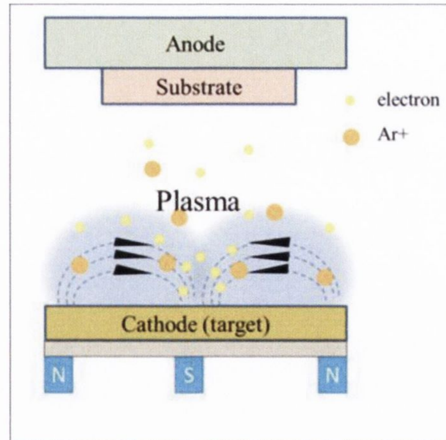

Figure 2.3. The magnetron sputtering system showing the plasma confined near the target area where the magnetic field is strong

2.2.3 Thermal evaporation

Thermal evaporation is one of the simplest and cheapest methods for thin film deposition. The basic idea is to heat the source material using a resistive heater in a vacuum environment, resulting in sublimation or evaporation of the source material. The resistive heater is generally chosen as a filament or boat made of tungsten or molybdenum and it is connected to vacuum feed throughs for a large electric current driven from a DC power supply. The temperature of resistive heater rises together with that of the source material, resulting in sublimation or evaporation. The vacuum allows vapour particles to travel directly towards the substrate where they condense in a thin film form. At low pressure, the evaporated particles can reach the substrate without collision due to the long mean free path of those particles. The kinetic theory of gases helps us to estimate a numerical value for the mean free path in the deposition chambers using the expression of $\lambda \equiv 6/P$ [2], where λ is the mean free path of the

particle in millimetre and P is the pressure given in Pascal. For example, in our evaporation system the pressure during the evaporation is around 1.3×10^{-5} Pascal leading to ≈ 460 meter mean free path which is extremely large when it is compared to the substrate-source distance (~ 0.45 m).

2.3 Thin film deposition systems

2.3.1 The Shamrock magnetron sputtering system

The shamrock sputtering system is an interconnected chamber consists of cassette module (CM), transfer module (TM) and process module (PM). This tool is currently used for metal deposition and it is located in the class 10000 clean room in CRANN. The original part of the tool is the PM which contains a 6 DC magnetron sputtering gun for metal deposition. The base pressure of the PM is around 8×10^{-8} Torr and it is separated from the TM via a slot valve. It is possible to use wafers for thin film growth which are of 150 inches or less in diameter. Normally we use 100 mm wafers. The design of the PM allows loading maximum 4 wafers at the same time and the wafers are rotated during the deposition to get a uniform film. The thin film growth in this chamber is fully computer controlled. The cassette module is initially used for sample loading to the deposition system, where a maximum 16 wafers can be stored. Once the wafers are loaded into the CM, the software waits for pump down until to reach a certain vacuum before opening the slot valve to pick up the wafers. The connection between the cassette module and process module is via the transfer module (TM), including a computer-controlled robot to pick up the wafers from the load lock (cassette

module) and transfer them to one of the deposition chambers. The TM is also connected to the Chamber B and Chamber C. They are custom-designed chambers for the deposition of insulators as well as metals under UHV conditions. The Chamber B includes 6 DC guns for metal deposition and 2 RF guns for the deposition of insulators. A heating capability up to 700 °C is available in this chamber. The Chamber C is used as a wafer transferring chamber from TM to Chamber D which is a custom designed UHV e-beam evaporation chamber. The Chamber D includes a low pressure AJA magnetron sputtering gun which is mainly used or CoFeB deposition and 4 e-beam evaporation pockets which is generally used for MgO, Fe, Au and Cr deposition. Figure 2.4 shows the schematic layout of the whole sputtering system. In this section the sputtering system is only briefly discussed. Readers can look two of the PhD theses for detail of information about this functional tool [3,4].

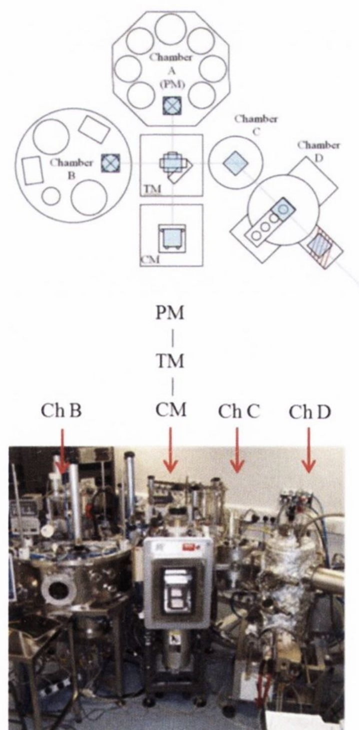

Figure 2.4. The Shamrock system, showing chamber B, C and D as well as a schematic drawing of the whole system

2.3.2 Ultra high vacuum organic & metal thermal evaporation system

Although the CRANN research center includes various state-of-the-art thin film deposition tools, there is no facility to deposit a multilayer organic and metal or oxide layers without breaking vacuum. Depositing the whole multilayer stack in the same system for the magneto-transport studies or interface characterization in UHV condition will give the best results for the investigations. Therefore, we designed a thermal evaporation system under the supervision of Dr. Huseyin Kurt for the organic, metal and oxide deposition, called the *organic UHV chamber*. The chamber was machined by Kurt Lesker Ltd. fully made of stainless steel including, totally 27 CF flanges ranging from 2.75 inches to 12 inches for multiple purposes. Furthermore, it is equipped with a low angle (°5) Ar ion etching gun, an in situ shadow masking system, a triple source temperature-controlled organic molecular evaporation gun, a manually controlled shutter, a quartz crystal monitor (QCM), a sample rotation assembly and a quick entry load-lock which keeps the system under UHV conditions when loading and unloading the wafers. The system is pumped by a Pfeiffer TMH 261 turbo molecular pump which has 250 l/s pumping speed with an Agilent SH-110 backing pump and a Perkin Elmer ion pump. The system is also equipped with heating cables wrapped to outside of the chamber to outgas the water molecules from inner side by setting the power as 45% which correspond to a baking temperature of ~ 100 °C. All these conditions allow the base pressure to go to ~ 2.10^{9} mbar.

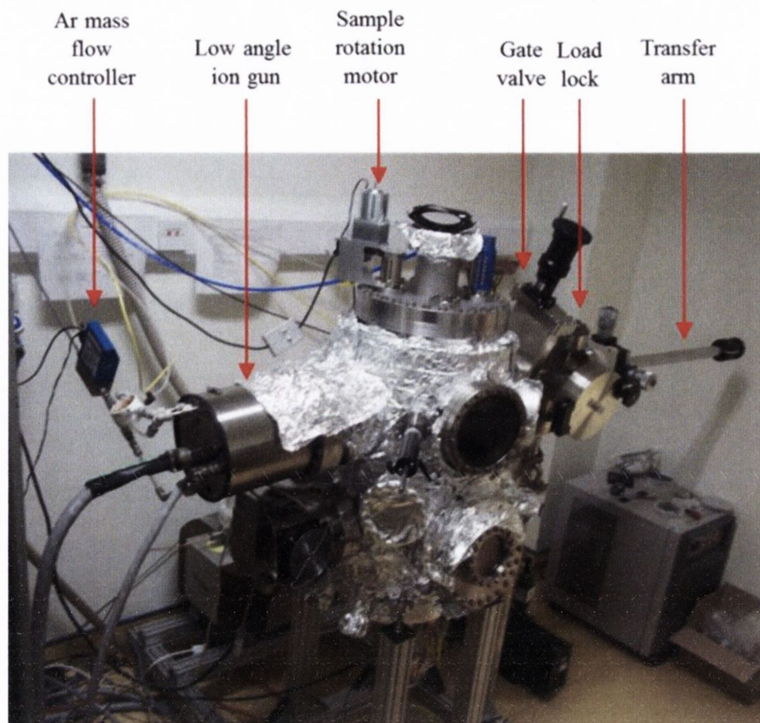

Figure 2.5. Overall view of the organic UHV chamber

2.3.2.1 Material deposition

The organic molecular evaporation gun is designed to deposit organic molecular compounds by thermal physical vapour deposition from a crucible which is heated by a tungsten coil. Various sizes of crucibles ranging from 0.5 cc to 8 cc, which can be used for organic evaporation, are made from Alumina, Boron Nitride, Aluminium Nitride, Graphite or Quartz. The maximum heating temperature of this source is 600 °C, which is large enough to evaporate most of the organic compounds, used and the temperature is controlled by a K-type thermocouple having close contact to the bottom side of the crucible. The crucibles are surrounded by ceramic insulators to concentrate the heat

around the crucible area. The source assembly is designed on a stainless steel base with CF flange for compatible mounting to any standard vacuum chambers.

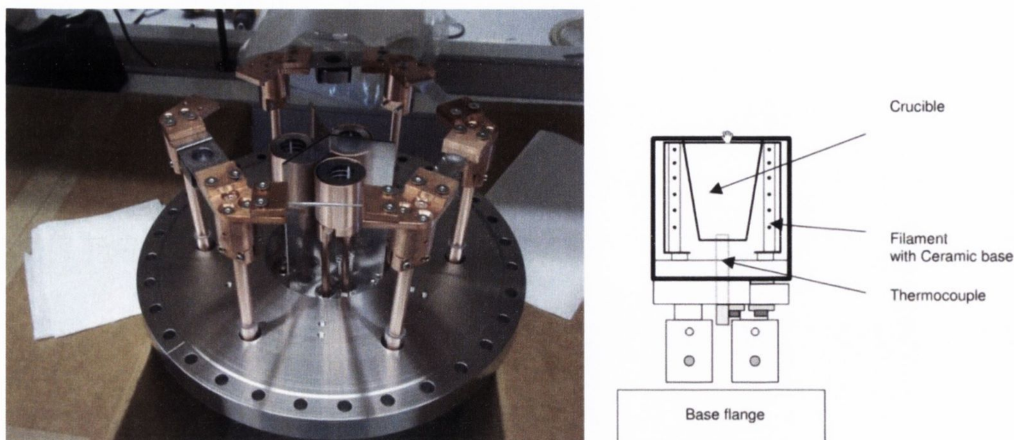

Figure 2.6. The bottom plate of the organic UHV chamber, showing the triple molecular organic evaporation assembly, metal heating sources and a schematic drawing of one of the evaporation pockets in the organic evaporation assembly.

The bottom plate has 6 identical copper feed throughs mounted as heating electrodes 1 cm in diameter allowing to put five different materials for metal or oxide depositions. The evaporation can be made using different methods. First of all, materials can be evaporated from a heated box (metals) placing the pellets inside a crucible. In our system, we use a tantalum microelectronics box bought from Testbourne Ltd. (*ME-19 microelectronics tantalum heating source*). That box can heat the material up to 1600 °C applying 298 Watt. Another option is to use an alumina-molybdenum coated tungsten boat. The inertness of the Aluminium Oxide (Alumina) with most metals and its good heat transfer property are the advantages of the alumina coated sources over uncoated. Molten materials coalesce into a sphere forming a point source and do not wet the alumina surface. In addition, a refractory metal boat using molybdenum with an alumina barrier will increase the desired parameters for evaporation. To obtain an

efficient heat transfer, the evaporant needs to be in a good thermal contact with the boat. The alumina barrier will not allow the evaporant to flow towards the heat sink or to wet the entire boat. In our system, an alumina coated tungsten boat bought from Testbourne Ltd. (*ME3-AO-MO*) is used for metal evaporations. The organic UHV system also allows us to use a metal plated tungsten rod such as chromium. In that case, the material requires less heating power than boat or box heaters due to the intimate contact with the heated tungsten rod.

Aluminium (Al) is one of the cheapest and most abundant metals in the Eart's crust. It is used in many of the industries in thin film or bulk form. However, it is not easy to evaporate Al from a thermal source without damaging the source even though it has a low melting point, 660 °C. The problem is that Al is chemically very reactive with most of the materials so it wets and creates an alloy with the evaporation source material such as tungsten. Suitable thermal sources are Boron Nitride (BN) or Titanium Diboride (TiB_2) crucibles but using those crucibles requires more power to heat Al to its melting point. A tantalum box heater may solve the heating problem but the Ta box cannot be used due to the overflow of the molten Al from the crucible towards that box, results in an expensive process. We solved this problem making a quasi-heating oven around the BN crucible by covering the crucible with a thin molybdenum sheet. First of all, we use Al pellets in this process instead of Al wire. A single pellet is placed into the BN crucible and the crucible is surrounded by 0.125 mm thick molybdenum sheet to encapsulate the heat. After that, the crucible is placed on an alumina-molybdenum coated boat to make deposition. This process is an easy and cheap way to deposit tens of nanometres of Al thin film, and it requires less power. The chamber is also equipped by a baffled box source commonly used for dielectrics such as silicon monoxide (SiO). The advantage of this heating source is that material is sublimed at low power due to

the well-shielded heat providing a uniform sublimation temperature. Furthermore, sublimed particles have an indirect path through a series of baffles before they reach the exhaust chimney. The evaporant material never sees the substrate directly so any change of spitting or streaming which causes pinholes in the thin film are eliminated.

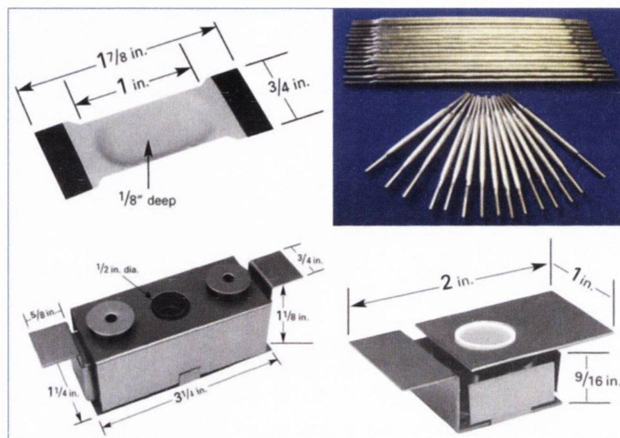

Figure 2.7. Thermal evaporation sources, showing alumina coated boat (top left panel), baffled tantalum box heater (bottom left panel), tantalum microelectronics box heater (bottom right panel) and metal plated tungsten rods (top right panel).

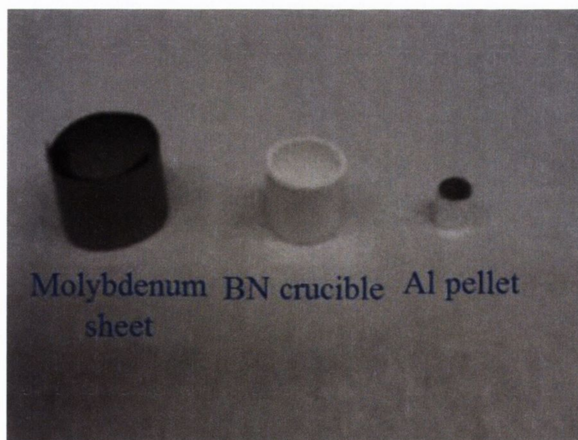

Figure 2.8. Showing the tools for Al deposition. Firstly, single Al pellet is put inside the BN crucible and the crucible is then surrounded by molybdenum thin sheet.

The thermal evaporation sources are heated by electrical current flowing via the 1 cm diameter copper electrodes. The current is driven by a DC power supply which provides 8 Volts and 580 Amps, providing maximum 4.64 kW power. As it is seen from Figure 2.9, the heating cables and copper electrodes are connected using a movable copper clips which have small channels for water flow to cool down the electrodes and heating cables. The cooling water is supplied by a chiller setting the temperature to 10 °C and maximum water pressure is 4 bar.

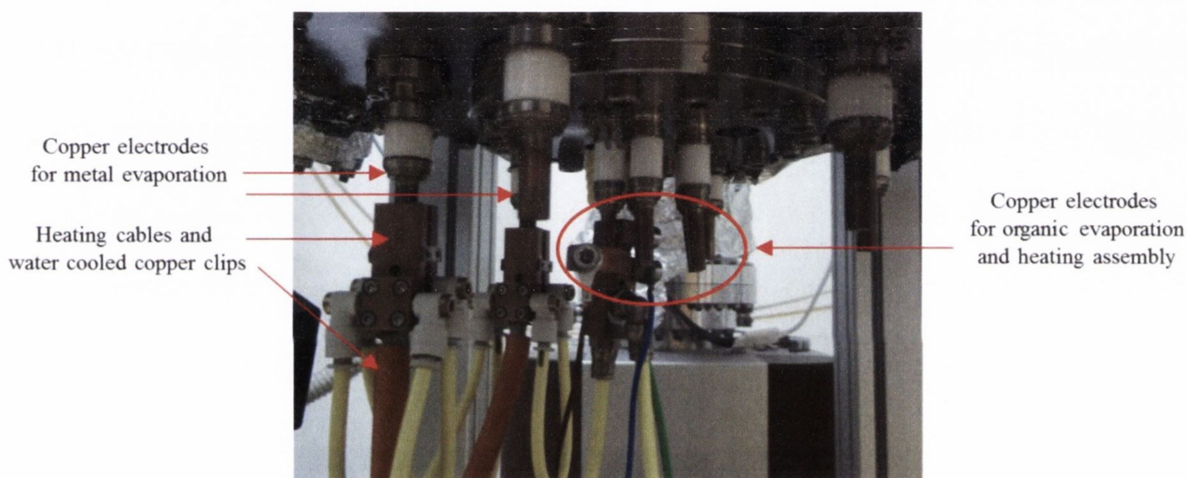

Figure 2.9. The bottom side of the organic UHV chamber showing the electrical and cooling connections

2.3.2.2 Thickness measurement

When the chamber is ready for material deposition, the evaporant material is heated up and thickness of the deposited film is measured using a quartz crystal monitor (QCM) which is a *STM-100/MF thickness-rate monitor* supplied by Sycon Instrument. The resolution of the QCM is 0.1 Å/s and the deposition parameters can be saved for 9

different materials in its memory. These materials tooling factor, density of evaporant or z-factor. The QCM is fixed in a position near the substrate and it is calibrated making two trial samples. Firstly, material density and z-factor related to evaporant, which can be found in the sheet provided by company, are set in one of the 9 memories (marked as *'program'* in the QCM) adjusting the *tooling factor* as 100. Then, the material is deposited and the thickness is read from the monitor (generally 10-15 nm). To check the real thickness, XRR measurement is performed on the sample and the tooling factor is recalibrated using the QCM and XRR values. The tooling factor is calculated using the following expression.

$$Tooling\ factor = \frac{thickness\ readed\ by\ QCM}{thickness\ measured\ by\ XRR} x100$$

The tooling factor can be bigger or less than 100 depending on the substrate and QCM positions (it is less when the QCM is placed between substrate and heating source). In the next step, a new sample is prepared using a new tooling factor and the real thickness is measured using XRR to double check the thickness. If the fraction of thickness values obtained by QCM and XRR is less than 5%, the calculated tooling factor can be used for the experiments otherwise the tooling factor needs to be recalibrated until the ratio of d_{QCM}/d_{XRR} is less than 5% for accurate thicknesses.

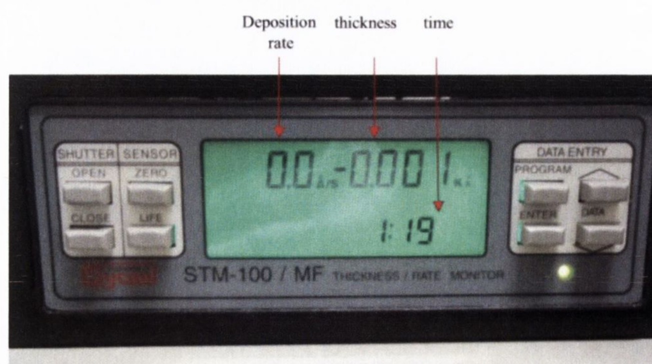

Figure 2.10. The thickness/rate monitor (QCM)

2.3.2.3 Load-lock and sample loading

Sample loading to the organic UHV chamber is via through a load-lock which is isolated from main chamber via a UHV gate valve. The load-lock is pumped by a small turbo molecular pump (46 l/s) and a scroll pump which lower the pressure to ~5×10^{-7} mbar. One high purity oxygen line for oxidation processes and one nitrogen line for ventilation are connected. The load-lock is equipped with a magnetic transfer arm mounted to an X-Y micro manipulator stage to move the sample up and down or left and right as well as to transfer the sample to the main chamber under vacuum. A circular substrate holder made of copper is used for holding the samples at maximum size 75 mm in the chamber. A stainless steel head is attached to the end of the transfer arm to hold the copper substrate holder (see Figure 2.12). When the load-lock and the main chamber is under the vacuum, the gate valve is opened safely and the substrate is transferred to the main chamber via the transfer arm. The main chamber has a special assembly designed for the substrate holder to keep the sample inside during deposition, which is made of stainless-steel and mounted on a rotational stage via 3 rods on the top side keeping the substrate source distance at ~45 cm. The sample is placed in the correct position using the micro manipulators and the transfer arm is retracted.

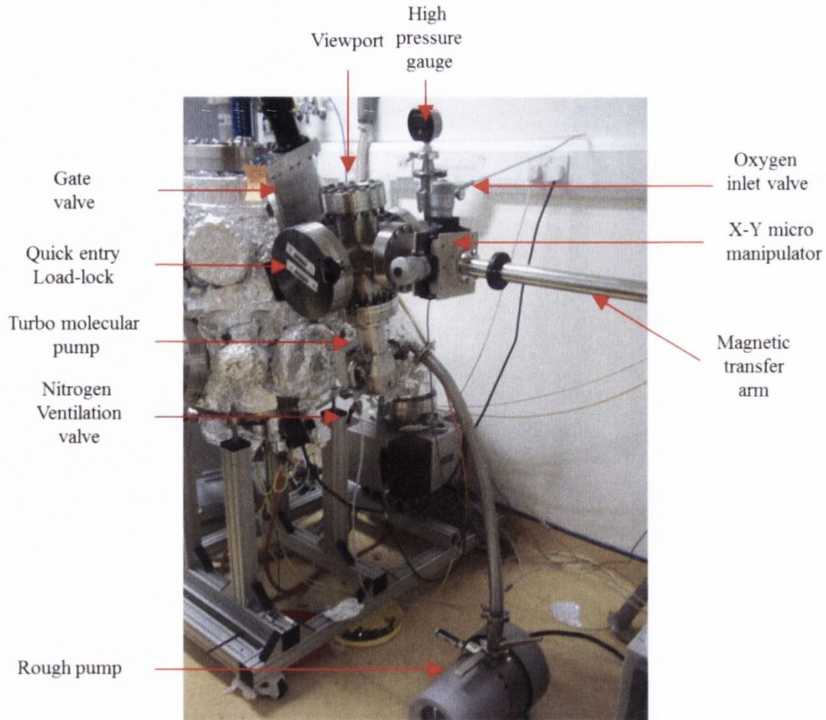

Figure 2.11. The picture of the load-lock showing its assembly

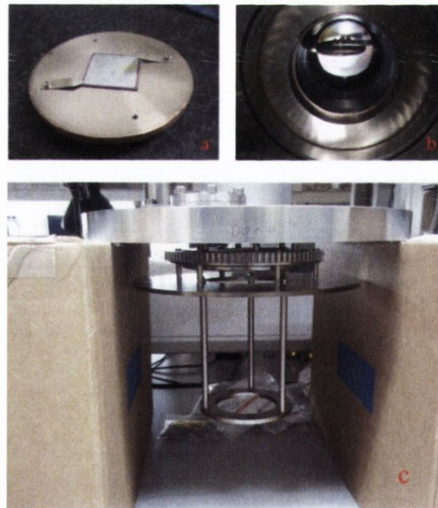

Figure 2.12. Sample mounting and transferring. A 25 mm SiO_2 wafer is attached on the copper substrate holder (a), the substrate holder is mounted on the transfer arm in the load-lock (b) and the rotational assembly to hold the substrate in the main chamber (c).

2.3.2.4 In situ shadow masking system

One of the desired ways for device fabrication is to fabricate the entire device under vacuum conditions. In situ shadow masking is the most commonly used method for this purpose due to the ease of use and cheaper processing. Therefore, an in situ shadow masking system is incorporated in the organic UHV system for device fabrication. The masking system basically consists of a shadow mask, mask holder and a linear shift mechanism to move the mask back and forth. The shadow masks are machined from 50 micrometre thick and 37 mm x 72 mm in size stainless-steel sheets which contain various sizes of cut-outs, which was supplied by Laser Micromachining Ltd. The size of the cut-outs changes from 0.1 mm to 3 mm to create stripes, giving different size of junctions. The mask holder is also made of stainless-steel, 1 mm thick, and it is 105 mm x 40 mm in size with a central aperture to fit the mask. The central aperture is a counter-sunk border, 1mm wide and 0.06-0.08 mm deep and the holder is mounted to the linear shift mechanism via a rod. The linear shift mechanism gives totally 10 cm freedom to move the mask back and forth and ± 5 mm in the up and down direction. It is also equipped with a digital scale which has micrometre resolution to adjust the accurate position of the mask below the sample surface.

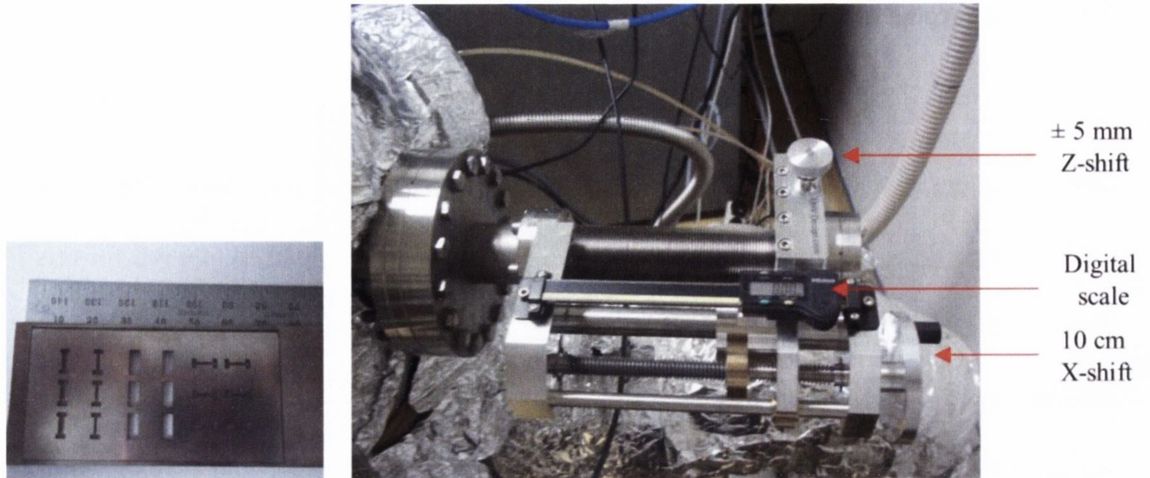

Figure 2.13. Picture of the shadow mask and linear motion mechanism

2.3.2.5 Argon ion gun

One of the main parts of this thesis focuses on the MgO/organic based magnetic tunnel junctions. The sample preparation requires to use both the Shamrock sputtering tool and the organic UHV chamber together due to the lack of an MgO evaporation facility in the organic UHV chamber. This process results in exposing the MgO surface to the air and forming a thin $Mg(OH)_2$ (magnesium hydroxide) layer at the surface, which destroys the spin polarized transport. To remove that thin layer of $Mg(OH)_2$ before evaporating an organic film, an Ar ion cleaning process is performed to sample. As we will discuss in Chapter 4, this process increases the TMR ratio from 14% to 120% depending on the cleaning time. The ion gun is positioned at a small angle (5°) with respect to substrate plane and a low beam voltage is set in order to obtain uniform and soft cleaning. After the stack is prepared up to the MgO layer in the Shamrock sputtering tool and exposed to a subsequent annealing process, it is safely loaded into organic UHV chamber. Firstly, using the gas valve labeled in Figure 2.14, Ar gas is let

to flow inside the chamber, setting the flow rate as 0.83 sscm, increases the pressure up to 2.4×10^{-4} mbar. The parameters used in the cleaning process are summarized on Table 2.1. To achieve a uniform cleaning, the substrate rotation is kept at 'ON' position and the shutter must be retracted from the sample area. For the next users of the organic UHV chamber, it is worthwhile to describe Ar ion the cleaning process step by step.

1. Load the substrate into the chamber safely and make sure that shutter is in the retracted position and the substrate rotation is 'ON'.
2. Check the water cooling. This is not connected to the chiller. The water is supplied from PCW connected to the next door (follow the water pipe connected to the ion gun)
3. Shut down the ion pump and ion gauge
4. Open the Ar gas valve on the wall, the gas inlet valve connected to the chamber (green valve) and the gas flow meter on the rack.
5. Set the gas flow meter to 0.83 sscm and wait 2-3 minutes to stabilize the pressure at 2.4×10^{-4} mbar (now you can open the ion gauge).
6. Switch the power button to the position '1' on the power supply.
7. Press the 'source' button.
8. Switch the mode button to 'manual'.
9. Adjust the parameters which are written in Table 2.1 using the 'adjust' button. You can jump between the parameters using the 'module' and 'function' buttons. For faster cleaning the energy of the ion beam can be increased playing with the parameters.
10. Press the 'beam' button to start the cleaning process.
11. When you finish the cleaning, press the 'beam' button to stop the beam.
12. Press the 'source' button.

13. Switch the power to the position ‘0’.

14. Close the gas inlet valve connected to the chamber (green valve), the Ar gas valve on the wall and the gas flow meter on the rack.

15. Open the ion pump.

16. Close the substrate rotation and shutter.

17. Safely unload the sample.

Beam voltage	Accelerator voltage	Beam current	Accelerator current	Neutralizer current	Neutralizer filament current	Cathode current	Gas	pressure
200 V	300 V	18 mA	4 mA	20 mA	2.80 A	3.35 A	0.83 sccm	2.4×10^{-4} mbar

Table 2.1. Ion gun parameters used for cleaning the MgO surface

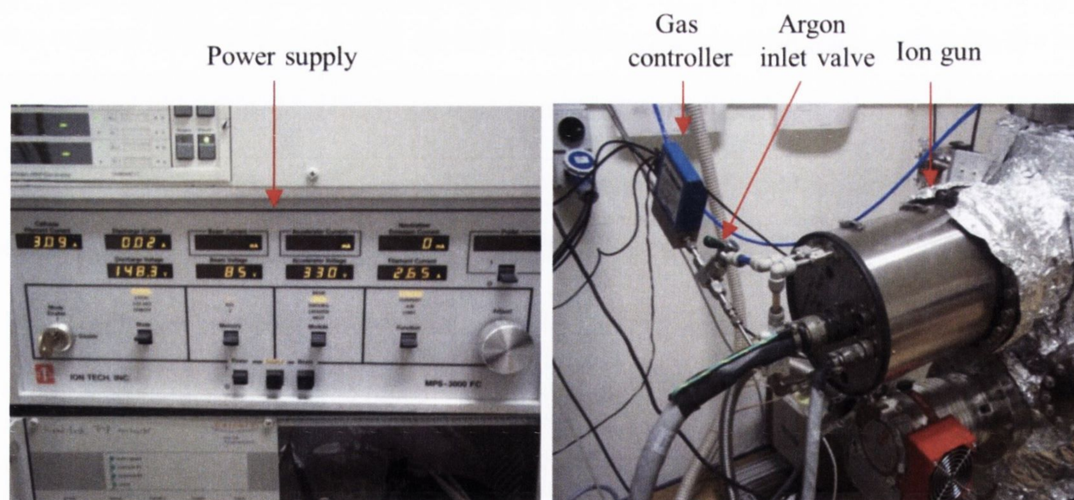

Figure 2.14. Picture of the ion gun and its power supply.

2.3.3 Other organic evaporation systems

In this part the other evaporation systems used during the PhD. study for metal-organic deposition are briefly mentioned. The functionality of those tools is not as good as the *organic UHV chamber* but they were the only possibility for organic-metal deposition before building up the *organic UHV chamber*.

2.3.3.1 The Camellia

The Camellia is a purpose-built organic-metal evaporation system which was built up by Prof. Gregory J. Szulczewski who worked in the Spin Electronics and Magnetism group as a sabbatical visitor in 2008-2009. The name of 'Camellia' represents the state flower of Alabama (US) where the chamber is originated. The organic evaporation in this tool is simply via heating the alumina crucible with a tungsten basket heater. The temperature is heated up carefully to start deposition and the film thickness is read by the QCM which is positioned near the substrate. The sample is held by an extra magnetic arm which is sitting in the deposition chamber. For metal deposition generally Co and Al are used. Co thin films are deposited by bombarding a Co rod. The Co rod is kept at a high positive voltage and it is surrounded by a tungsten wire kept at a negative voltage. When the tungsten wire is heated up, electrons are released and accelerate towards to the Co rod. Finally, the rod is bombarded by the electrons to remove the target atoms from the surface. On the other hand, Al films are evaporated from an aluminium wire which is wrapped on a spiral shaped tungsten heater, aiming to cap the other films from oxidation. Al can be easily evaporated due to the low melting point

(660 °C) with respect to Co (1495 °C) so a small power applied to the tungsten heater is melt and evaporate the aluminium. The disadvantage of this method is that the evaporant is quickly used and molten Al creates an alloy with the tungsten. Therefore, the vacuum needs to be broken in every week to change the evaporant as well as tungsten filament.

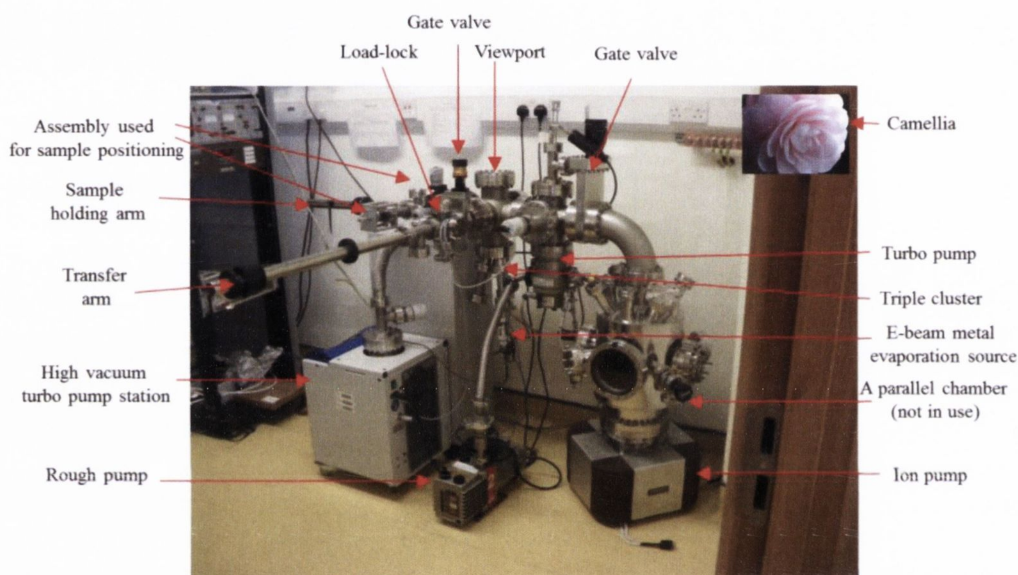

Figure 2.15. Picture of Camellia

2.3.3.2 Organic evaporator

This tool is another purpose-built chamber for organic-metal evaporation as a joint work with Dr. Simone Alborghetti. The tool is equipped by a four-port cluster used for connection the evaporation cells. The process of deposition of organic materials and aluminium are the same as with the Camellia and they are simply evaporated by heating the alumina crucible or tungsten filament, respectively. However, the deposition of Co

is via a Knudsen-cell which easily controls the temperature of evaporant material and is commonly used in molecular-beam epitaxy. A magnetic transfer arm and a micromanipulator provide to transfer the samples from load-lock to deposition chamber and safely adjust the position of the substrate before deposition. The vacuum of the chamber can reach ~5×10^{-9} mbar using a Leybold turbo molecular pump which has 400 l/s pumping speed. The load-lock and its assembly mounted on this chamber was the same one which used in the organic UHV chamber.

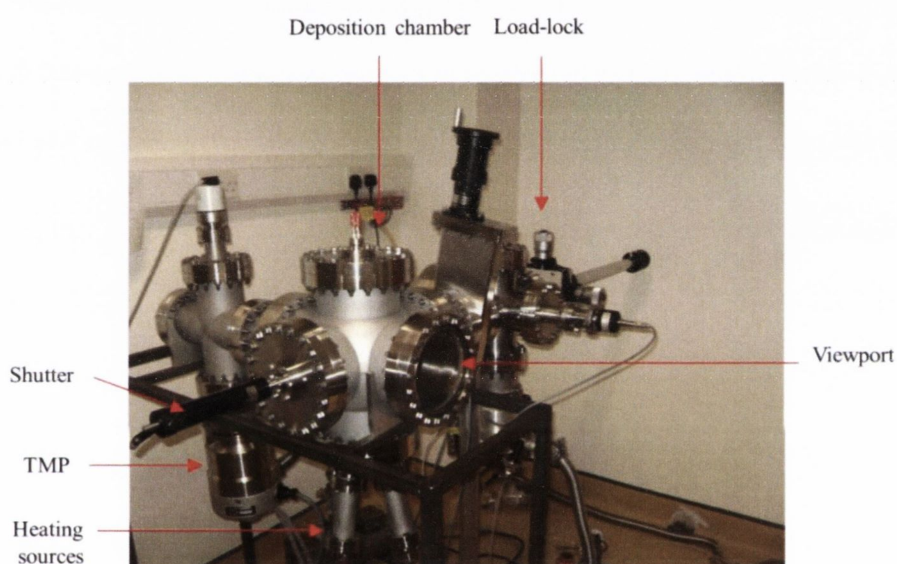

Figure 2.16. Picture of the organic evaporator.

2.3.3.3 Bell-jar evaporation system

The bell-jar evaporation system built by Dr. Franklyn Burke was the earliest system for organic evaporation in our group. It includes two thermal sources isolated from each other by a thin sheet to minimize the contamination. Organic materials are evaporated from a crucible which is placed into a tungsten basket heater positioned between two

copper electrodes. The system is also equipped by a tungsten substrate heater as well as three K-type thermocouples which are placed very close to the heating sources and substrate to control the temperature during the process. The film thickness is measured by a Q-pod QCM which is connected via a USB port to a computer. The substrate source distance is ~10 cm so the system is suitable for small-size substrates to get a uniform film thickness. To heat the electrodes, current is supplied by a Wayne Kerr AP6050A power supply which provides a maximum 1.5 kW power. The system is pumped by a high vacuum turbo pump station which can give a chamber pressure ~ $5x10^{-6}$ mbar. A manually controlled shutter placed between the substrate and heating source as well as a gas injection feedthrough are the other components of the bell-jar evaporation system.

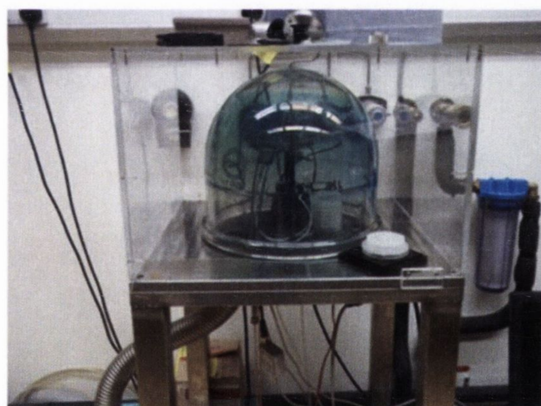

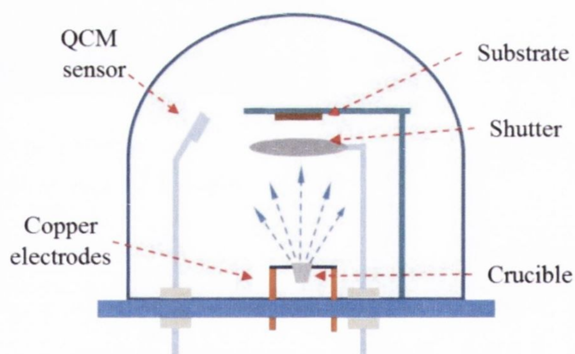

Figure 2.17. The bell-jar evaporation system and a schematic drawing

2.4 Device fabrication techniques

In this work, a large majority of the spin electronics devices are fabricated into micron size junctions in order to characterize the spin based transport properties. Two different processes, UV-lithography and shadow masking, are used for micro-fabrication and their details are explained in this section.

2.4.1 Photolithography technique

2.4.1.1 UV lithography and general basics

The UV-lithography process is the most widely used technique for fabrication of micron-scale features on a substrate using a photosensitive resist and a metal mask. A metal mask is designed with the desired micro-scale features patterned on a transparent glass or quartz substrate using a thin layer of chromium [5]. Basically, the metal features patterned on the glass block the UV light produced by a mercury arc lamp and allow the beam to pass through only in some specific areas to reach the photoresist spun on a substrate. The wavelength of the UV light can be in three different forms depending on the energy, they are called as g-line, h-line and i-line for the 436 nm, 405 nm and 365 nm wavelength, respectively [6]. In this work, 365 nm UV light is used for all UV exposure processes. The features patterned on the mask are transferred to the substrate, when the UV light reacts with the photoresist. Photoresist is a light sensitive polymer reacts with specific solvents. Depending on the type of photoresist, the exposed or unexposed areas dissolve in a chemical solution called a developer. In the

case of positive photoresist, the exposed area dissolves in the developer while the unexposed parts remain stable. In this study, Shipley S1813-G2 positive is used.

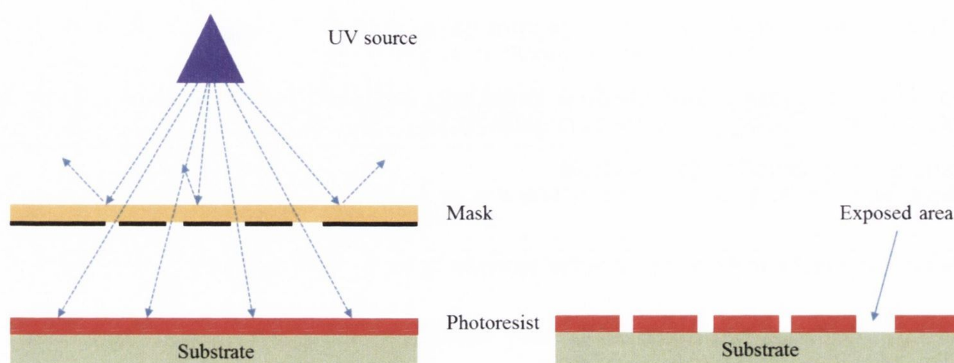

Figure 2.18. UV exposure, showing the UV light passing only from some specific areas through the metal mask; the features on the mask are transferred to the substrate after developing.

2.4.1.2 OAI mask aligner

A mask aligner is used to hold the wafer and mask in a specific position to expose the desired area to the UV radiation. For single step patterning, it is easy to align the mask and substrate but the situation is not so easy when the multi-step patterning is considered. The OAI Model 800 CE mask aligner located in the CRANN Class 100 clean room is used in this study to perform the photolithography. It is a typical contact printing tool providing ~ $20mW/cm^2$ light intensity for the exposure process. It has three different exposure modes: soft contact, hard contact and vacuum contact. In the case of soft contact there is no mechanical force between the substrate and the mask, while nitrogen gas is used to press the substrate against the mask in the hard contact mode. In the vacuum contact mode, the space between the substrate and the metal mask

is pumped and the substrate is pressed against the mask by the atmospheric pressure. The highest resolution is obtained using the vacuum contact (less than 2μm).

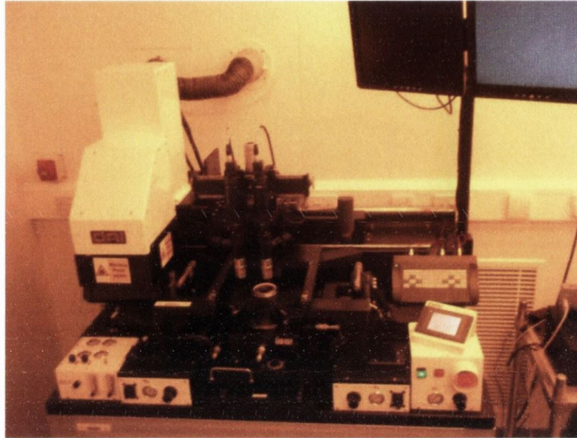

Figure 2.19. The picture of the OAI mask aligner

2.4.1.3 Argon Ion milling and Millatron

Ion milling is simply used for etching the samples by using energetic ions which are produced by an ion gun and accelerated towards the target by a strong electric field. The method is similar to sputtering aiming at removing the target atoms from surface. Milling is one of the necessary steps of the UV lithography process to remove unprotected films from the samples. The tool used for milling purpose in this study is the Millatron located in the SNIAMS building. It is a broad-beam ion milling tool equipped with an Argon ion gun producing the Argon plasma, a secondary electron mass spectrometer to monitor the etched materials in the system and a substrate rotation stage to obtain uniform etching. Also, the sample holder can be tilted from 0° to 90° with respect to the ion beam, which allows the samples etched at different angles. The

system is pumped by a cryogenic pump and the typical base pressure and the operating pressure are ~ 10^{-7} Torr and ~10^{-4} Torr, respectively. For the detailed information, readers can see Ref. [3]. In this study, RF power of 300-400 W is used for the all ion milling processes.

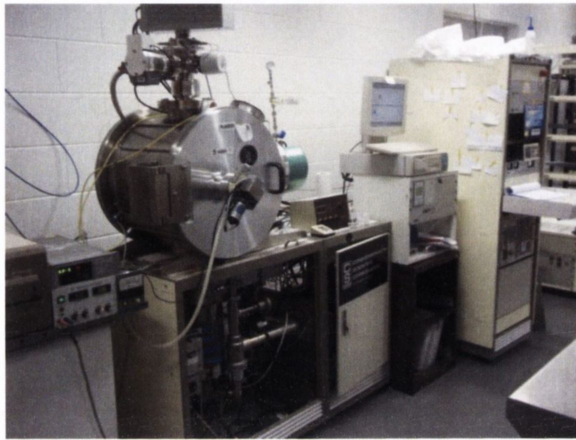

Figure 2.20. Picture of the Millatron

2.4.1.4 Device fabrication by UV lithography

In order to characterize the electrical and magnetic properties of the samples, they need to be patterned into micron size junctions. At this point, UV lithography and Ar ion etching are the conventional state of the art techniques used to obtain high quality small size junctions. These full stacks were patterned by three-step UV lithography with junction sizes ranging from 4 x 4 μm^2 to 50 x 150 μm^2. Also, the patterning process includes two-step Ar ion milling and two-step oxide depositions. These steps, basically, define the bottom contact, junction area and top contact. The details of the patterning process are explained below:

1. Positive photoresist (Shipley S1813) was spun on the samples by spinning at 3000 RPM to create a uniformly spread 1500 nm thick layer of photoresist on the sample. The sample is then placed on a hot plate to dry excess solvent from the photoresist. The hot surface is kept at 115 ºC and the sample is heated for 2 minutes. This process is called *soft-baking*. After that, the sample is moved to the OAI mask aligner to expose it with 365 nm UV light (i-line). The sample and the first photomask are brought into contact using the vacuum contact mode of the mask aligner to expose to UV light for 5 seconds. 24 dog-bone shapes are designed on the photomask to create the bottom contacts. The mask does not allow the UV light to pass through that dog bone area but all the rest of the sample surface is exposed to the UV light to make the resist soluble in a special solvent which is microphotoresist developer MF-319. Next, the sample is immersed into the solvent to remove the photoresist from the exposed area. The exposure takes ~ 40 sec until the pattern is clearly seen on the substrate and finally the sample is cleaned from the developer using deionized (DI) water.

   The sample is now ready for milling to etch the unprotected area using Ar ions. To do this, the sample is placed in the Millatron and etched down to the Si/SiO_2 substrate. The angle between the beam and the sample surface is kept at 75° and the etching is controlled by an End Point Detector (EPD) monitoring the etched layer. When the milling is successfully accomplished, a thick oxide layer (either SiO_2 or SiO) is then deposited using either the Shamrock sputtering tool or the organic UHV chamber just above the barrier layer to protect the organic layer from any solvent in the following steps. Then the oxide layer and the photoresist are removed from the dog bone structure by lifting off using acetone and IPA (iso proponol alcohol).

2. The junction areas were defined by the second lithography process. The soft-baking, development and UV exposure parameters are the same as in section 1. However, the only difference is that a second photomask is used to define the mesas. The photomask includes various sizes of square or rectangular shapes ranging from 4 x 4 μs^2 to 50 x 150 μm^2. The positive photoresist was spun again onto the sample using a spinner which again rotates the sample at 3000 RPM and soft-baked on the hot plate. It is then exposed to UV with the second photomask defining the mesas and the resist is developed in the MF-319 developer. Later, it is Ar ion milled down to barrier and 50 nm SiO_2, which was removed later from mesas by lifting off using acetone and IPA, deposited to isolate the bottom stacks.

3. A final exposure and development step creates strips for the top contacts. Here, the third photomask is used in the lithography process, keeping the same all the other parameters. A Ta(5nm)/Cu(50nm) bilayer was sputtered to form the top contacts and the lithography was successfully finished in the last lift-off step using acetone and IPA. Figure 2.22 shows the lithography steps which were used in this study.

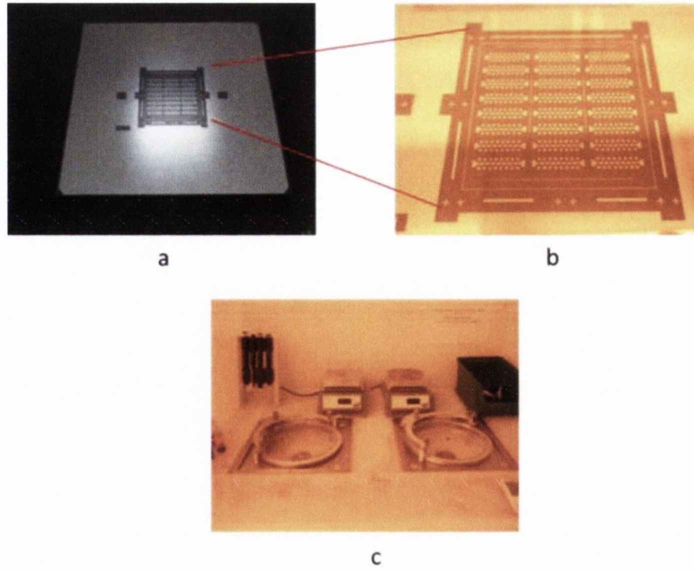

Figure 2.21. A picture of the first UV photomask (a) and zoom in (b). (c) shows the spinner and the hot plate for soft-baking.

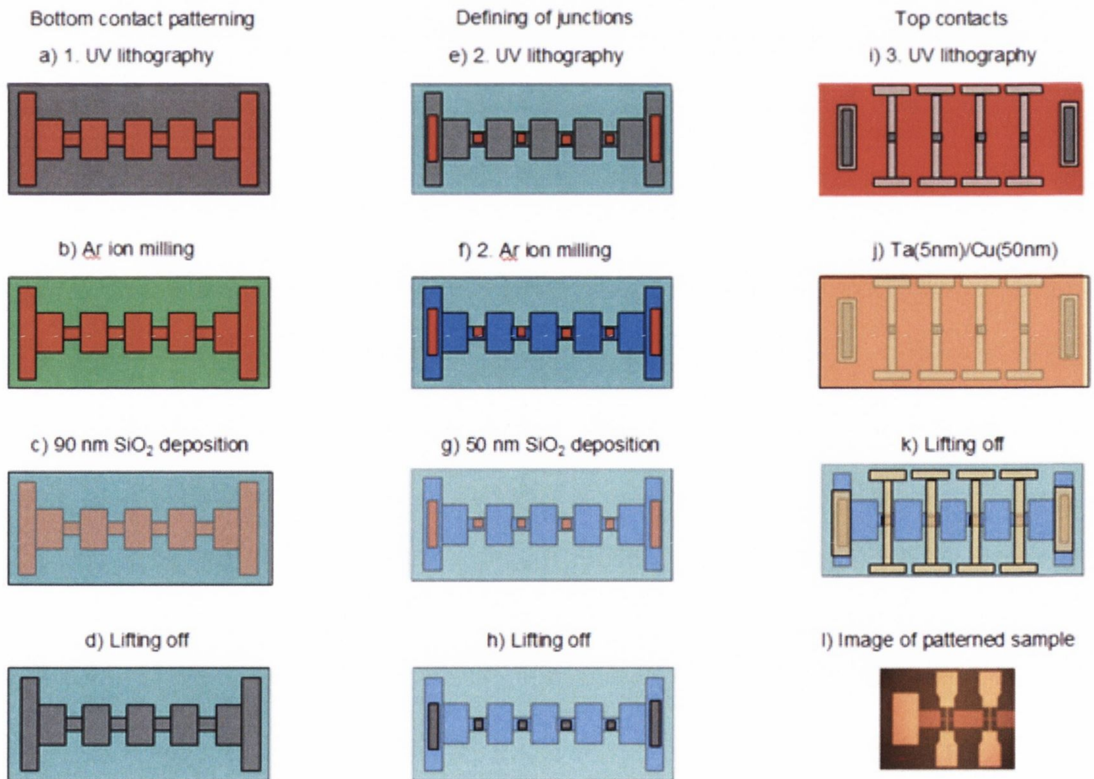

Figure 2.22. Device patterning process

2.4.2 In-situ shadow masking technique

The shadow masking technique is used to make a standard cross configuration for a wide range of vacuum chamber evaporations. The electronic devices can be easily fabricated under the vacuum conditions by patterning the bottom and top electrodes into rectangular strips which are perpendicular to each other, and the barrier is sandwiched between the electrodes. The active area of the devices is determined by the overlapping of the electrodes.

In this study, devices are fabricated using a stainless-steel shadow mask described in the section 2.3.2.4. Firstly, the shadow mask is placed between the substrate and source material using the micro-scale feedthrough. The gap between the substrate and the mask is ~ 2 mm and the shutter is kept closed until the deposition starts. When the evaporation starts, the shutter is opened and the first ferromagnetic layer is deposited through the mask to create the strips. When the strips are created, the mask is retracted and the barrier layer is evaporated on the whole substrate, keeping the substrate in rotation which allows covering the side walls of the bottom electrode. Then, the mask is again placed under the sample to deposit the top ferromagnetic electrode into the strip form, such a way that the bottom and the top stripes overlap to create the active area. Hence, 6 junctions are produced in each batch. The junction sizes can change from 0.1x0.1 mm^2 to 3x3 mm^2 depending on the used shadow mask.

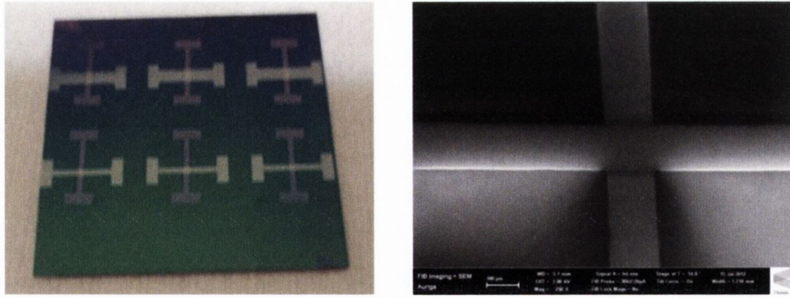

Figure 2.23. Junctions produced by shadow masking technique and an SEM image (the scale bar is 100 μm)

2.5 Characterization techniques

2.5.1 The Resistance-Temperature (R-T) rig

The R-T rig is a home-made electrical measurement setup generally used for I-V and magneto-transport studies. It consists of a Keithley 2400 sourcemeter, a cryostat, a temperature controller, an electromagnet and a computer which monitors and saves the measured data. It is possible to measure the I-V characteristics of the samples which have the resistance up to a few megaohms. The electromagnet can provide maximum ± 180 mT magnetic field for the magneto-transport or extra ordinary Hall Effect measurements, and a Kepko 10 ampere bi-polar analogue power supply is used to produce the magnetic field. Also it is possible to make low-temperature electrical measurements using the cryostat system. A closed-cycle helium gas compressor connected to the cryostat cools the cold head to 15 K and the temperature between the 15 K and 300 K is controlled by a *cryo·con 34* temperature controller. Otherwise, a high-impedance Quantum Design PPMS (physical property measurement system) located in the CRANN 2nd floor is used for high resistance measurements (100 GΩ).

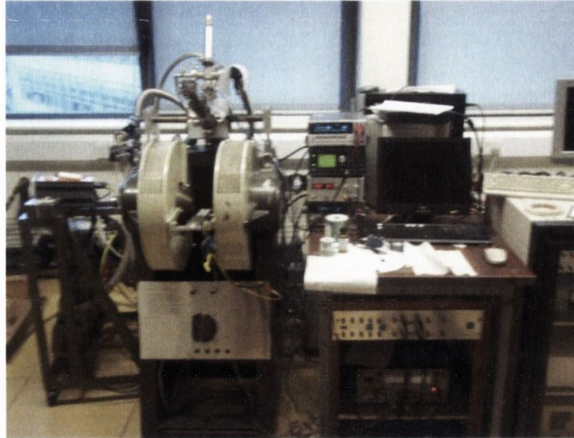

Figure 2.24. The picture of the R-T rig

2.5.2 SQUID magnetometer

In this study, magnetic properties of the samples are all measured using a Quantum Design Magnetic Property Measurement System (MPMS XL5). This is an ultra-high sensitivity SQUID (Superconducting Quantum Interference Device) magnetometer with 10^{-11} Am^2 resolution and maximum field of 5 T, making it ideal for low moment measurements. It includes a high field superconducting magnet, a temperature controller unit and a computer operating system. The superconducting components are cooled by liquid helium and the minimum operating temperature of the system is 1.8 K. The samples are produced onto a 5 x 5 mm^2 Si/SiO_2 substrate and loaded into the SQUID via a plastic straw. Generally, the hysteresis curves are measured to determine the saturation magnetisation of the samples for the dead layer investigations explained in Chapter 3. The SQUID measurements were done by Dr. M. Venkatesan.

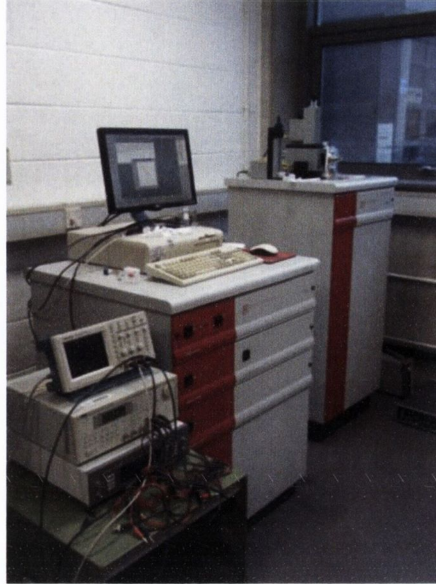

Figure 2.25. SQUID magnetometer

2.5.3 X-ray diffraction and X-ray reflectivity

X-ray diffractometer is the most commonly used method for determining the crystalline structure of materials. The typical crystalline properties of samples are obtained by using Bragg's law ($2d\sin\theta = n\lambda$) as shown in Figure 2.26. According to the Bragg's law, lattice parameter for a cubic crystalline is given by following equation.

$$a = \frac{\lambda}{2\sin\theta} \cdot \sqrt{(h^2 + k^2 + l^2)}$$

where *h, k* and *l* are the Miller indices.

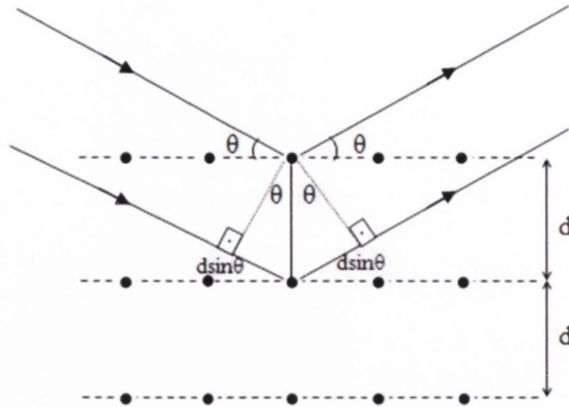

Figure 2.26. X-ray diffraction

Crystalline structure and quality of a given material can be understood from the diffraction peaks. The intensity, position and FWHM (full width at half maximum) of the diffraction peaks are used to determine that property. The FWHM is calculated by the following formula and is shown in Figure 2.27.

$$B = \frac{1}{2} \cdot (2\theta_1 - 2\theta_2)$$

where $2\theta_1$ and $2\theta_2$ represent the points at FWHM.

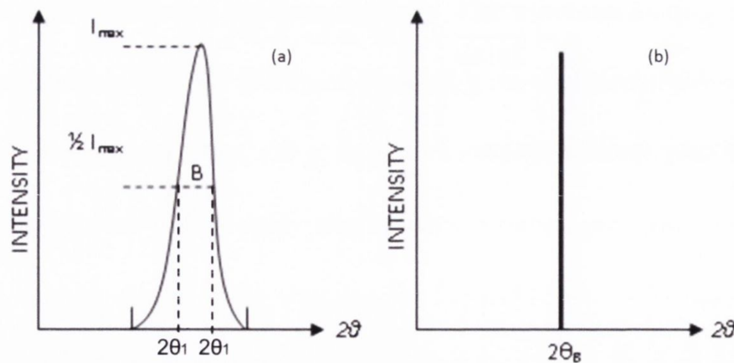

Figure 2.27. a) FWHM for a real and b) ideal XRD peak [7]

The film thickness and roughness are determined using X-ray reflectivity. This method is generally used to determine thickness, density and roughness of the thin films (single or multi layers), which is a way to calibrate the QCM. The basic idea behind this method is to send the X-ray beam to the film at low angles ($0^\circ < \theta < 10^\circ$) and measure the intensity of the reflected beam from the film surface or film/substrate interface. Both reflected beams will interfere with each other either constructively or destructively, resulting in oscillations in the reflected intensity as a function of the incident angle. The maximum positions of the oscillating intensity resulting from the constructive interference are related to the film thickness and their relation is given by the modified Bragg's law in the following expression

$$m\lambda = 2t\sqrt{\sin^2\theta - 2\delta}$$

where λ is the wavelength of the radiation used, m is the peak order, θ is the incident angle of the beam and δ is the dispersive refractive index of the sample. In this study, all XRR measurements were perform by Philips X'Pert Pro X-ray diffractometer using a Cu-K_α X-ray source (λ=0.154 nm).

Figure 2.28. Phillips X-Pert Pro system

2.5.4 Atomic Force Microscopy

Atomic force microscopy (AFM) is one of the most useful methods for observing the surface topographic images of thin films. An AFM consists of a micron-size cantilever and a silicon based tip attached to the cantilever. When the tip scans a surface, the cantilever moves up and down depending on the interaction between the tip and sample surface. Then, a laser beam is sent onto the cantilever in order to detect the deflection of the reflected beam. Next, the reflected laser beam is detected by a photodiode and topographic images are observed. In this study, a Nanoscope 3a multimode AFM device was used to study the sample surfaces and measuring the roughness of the surfaces.

Figure 2.29. Nanoscope 3a Multimode Atomic Force Microscope

2.6 Bibliography

[1] S.Y. Grachev, F.D. Tichelaar, G.C.A.M. Janssen, Journal of Applied Physics 97 (2005) 073508.

[2] J.M.D. Coey, Cambridge University Press (2010) 335.

[3] C. Fowley, Ph.D., University of Dublin & Trinity College Dublin/Ireland, 2010.

[4] K. Oguz, Ph.D., University of Dublin & Trinity College, Dublin-Ireland, 2010.

[5] J.R.S.a.B.W. Smith, Microphotography: science and technology, New York: Marcel Dekker, Inc, 1998.

[6] S.A. Campbell, The Science and Engineering of Microelectronic Fabrication. Second ed., New York: Oxford University Press, 2001.

[7] B.D.C.a.S.R. Stock, Elements of X-Ray Diffraction, New Jersey: Prentice Hall, 2001.

Chapter 3

MAGNETIC AND PHYSICAL CHARACTERISATION OF ORGANIC/METAL AND ORGANIC/INSULATOR/METAL INTERFACES

3.1 Introduction

To use the spin degree of freedom of the charge carriers for electronic applications is one ways in order to benefit from quantum mechanical effects in our daily life; it is the basis of the field of spin-electronics. Incorporating organics, molecular semiconductors or organic-based magnetic materials into this field is a new approach to producing new functional organic-based hybrid devices. These devices such as spin valves have been under investigation for the last decade. The key issue is to inject the spin polarized carriers into the organic spacer while preserving the spin orientation of the carriers, but structural and magnetic characteristics of the ferromagnetic/organic interfaces as well as the formation of interfacial states or chemical complexes at those interfaces can alter the spin properties of the carriers. All these entail a careful study of the

ferromagnetic/organic interfaces and give rise to a new field called as *spinterface* science which specifically designs the interfaces for spin-electronics applications [1].

In this chapter, we first mention some general properties of the ferromagnetic/organic interface using literature data. Then, we present magnetization measurements on a series of bilayer or capped bilayer systems composed of an organic layer (Alq_3, Znq_2 or CuPc,), a ferromagnetic layer of variable thickness (Co or CoFe) and an insulating layer (LiF or AlO_x) by using a simple method which we refer as the ferromagnetic film thickness magnetization (FFTM) method. Besides, we also present some TEM, AFM and XRR data to reveal the characteristics of the ferromagnetic/organic and ferromagnetic/oxide/organic interfaces.

3.2 Overview

Many initial reports on the organic-based spin valves show a large discrepancy between the magnetoresistance characteristics of the devices as well as widely-scattered device resistance. The sign of the magnetoresistance is one of the main discrepancies; it is reported as positive [2-5] or negative [6-9]. Xu et al. assert that observed magnetoresistance originates from direct tunneling of electrons in the locally thin areas in the organic spacers [8]. Whereas, Vinzelberg et al. concluded that magnetoresistance originates from cobalt chains embedded in the organic layer [10]. On the other hand, another interesting report published by Jiang et al. concluded that there was no magnetoresistance in the small molecule organic semiconductor Alq_3 [11]. Finally, Yoo et al. clearly pointed out that spin injection and transport in the spin electronic devices

strongly depends on the interfacial quality, imperfections in the interface resulting in significant change of device resistance and suppressed magnetoresistance [12]. Therefore, a detailed understanding of the relevant chemical and physical properties of the organic/metal interface plays a crucial role in the interpretation of transport measurements on vertical organic based spin valves.

3.3 Electronic structure of metal/organic interface

3.3.1 Metal-organic semiconductor contact

To bring two materials into contact creates new hybrid electronic states near the interface. The contact results in a charge flow across the interface and allows the materials to achieve thermodynamic equilibrium which equalizes the chemical potentials on both sides, resulting in formation of an interface dipole or band bending near the interface. The electronic energy level alignment is determined by fundamental properties of the two materials in the absence of chemical interaction on either side of the interface. Figure 3.1 shows a metal-semiconductor interface with and without contact and formation of band bending or a dipole layer at the interface. Here E_{fm} and E_f are the Fermi levels and Φ_m and Φ_{org} are the two work functions in the metal and semiconductor, respectively, and Δ is the dipole. Formation of a dipole layer at the interface is linked to several factors such as chemical reactions, ion formation or mirror forces. So far using photoelectron spectroscopy, a significant shift of approximately 1eV in the vacuum level has been observed for the metal-organic semiconductor junctions [13,14].

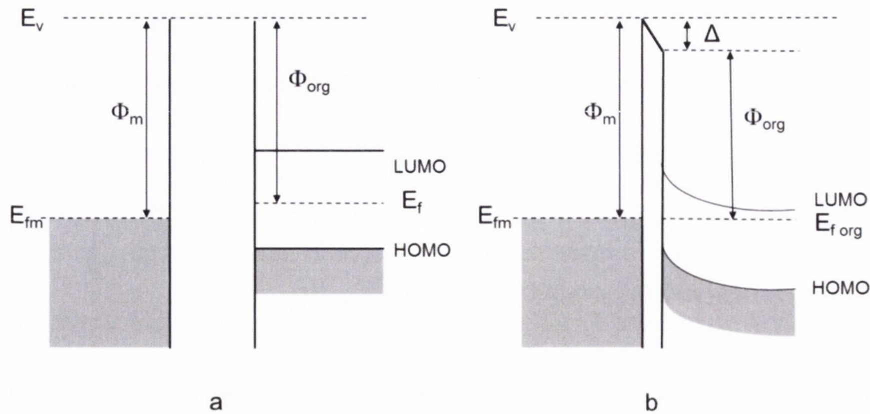

Figure 3.1. Formation of a metal-semiconductor interface and energy level alignments in separate (a) and contact (b) positions.

3.3.2 Metal-insulator-organic semiconductor contact

Introducing an insulating layer between an organic and a metal layer in the organic spin valves provides many great advantages in terms of the interfacial quality as well as the device performance. For example, studies in the last two decades have showed that the presence of a thin LiF layer sandwiched between metal and organic films in an electroluminescent device (EL) reduces significantly the driving voltage of the EL devices used in the OLED industry [15]. The fact that the LiF insulating layer improves carrier injection into the organic layer by reducing the barrier height at the interface, is a great advantage for organic-based electronic devices. Therefore, a picture of the electronic energy levels at the interface in the presence of LiF can help to better understand the transport behaviour or interface characteristics of this kind of device. A clear picture of the energy level alignment near the interface was reported by Mori *et al.* [16]. Using an ultraviolet photoelectron spectroscopy they measured the electronic structure of Alq_3/LiF/Al and Alq_3/Al. They observed that HOMO level of the Alq_3

shifts towards higher binding energy and also that vacuum level of the Alq_3/LiF/Al is much higher than that of Alq_3/Al interface. These results clearly demonstrate that LiF layer reduces the barrier height for carrier injection at the interface. Figure 3.2 shows the typical electronic structure of the Alq_3/Al and Alq_3/LiF/Al interfaces taken from ref. [16].

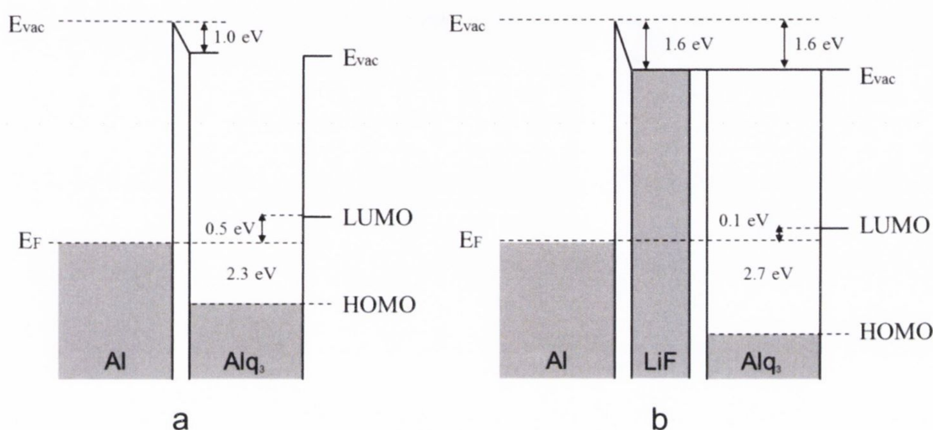

Figure 3.2. Energy levels alignment of Al/Alq_3 interface (a) and Al/LiF/Alq_3 interface.

3.4 Carrier injection mechanism into an organic semiconductor from a metal

Modifying the electrical properties of a semiconductor by doping it with a dopant in a low concentration is an easy process, resulting in a shift of the Fermi level. However, in an organic semiconductor, charge carriers must exceed a large intrinsic band gap (~ 2-3 eV) between the highest occupied molecular orbital (HOMO) and lowest unoccupied molecular orbital (LUMO), which makes difficult to excite an electron to the LUMO.

Therefore, it is a challenge to inject the charge carriers into an organic semiconductor which has no free charge and the conduction characteristics are dominated by the injection properties or the injected carriers. Mainly there are three types of injection mechanism which are known to be responsible for the injection process, field emission, thermionic emission and back-flow scattering. These injection mechanisms are explained briefly in the fallowing subsections considering a triangular barrier between metal and semiconductor (Figure 3.3)

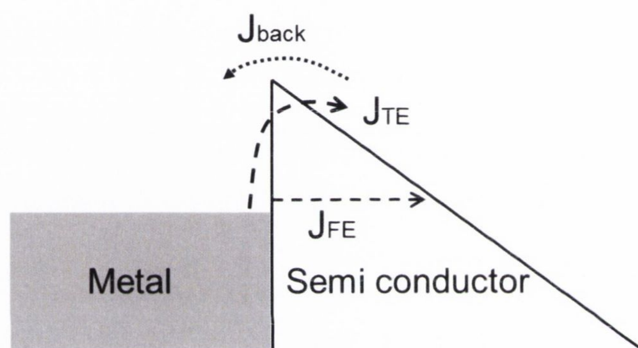

Figure 3.3. Illustrating different injection mechanism for the metal-semiconductor interface where J_{TE}, J_{EF} and J_{back} represent the thermionic emission, field emission and back scattering, respectively.

3.4.1 Thermionic emission mechanism

The thermionic emission can be considered as a heat induced charge flow over a potential barrier, ignoring the quantum mechanical tunneling, it is described as by the Richardson-Shottky model [17]. In this model, the charge carriers gain a sufficient thermal energy to exceed the potential barrier and join the semiconductor. This mechanism is illustrated in Figure 3.3 and it can be formulized as follows,

$$J_{TE} = A^{*}T^{2}exp\left[-\left(\varphi_{B} - \sqrt{\frac{qF}{4\pi\varepsilon}}\right)/k_{B}T\right] \quad (1)$$

Here A^{*} is the modified Richardson constant, φ_B is the zero-field injection barrier, q is the electronic charge, F is the external electric field, ε is the permittivity of the semiconductor, k_B is Boltzman's constant and T is the temperature. From the equation it is clear that the thermionic emission current density (J_{TE}) is decreases as the temperature is lowered. In the organic-based devices, the thermionic emission at the interface together with the phonon assisted hopping to the HOMO/LUMO energy levels introduces strong T-dependency of the device current reflecting thermal activation. For low temperatures, the current density is dominated by the field emission mechanism at the interface.

3.4.2 Field emission mechanism

The field emission mechanism known as "Fowler-Nordheim tunneling" is a quantum mechanical tunneling process of the charge carrier through a trapezoidal potential barrier at low temperature and high electric field. This process ignores the coulombic effects and only considers the tunneling through a triangular barrier represented as J_{FE} in Figure 3.3. This model is formulized in the following expression

$$J_{FE} = \left(\frac{A^{*}q^{2}F^{2}}{\varphi_{B}\alpha^{2}k_{B}^{2}}\right)exp\left[-\left(\frac{2\alpha\varphi_{B}^{\frac{3}{2}}}{3qF}\right)\right] \quad (2)$$

Here α is $4\pi(2m^*)^{0.5}/h$ and the other parameters have the same meaning as in the previous section. The main feature of this equation is that the current density (J_{FE}) is independent of the temperature and it is exponentially depends on the 3/2 power of the barrier height.

3.4.3 Back-flow tunneling

The first two models work perfectly for crystalline inorganic semiconductors but they are not expected to work perfectly for the organic semiconductors due to disorder. In a disordered system the mobility of the charge carriers is lower than in ordered systems. There is lower mean free path, which is defined by the intermolecular distance in the organic semiconductor. Furthermore, the existence of disorder in organic semiconductor systems leads to an additional obstacle which needs to be overcome by the injected carriers. When the injected carriers move away from the contact into the bulk, they come across some random energy barriers as a result of the disorder. These lead to an enhanced back-flow of injected carriers in the metal electrode represented as J_{back} in Figure 3.3, leading to decrease the field emission and the thermionic emission current [18,19].

3.5 Spectroscopic and physical characterization of metal/organic interface

Interfacial quality is a central issue in order to interpret the transport behaviour in electronic devices. The interface formed between metal and organic layers has been studied using photoemission spectroscopy and the results have shown a reacted interface as well as penetration of metal atoms into the organic layer. Recently, a careful spectroscopic study of the interface formed between metal (cobalt) and organic (Alq_3) layers has been studied by Xu *et al.* to characterize the electronic and magnetic nature of the interface using X-ray photoelectron spectroscopy (XPS), ultraviolet photoelectron spectroscopy and X-ray magnetic circular dichroism (XMCD), which is a difference spectrum of two X-ray absorption spectra (XAS) taken in a magnetic field, one taken with left circularly polarized light, and one with right circularly polarized light [20].

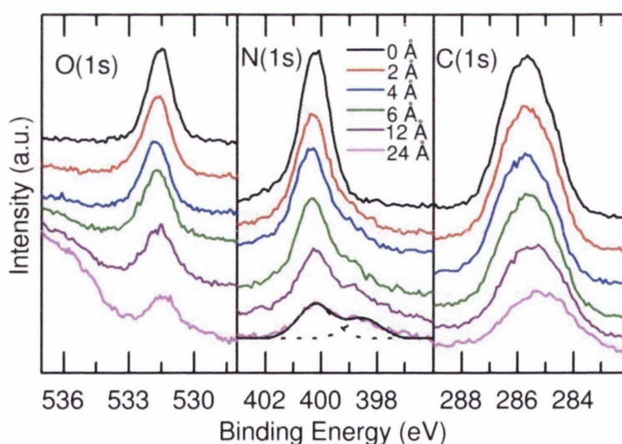

Figure 3.4. Comparison of the XPS spectra of the Alq_3 core levels before and after deposition of Co layers with different thicknesses [20].

As it is seen in Figure 3.4, the deposition of a Co layer results in formation of a shoulder on the N (1s) pristine peak on the lower binding energy side at 398.5 eV. Furthermore, the N (1s) peak decreases and the peak at 398.5 eV increases with increasing Co thickness. Beside this, there is formation of a broad shoulder on the lower binding energy side of the C (1s) pristine peak as well as a shift of the O (1s) peak with increasing Co thickness. They also reported that there is no shift in the Al (2p) core level binding energy and a completely attenuated core level signals of the Alq_3 for 5 nm thick Co deposition on the organic layer. These results support the view that there is a chemical reaction at the Co/Alq_3 interface and a limited diffusion of Co atoms into the organic layer.

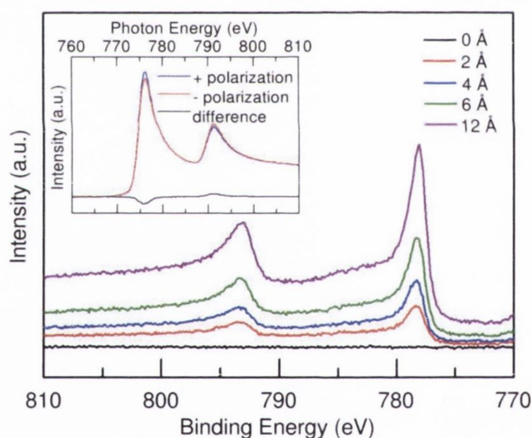

Figure 3.5. Showing the XPS spectra of Co ($2p_{3/2}$) core levels of the Co layers of various thicknesses deposited on Alq_3 [20].

The binding energy for metallic Co is known at 778.0 eV [21] and the peak positions of the Co layers deposited on the Alq_3 for 2 Å and 12 Å thick are 778.5 eV and 778.0 eV, respectively (see Figure 3.5). As the binding energy of the deposited Co layer is similar

to that of the metallic Co, an XMCD experiment is also performed [20]. The XMCD data shown at inset in Figure 3.5 were measured at room temperature for 20 Å nm Co deposited on Alq_3 and they show the signature of ferromagnetism. From the Figure 3.4 and Figure 3.5, the intensity of the Co signal increases with the increasing Co thickness while the intensity of the Alq_3 core level signals decreases. At this point, a main comment is the accumulation of Co atoms near the interface without penetrating deep into the organic layer. All these data provide an indirect measurement of the Co/Alq_3 morphology. A further analysis of the interface has been done using TEM measurement [20]. Here, the cross-sectional TEM image of a 10 nm Co layer deposited on a 30 nm thick Alq_3 film is presented (see Figure 3.6). According to the TEM picture, an abrupt interface seems to be formed with a ~ 1-2 nm roughness (considering the molecular size of Alq_3 is 1 nm in diameter) and there is no evidence for intermixing or cluster formation. However, one must take into account that the TEM image does not perfectly reflect the atomic penetration or forming an atomic conduction chain in the organic layer. Furthermore, Santos *et* al. published a TEM image which shows the Co/Alq_3/NiFe interfaces [2] and the morphology of the Co/Alq_3 is the same with the ref. [20].

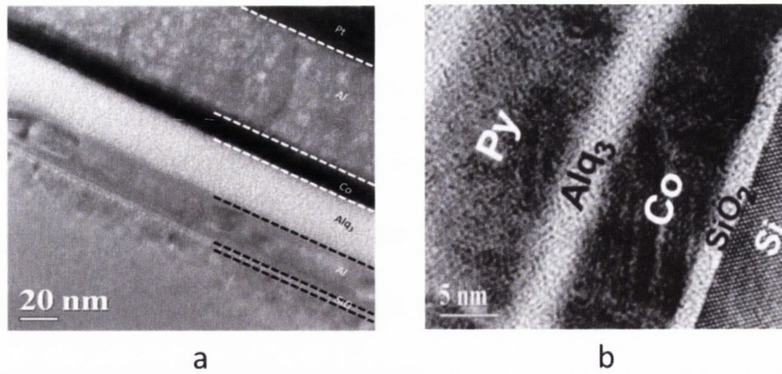

Figure 3.6. TEM images showing the metal/organic interface (a) taken from ref. [20] and (b) taken from ref. [2]

Vinzelberg *et al.* showed that penetration of the Co atoms into the organic layer is much higher than a few nanometres even more that 50 nm [10]. In their study, they made a LSMO/Alq_3/Co spin valve to study the magnetotransport using various organic thicknesses (0-200 nm) with a 1x2 mm^2 junction size, but the inconsistent results pushed them to characterize the interfaces. In their transport measurements, there are three prominent points. Firstly, in the case of $Alq_3 > 200$ nm, strong temperature dependence of the device resistances as well as non-linear feature of the I-V curves reflects the characteristics of Alq_3 layer. Secondly, in the case of $Alq_3 < 100$ nm, the devices show low resistance (short circuits) with no magnetoresistance. Lastly, they observed the spin valve effect at low temperature only when the thickness of the organic layer is 150 nm. However, the device resistances vary by $\sim 10^6$ from sample to sample prepared under the same conditions. Also they observed that sign of the magnetoresistance and switching fields are different for the same sample. Moreover, the electrical properties of the devices changes when the measurements repeated both at room and low temperatures. These inconsistent results are ascribed to the different amount of penetration of Co atoms into the Alq_3 layer. The TEM image in Figure 3.7

shows a smooth interface with no any peculiarities for the roughness or intermixing. However, their EELS measurement shows a completely different feature for the Co/Alq_3 interface. From Figure 3.7, the intensity of Co still exists in the Alq_3 side over ~ 50 nm deep inside although there is a sharp decrease in the Au side. This result indicates that Co atoms can penetrate a few tens of nanometre into the organic layer and possibly create a Co chain. This Co chain can change the transport mechanism and magnetoresistive effect such a way that it reduces the effective barrier thickness and provides tunneling contacts. Furthermore, the magnetic switching behaviour may be determined by micro magnetic Co grains which show different magnetic properties from the bulk Co.

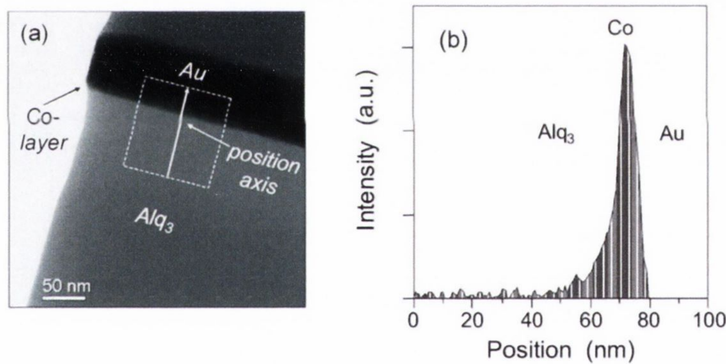

Figure 3.7. Showing the interface feature of the Alq_3/Co/Au structure (a) TEM image, (b) EELS image [10].

3.6 Magnetic and physical properties of organic-ferromagnet and organic-insulator-ferromagnet interfaces

Existence of a buried interface, especially when the metal layer is deposited on the organic layers, is a well-known interfacial imperfection that can result in modification of the transport characteristics of the devices. The buried interfaces are not easy to characterize. High resolution transmission electron microscopy (TEM) with atom-scale chemical analysis provided by electron energy-loss spectroscopy is usually the technique of choice, but it does not capture the magnetic character of the interface. Although the TEM images suggest that a rather abrupt interface is formed when ferromagnetic metals are deposited onto Alq_3 films [2,20] with roughness on a 1–2 nm length scale, the other evidence suggests Co penetration up to 50 nm in regions of Alq_3 [10]. X-ray spectroscopy suggests a 1 nm reaction layer, and ferromagnetic metallic cobalt at 2 nm and beyond [20]. Next, using the FFTM method, we present magnetization measurements on a series of bilayer or capped bilayer systems including organic, insulator and ferromagnetic thin films in order to realize the magnetic nature of that interfaces. Additionally, we will show some AFM and TEM images to support the magnetisation data.

3.6.1 Ferromagnetic film thickness magnetisation method (FFTM)

The principle of the method is illustrated in Figure 3.8. A series of bilayer films is prepared on a substrate. The nominal ferromagnetic layer thickness t is varied, and the film magnetic moment m is plotted against t. The slope for bulk cobalt, for example, corresponding to the room-temperature cobalt magnetization is $M = 1.44\ MAm^{-1}$. This is the slope expected for large cobalt thicknesses, but deviations will appear at thicknesses comparable to the interface roughness or interdiffusion layer width, as shown in Figure 3.8b. At a very rough interface, detached islands of ferromagnetic metal may be surrounded by organic material. These may be superparamagnetic at room temperature, but will block with approximately the full cobalt magnetization at low temperature. It has been established that the magnetization of cobalt retains practically its bulk value up to the surface layer [22].The intercept t_x and the shape of the curve at smaller thickness provides information on the ferromagnetically active interface between the metal and the organic. It must be recognized that the interface is formed of discrete atoms so there are bound to be deviations from the high-thickness slope below 1 nm. Furthermore, interfaces are rarely ideally sharp. Roughly speaking, t_x is the magnetic "dead layer" thickness. Thinner films may have a magnetic moment, but it is reduced from the bulk value by roughness, interdiffusion, and/or chemical reaction.

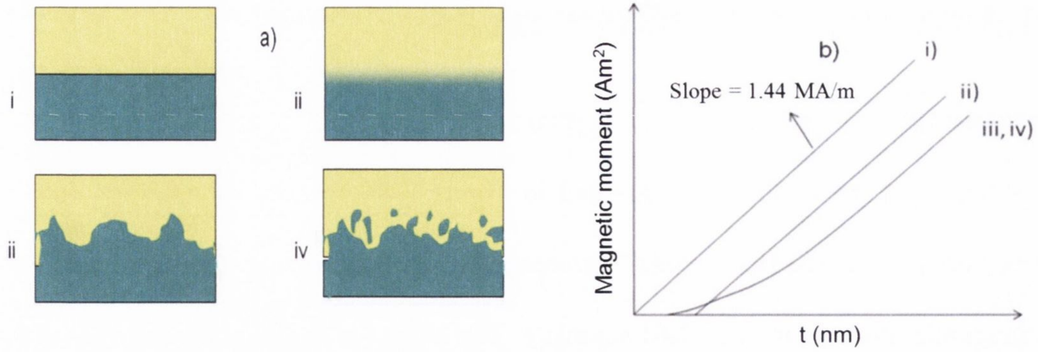

Figure 3.8. a) Schematic illustration of different magnetic interfaces: (i) sharp, atomically flat interface, (ii) diffuse interface with a reached interlayer where the metal is no longer all ferromagnetic, (iii) a rough but sharp interface, and (iv) very rough but sharp interface. b) The magnetic moment is plotted as a function of the nominal thickness of ferromagnetic metal, t.

3.6.2 SiO_2/Alq_3-Co interface

An awkward feature of thin films is that they have two sides. We have to know how one side behaves in order to deduce something about the other. A judicious choice of substrate and capping layer in a series of different stacks is required to exploit the FFTM method. Here we discuss the Alq_3-Co interface. Alq_3 is a popular tunnel barrier or transport layer in organic spin-valve structures. All the thin film structures were prepared without breaking vacuum in a chamber with a base pressure of $5x10^{-8}$ Torr. Cobalt was deposited on a Si/SiO_2 substrate or Alq_3 films by using an electron-beam evaporation technique. The source–substrate distance was approximately 25 cm mm. The Alq_3 and Al cap layers were deposited by thermal evaporation. Film thicknesses were monitored using a quartz crystal monitor during deposition. All magnetization measurements were made in a 5 T SQUID magnetometer. Initially, we investigated a cobalt layer deposited on Si/SiO_2 wafers that were subsequently exposed to air. The

cobalt is known to form a monolayer of a Co–O–Si phase at the interface [23] and the upper surface is oxidized on exposure to air to yield a 2–3 nm passivation layer of CoO [24]. Since CoO is an antiferromagnet, with a Néel temperature of 291 K, it makes no contribution to the ferromagnetic moment. Fitting the data in Figure 3.10, to a line with slope 1.44 MAm^{-1} gives a thickness t_x=3 nm, which may be identified with the thickness of the CoO passivation layer at the surface, provided the SiO_2/Co interface is flat and sharp. The effect of adding a 3.5 nm Al cap layer is shown in Figure 3.9b. It reduces t_x to 0.5 nm, which reflects the combined magnetic roughness of the top and bottom interfaces.

Figure 3.9. The stacks used for magnetic dead layer investigation showing uncapped (a) and capped (b) Co layer.

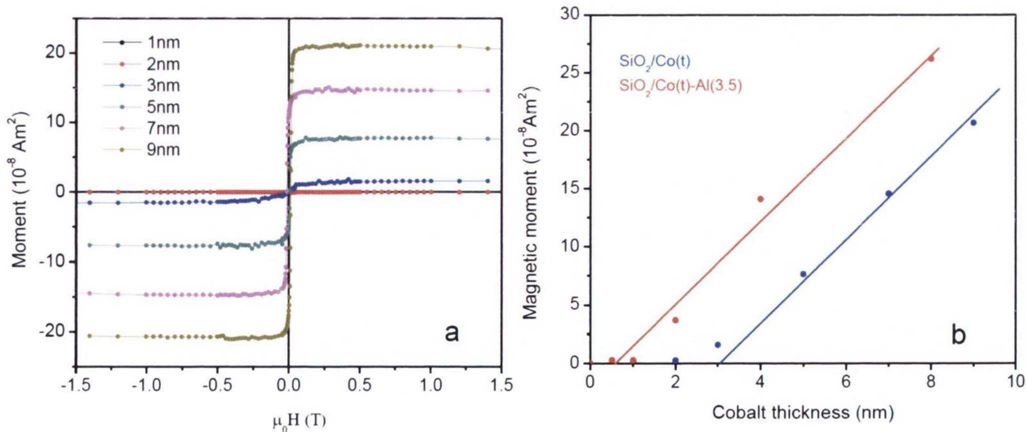

Figure 3.10. Room temperature magnetization curves for cobalt layers of different nominal thicknesses on SiO_2 (a) and FFTM plot of the data, showing the effect of introducing a 3.5 nm Al capping layer (b).

Turning now to the Co/Alq_3 interface, the cobalt layer can be either above, or below the Alq_3. When it is on top, it is necessary to use a cap layer in order to prevent the formation of CoO. The plot for Alq_3/Co/Al stacks is shown in Figure 3.11a. The value of t_x is small, 1.0 nm, indicating that the cobalt–organic interface is quite well defined when the cobalt is on top, with possible formation of a metal-organic complex [18]. If the Al cap layer is omitted, the value of t_x rises to 3.4 nm, which represents the sum of the CoO passivation layer thickness and the Alq_3/Co interface. The rms roughness of the 40 or 10 nm Alq_3 layer is 0.19 or 0.32 nm, respectively, much less than the dead layer thickness.

The situation seems to be different when Alq_3 is deposited on cobalt. Then the value of t_x is 3.3 nm, which suggests an extremely diffuse or oxidized interface. This would appear to justify the practice of incorporating a thin protective layer of AlO_x or MgO at the surface of the bottom Co electrode in an organic spin-valve stack. However, a surprising result was found when an Al cap layer was deposited on the Alq_3 layer covering the Co. The value of t_x then fell to just 1.2 nm. It seems that the cobalt at the Co/Alq_3 interface is oxidizing through the Alq_3, and that it is not intrinsically very rough. Since fairly large magnetoresistance values are achieved at room temperature for stacks that have a direct Alq_3/Co top interface, it seems likely that similar results may be possible with a direct Co/Alq_3 bottom interface as well, at least insofar as the organic acts as a tunnel barrier.

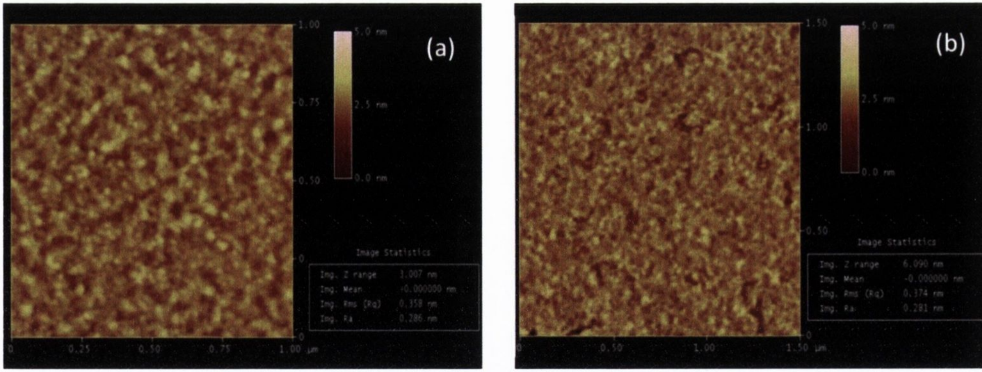

Figure 3.11. FFTM plots of the Alq_3/Co interface showing the effect of the Al capping layer (a) and the bilayer with Alq_3 on top (b).

In Al-capped Co on Alq_3, t_x was reduced from 0.6 nm at room temperature to 0.3 nm at 4 K. The disconnected regions of cobalt metal shown in Figure 3.8a (iv) are blocked, increasing the ferromagnetic volume and decreasing its roughness. Almost all of the FFTM plots show a nonzero Co moment at thicknesses that are just less than t_x. This shows clearly that t_x is an upper limit on the thickness of the magnetic dead layer. For example, the data in Figure 3.11a show a moment m = 1.07×10^{-8} Am^2 for a thickness of 1 nm. This would be consistent with a corrugation of the Co/Alq_3 interface in which half of the area at this depth is composed of cobalt atoms that are connected to the bulk of the film. Such a corrugated surface may help to promote spin injection into the organic, whereas an interface where paramagnetic cobalt is dissolved in the organic is likely to destroy the spin polarization of injected electrons by spin-flip scattering.

3.6.3 SiO_2/Alq_3-LiF-Co interface

3.6.3.1 The effect of LiF layer on the structural evolution of Alq_3/Co interface

In this section, we investigated the effect of introducing a thin interlayer of LiF between the Co and Alq_3. The LiF was chosen as the tunnel barrier because it has been widely used in the OLED industry and it is expected to promote injection of electrons into the band derived from the lowest unoccupied molecular orbital (LUMO) of Alq_3 [15]. Furthermore, it has been shown that LiF does not dissociate during the evaporation process [16]. We started to investigate the role of LiF at the interface by performing the atomic force microscopy (AFM). To measure the roughness of the organic layer with and without LiF, we evaporated two sets of 20 nm Alq_3 on 5x5 mm^2 SiO_2 substrates and one of them was capped by 2 nm LiF layer. Figure 3.12a and Figure 3.12b show the surface roughness of the Alq_3 (20 nm) and Alq_3 (20nm)/LiF (2 nm) layers deposited on SiO_2, respectively. The RMS roughness of the Alq_3 single layer is 0.35 nm and depositing 2 nm LiF slightly increases the RMS roughness to 0.37 nm. This low roughness is one of the necessary requirements for the good quality interfaces in the organic spin valve devices, especially reducing the Néel orange peel coupling [25].

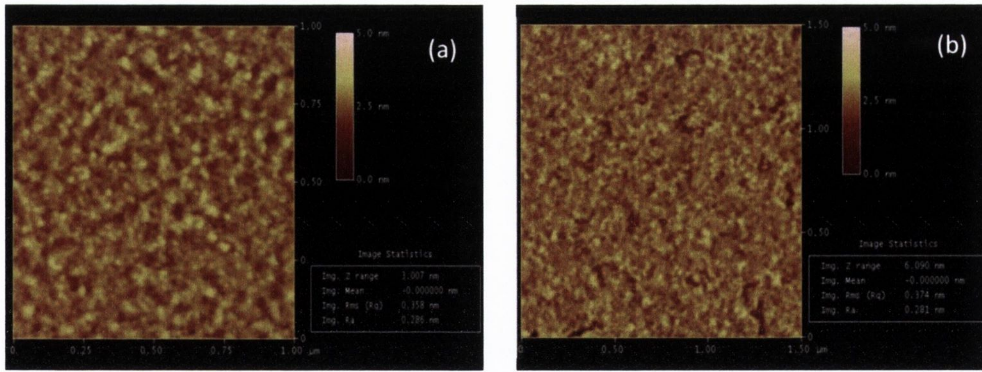

Figure 3.12. AFM image of SiO_2/Alq_3 (20 nm) (a) and SiO_2/Alq_3(20 nm) LiF (2 nm) (b)

As a next step we look at the interfaces of a Alq_3/LiF/Co tri-layer to see the interface morphology. Figure 3.13a and Figure 3.13b show the transmission electron microscopy (TEM) images of the Alq_3(40 nm)/LiF(2 nm)/Co(5 nm)/Al(7 nm) structure in normal and high resolution modes. In Figure 3.13a, the ultra-thin LiF between the Alq_3 and Co layers, can be clearly distinguished as a bright thin layer on the organic. We expect that LiF prevents the formation of a mixed interface between the Alq_3 and Co and it blocks the diffusion of the Co atoms into the organic layer. In Figure 3.13b, we look at the interfaces in a high resolution TEM picture in the bright field mode; the electron-dense regions are dark. It is not easy to distinguish the LiF layer in this picture due to the measurement mode but we can clearly see the effect of that layer in the circularly marked regions that show well-ordered Co atoms. It is obvious that LiF also improves the structural quality of the Co layer and it appears to induce crystallization of the Co.

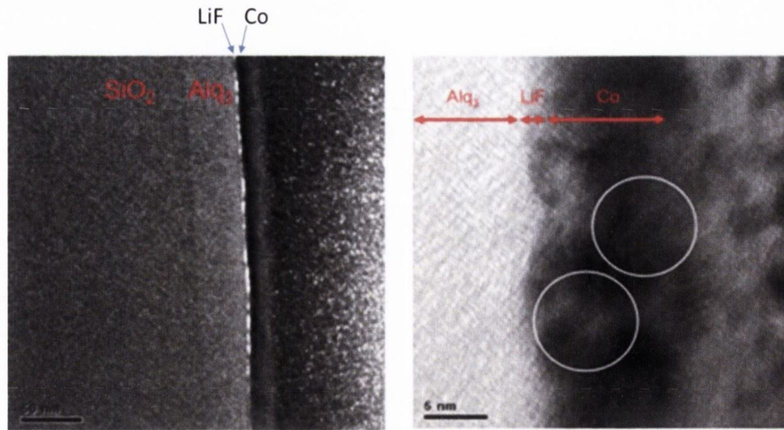

Figure 3.13. TEM image of SiO_2/ Alq_3(40nm)/LiF(2nm)/Co(5nm)/Al(7) multilayer in normal dark field mode (a) and high resolution mode (b).

It is also worthwhile to check the Alq_3/LiF/Co interfaces using small-angle X-ray reflectivity method (XRR) on the same stack. Figure 3.14 shows the XRR oscillations (black line) and also the fit (red line). It is not easy to obtain fits when the number of layers is bigger than 2-3 but we tried to fit the data to get some idea about the interface roughness of the Alq_3 stack. According to our best fit, the calculated layer thicknesses and their interface roughnesses are summarized in the table inserted in Figure 3.14. All the layer thicknesses are quite consistent with the thicknesses measured by quartz crystal microbalance (QCM) during the deposition process. The roughness at the Alq_3/LiF interface is found to be 0.95 nm. If we consider the thickness of the Alq_3 film, 40 nm, and its molecular size (around 1 nm), with this roughness is reasonable to call the interface abrupt. The same roughness value is also measured at the LiF/Co interface, 0.93 nm, and the LiF/Co interface apparently follows the Alq_3/LiF interface.

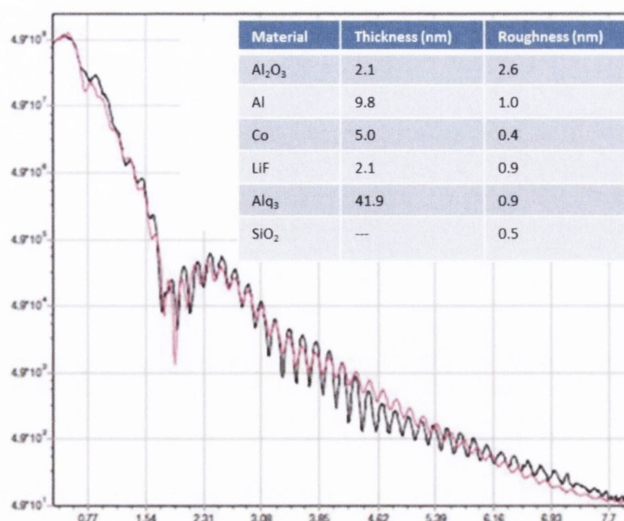

Material	Thickness (nm)	Roughness (nm)
Al_2O_3	2.1	2.6
Al	9.8	1.0
Co	5.0	0.4
LiF	2.1	0.9
Alq_3	41.9	0.9
SiO_2	---	0.5

Figure 3.14. The XRR reflectivity of the SiO_2/Alq_3(40)/LiF(2)/Co(5)/Al(7) stack. The black line is the experimental data and the red line is the fit.

3.6.3.2 The effect of LiF layer on the magnetic evolution of Alq_3/Co interface

In this section, the Alq_3/LiF/Co interface will be investigated in terms of its magnetic characteristics. One of the well-known thin film properties of LiF is that the initial growth of this material occurs via island formation followed by a layer-by-layer growth [26,27]. Therefore, it can be worthwhile to vary the thickness of the LiF layer inserted between the Alq_3 and Co layers to see the variation of the magnetic properties of the Co layer. A multilayer stack with varied LiF thicknesses was deposited on a SiO_2 substrate of size 5x5 mm^2 and the magnetic moment and the full hysteresis curves of the samples was measured in the 5 Tesla SQUID magnetometer at 300 K or 4 K. The multilayer stack in question is SiO_2/Alq_3(20)/LiF(t)/Co(4)/Al(4) (the numbers always represent the layer thicknesses in nanometre and *t* is the varied thickness of the LiF layer). Figure 3.15 shows the effect of LiF thickness on the magnetic moment of Co thin films.

Introducing the LiF layer between the organic and Co layers apparently improves the magnetic moment even for thickness of the LiF layer as low as 0.5 nm. The magnetic moment increases with increasing LiF thickness thanks to the formation of a good uniform underlayer film. We can deduce from this data that LiF blocks the reaction of Co with Alq_3, which leads to an increased magnetic moment.

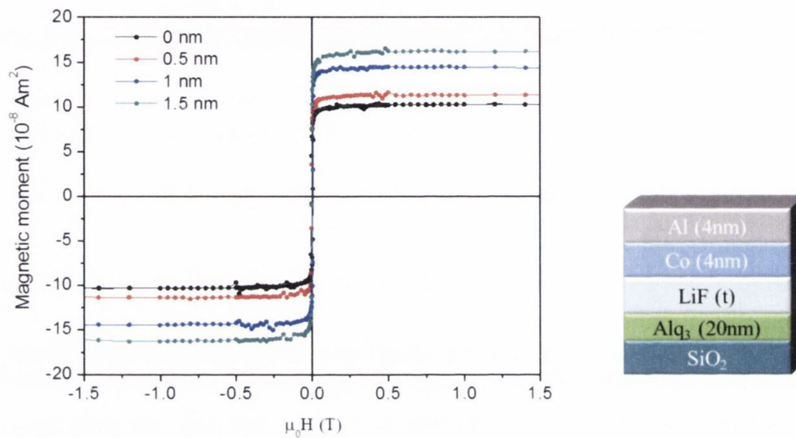

Figure 3.15. Magnetisation curves of Co layer with varying LiF thickness and corresponding multi-layer.

As a next step, the thickness of the LiF layer was fixed at 1 nm and the Co layer was evaporated with varied thicknesses in order to compare the formation of dead layer in the presence and absence of LiF buffer layer. Figure 3.16 shows the effect of LiF on the evolution of the magnetic dead layer at the interface. From the intercept points we determine the thickness of the dead layers as 0.24 nm and 0.93 nm with and without LiF at 300 K, respectively. This values decreases to 0.13 nm and 0.63 nm with and without LiF at 4 K, respectively. It is clearly seen that LiF is also reducing the formation of the magnetic dead layer at the interface. Furthermore, comparison of the magnetisation switching curves with and without LiF buffer layer at 4 K clearly show

that magnetisation of Co switches more sharply when LiF is introduced at the interface (see Figure 3.17).

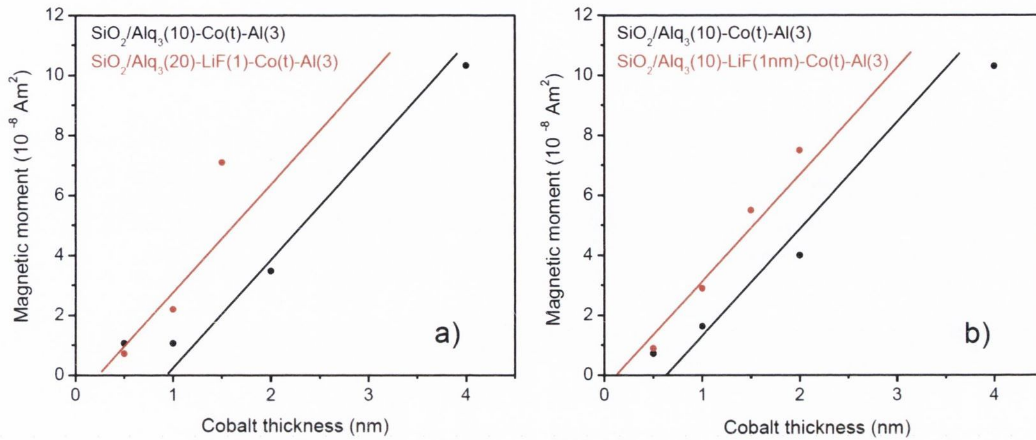

Figure 3.16. FFTM plots of the Alq_3/Co interface showing the effect of the LiF buffer layer a) at 300 K and b) at 4 K

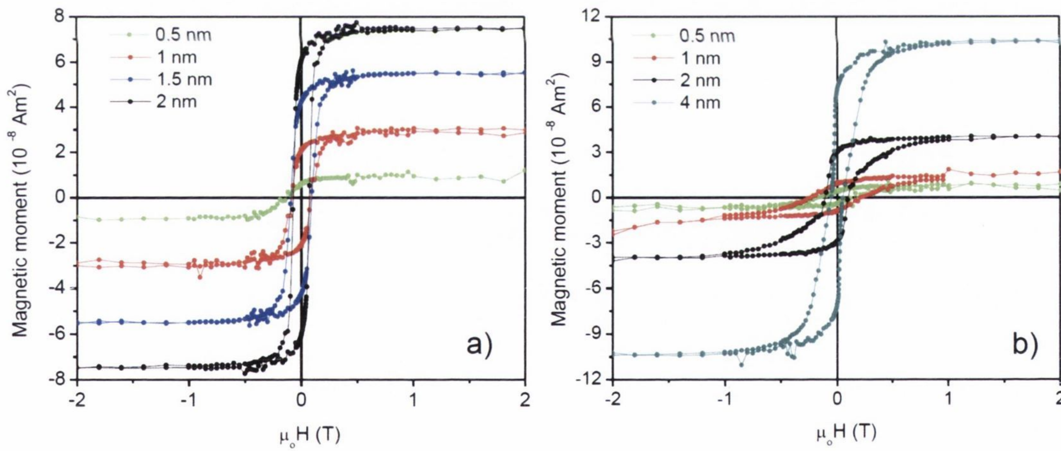

Figure 3.17. Magnetisation switching curves of Co layers at 4 K showing the effect of the LiF buffer layer a) with LiF and b) without LiF.

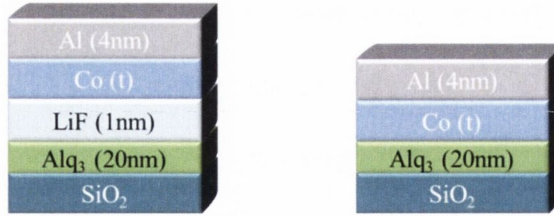

Figure 3.18. Related multi-layer stacks for Figure 3.17, showing the Co layer deposited either on LiF or Alq_3.

Chemical characterization of the ferromagnet/organic interface and the role of an insulating layer on the evolution of an unreacted interface has been deeply studied by Borgatti et al. [28]. Figure 3.19 shows the hard X-ray photoelectron spectroscopy of the bare Alq_3, Co/Alq_3 and Co/AlO_x/Alq_3 structures. The N 1s and C 1s spectrums show that there is a broadening in the lower binding energy side in the absence of AlO_x layer at the Co/Alq_3 interface (top panel). The broadening for the N 1s peak is larger than the C 1s peak. However, the peaks are nearly identical for the bare Alq_3 and Alq_3/AlO_x/Co structures. The bottom panel of Figure 3.19 shows the spectral fit for the Co/Alq_3 interface. There are three components for the N 1 s spectra at 399.0 eV, 400.4 eV and 402.3 eV. The presence of the peak at 399.0 eV for the Co/Alq_3 structure indicates some degree of chemical interaction while that peak is very weak for the other samples. Furthermore, the shift of the peaks at lower binding energies indicates an increase in the local electronic charge in the Alq_3 molecule, which is more visible in the N 1s peak.

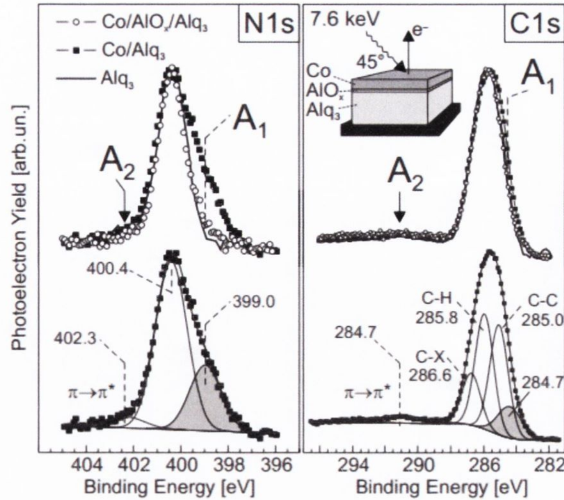

Figure 3.19. Herd X-ray photoelectron spectroscopy of bare Alq3, Co/Alq3 and Co/AlO_x/Alq_3 structures.

3.6.4 The effect of an AlO_x layer at the Alq_3/CoFe interface

So far, the effect of a LiF insulating layer in between the small molecule organic semiconductor Alq_3 and a ferromagnetic Co layer has been investigated but as it is going to be explained in the next chapter, LiF is not a good material when the spin transport is concerned. At this point it will be worthwhile to use an insulating material which allows the spin polarized transport such as AlO_x or MgO. These oxides have been studied intensively for two decades in the spin electronics field as tunnel barriers and their fantastic spin transport properties make these materials useful for future spin electronics applications [29-32]. These materials can be deposited in a thin film form using electron beam deposition or magnetron sputtering techniques using the facilities of Centre of Research on Adaptive Nanostructure and Nanodevices (CRANN). However, the challenge is to make all the oxide, metal and organic layers in the same chamber without exposing the samples to the air so that we can get a high quality interfaces. In our organic UHV chamber we can use only the thermal evaporation

technique which is not suitable for the deposition of AlO_x and MgO thanks to their very high evaporation temperatures. However, we overcome this problem oxidizing the thin film metals in a pure oxygen environment. Here, we choose AlO_x as an insulating layer which is obtained from the oxidation of thin Al metal layer and the details of the oxidation process are explained in the experimental part of the thesis (Chapter 2). We also choose the $Co_{50}Fe_{50}$ alloy as a ferromagnetic layer due to its higher spin polarization than the Co. We made a series of multi-layered stacks which comprise Alq_3, CoFe, Al and AlO_x in order to understand the effect of AlO_x insulating layer at the Alq_3/CoFe interface. All the materials are evaporated from a hot surface using thermal evaporation and the base pressure of the chamber is ~ $5x10^{-9}$ mbar. The AlO_x layer is obtained exposing the thin layer of Al to oxygen in the load-lock. Figure 3.20 summarizes the effect of AlO_x at the Alq_3/CoFe interface in terms of the magnetic properties of the CoFe layer. First of all the magnetic moment of the CoFe is higher when it is capped by AlO_x rather than Al, which indicates that CoFe/AlO_x interface is much better than the CoFe/Al interface. For the simplicity the CoFe-AlO_x structure is called as a base bilayer. The magnetic moment of this bilayer does not change when the Alq_3-AlO_x structure deposited on it, so we can infer that thin layer of 1.5 nm AlO_x prevent the reaction between CoFe and Alq_3. If we remove the AlO_x layer from top of the base stack, the magnetic moment of the CoFe sharply decreases thanks to the reaction of the CoFe atoms with Alq_3 molecules and formation of a dead layer at the CoFe-Alq_3 interface, see the green and red curves in Figure 3.20). The reason why this structure has the lowest magnetic moment with respect to the others is that the CoFe layer has another interface on the bottom side with SiO_2 and this interface also contributes the formation of a dead layer, resulting in lowest magnetic moment. So what happens if the CoFe layer evaporated on Alq_3? The blue curve shows the

magnetisation curve of the base stack when it is evaporated on the Alq_3 layer and it shows that magnetic moment increases remarkably if we compare the case that CoFe is in the bottom side (the red curve). That increment results from the different magnetic interface of the bottom side of CoFe, Alq_3-CoFe interface is better than SiO_2/CoFe interface. As a last step, introducing a thin layer of AlO_x between the bottom Alq_3 layer and the base stack shows the highest magnetic moment for the CoFe layer due to the formation of good interface in the both side of CoFe. In conclusion, the AlO_x insulating layer shows the similar effect like LiF in terms of the magnetic quality of the organic/ferromagnetic interface and it is a good candidate for the further spin transport studies in the organic based spin valves. The magnetotransport studies of the Alq_3/AlO_x hybrid barrier structure will be explained in detail in the next chapter of the thesis.

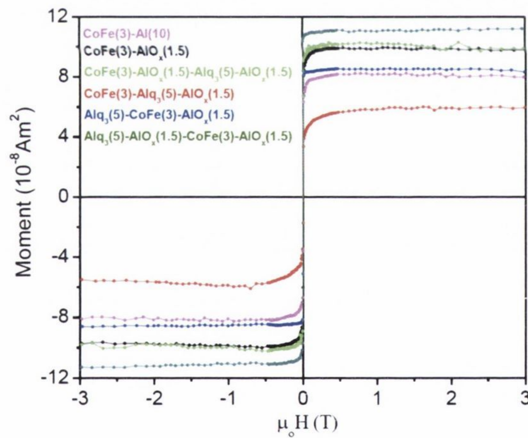

Figure 3.20. Magnetisation curves of the CoFe layer showing the effect of AlO_x at the Alq_3/CoFe interface.

3.6.5 TEM, EDX and EELS analysis of CoFe-AlO_x-Alq_3-AlO_x-CoFe structure

So far, the magnetisation data have shown us that the reacted interface between the organic and ferromagnetic layers can be controlled by inserting a thin layer of insulator. To use an organic layer in a spin valve stack as a spin channel requires two interfaces, in contact with bottom and top ferromagnetic layers. Therefore, inserting a thin layer of AlO_x on each side of organic layer will be the best option to avoid any intermixing or reaction at the organic/ferromagnet interface. It should result in enhanced carrier transmission the organic layer from both sides. To see the interfacial picture of both sides of the organic layer we produced a spin valve stack (SiO_2/CoFe[8]-AlO_x[1.5]-Alq_3[10]-AlO_x[1.5]-CoFe[18]) and summarize the data in Figure 3.21. The scale bar in the TEM cross-section is 20 nm and it shows nice continuous films, but the AlO_x layers deposited on both sides of the organic layer are relatively thin and cannot be clearly seen on this scale. However, this image does not reflect the real picture of the interfaces in terms of the atomic diffusion or intermixing. For a deeper analysis, an EDX (energy-dispersive X-ray spectroscopy) and EELS (electron energy loss spectroscopy) analysis was done on the sample and the line scan gives us the elemental composition of the scanned area. Co, Fe and Al peaks are marked as green, orange and red lines respectively and they are seen clearly in the EDX spectrum (top panel). For Co and Fe peaks the signals come from the CoFe film and they are completely top of on their each other. The gap between the two CoFe peaks is roughly 10 nm and it corresponds to the thickness of the Alq_3 layer, which is also supported by EELS data. Furthermore, from the same data Al seems to have diffused into the CoFe layer. The point scan marked as '+' in the TEM image reflects the position of the signal in the same EDX panel as well

as the elemental composition of the marked point in the left panel. It is very clear to see Co, Fe and Al peaks at the same point in the interface, showing that Al atoms have diffused into the CoFe layer. Then, for the comparison we moved the sign '+' on the line scan to the middle of the Alq_3 layer to see the elemental composition in that point (Figure 3. 22). In that case, the Fe and Co peaks sharply decreases to the background level in the left panel of the EDX spectrum, indicate the absence of a significant metal diffusion into the organic layer.

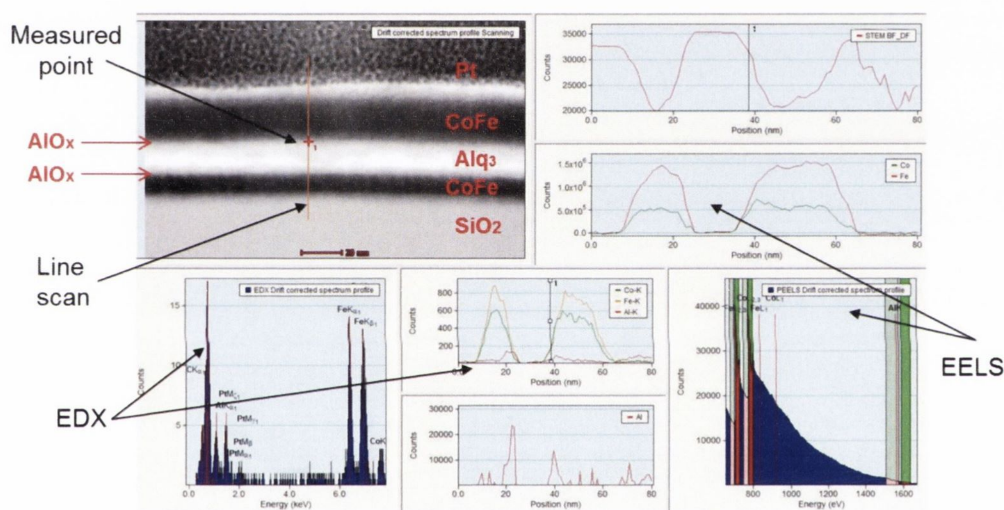

Figure 3.21. Showing the TEM, EDX and EELS data of SiO_2/CoFe(8)-AlO_x(1.5)-Alq_3(10)-AlO_x(1.5)CoFe(18) stack.

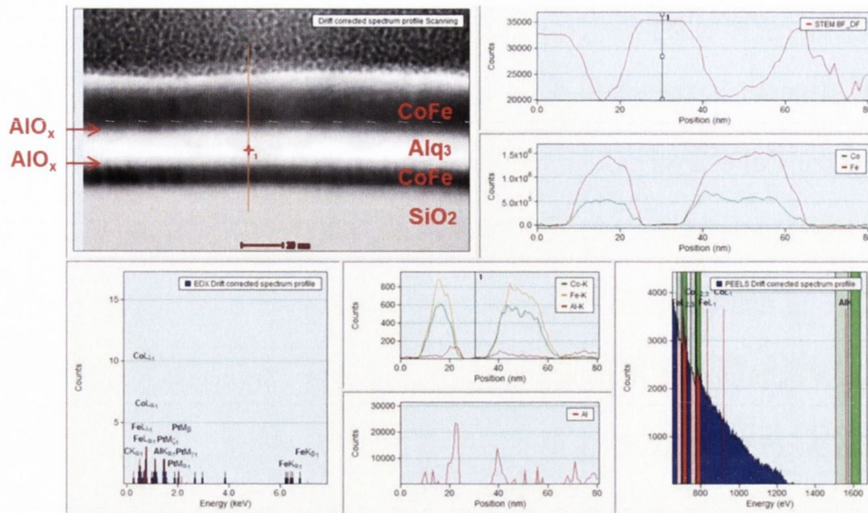

Figure 3. 22. TEM, EDX and EELS data, showing the elemental composition in the middle of the Alq_3 layer.

Also, the electron beam intensity profile gives us more information about the interface. Figure 3.23 compares the three profiles taken from different regions of the TEM lamella and it is obvious from the figure that the interface has different features for different regions, showing the non-uniform interface. From the figure we can also deduce that the top interface is much rougher than the bottom because the variation of the peak shape of the top interface is much higher than the bottom.

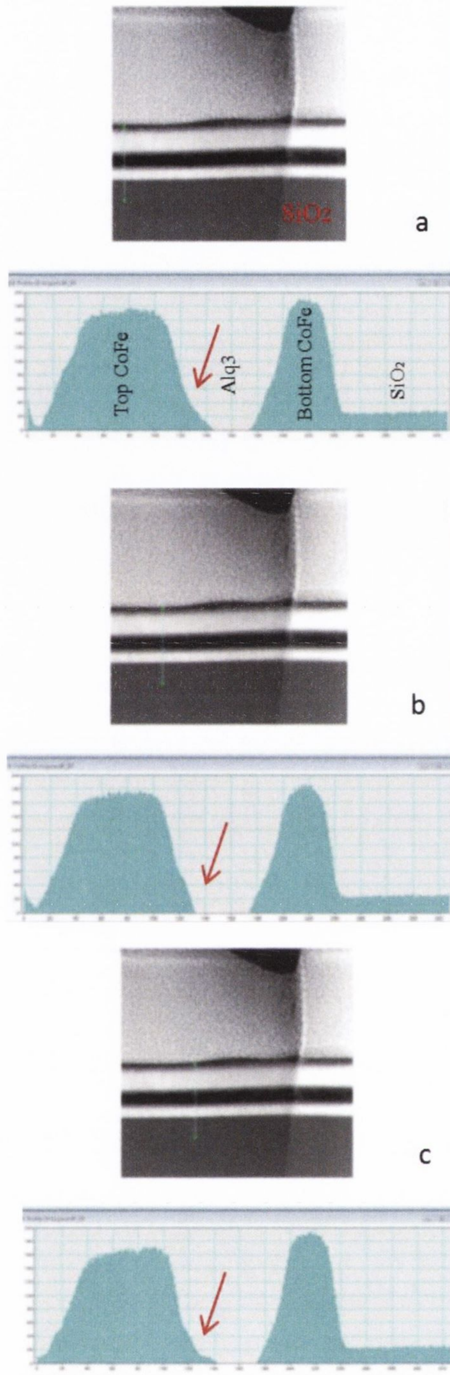

Figure 3.23. Electron intensity profiles taken from different regions of the top and bottom interfaces of SiO_2/CoFe(8)-AlO_x(1.5)-Alq_3(10)-AlO_x(1.5)CoFe(18).

3.6.6 SiO_2/Znq_2-Co interface

Bis(8-hydroxyquinoline) zinc (Znq_2) is used as an alternative organic material to Alq_3 in the OLED industry due to the high quantum yield which results in low operating voltage in the device performance [33]. To incorporate such a useful material into the field of organic spin-electronics and to study its magnetotransport properties will be an attractive research prospect. Therefore, in this part we start with the interfacial properties of Znq_2 when it contacts a ferromagnetic layer.

3.6.6.1 Magnetic features of the Znq_2-Co interface

To investigate the magnetic dead layer at the organic/Co interface we made a series of bilayer and fitted the data to a line with the slope of bulk Co. Initially, we cap the Co surface with Al or LiF layers in order to prevent the formation of CoO and also to compare the different contributions which comes from the capping layer. From the magnetisation data in Figure 3.25a, the magnetic moment of the Co layer is independent of the type of capping layer, Al and LiF are both good protection layers. The interface between Co and Znq_2 can be in the two forms, either with Co on top or at the bottom. When Co is at the bottom, the magnetic moment is lower than the case that it is on top. The reason is that when Co is deposited on the SiO_2 substrate, a Co-O-Si phase forms at the interface as was explained in the section 3.6.2. Fitting the data to the bulk magnetisation value of Co, we determine the magnetic dead layer in the both case (Figure 3.25b). The thickness of the dead layer is approximately 1.3 nm when Co is at the bottom or 1.0 nm when it is on top. The lowest magnetic dead layer in the graph

observed for the SiO_2/Co-Al bilayer (~0.6 nm). The dead layer increases from 0.6 nm to 1.0 nm when the Co-Al bilayer is deposited on Znq_2. The difference (0.4 nm) clearly indicates a small intermixing or a chemical reaction at the interface between Co and Znq_2.

Figure 3.24. The stacks showing that the Co layer is either deposited on SiO_2 or Znq_2.

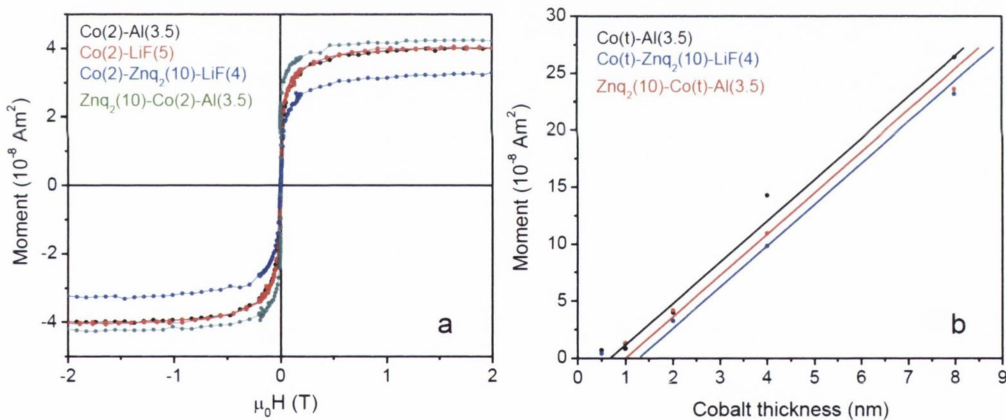

Figure 3.25. Room temperature magnetisation curves of Co layers with different under layer and top layer (a) and FFTM plot of the data, showing the related magnetic dead layers (b).

3.6.6.2 Structural analysis of Znq_2-Co interface

In addition to the magnetic feature of the Znq_2-Co interface it is also worthwhile to know how the interface looks like in terms of AFM and TEM. Znq_2 can be evaporated in a thin film form as seen from the XRR measurement with nice oscillations and 0.36 nm RMS roughness in Figure 3.26. The roughness is also confirmed by performing AFM measurements for the 10 nm thick Znq_2 thin film (0.44 nm).

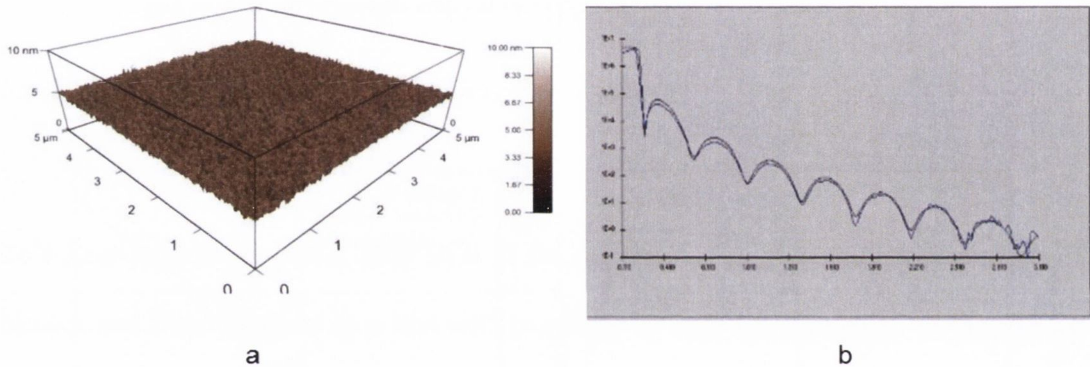

Figure 3.26. AFM (a) and XRR (b) measurements of a 10 nm thick Znq_2 film showing smooth surface.

For further analysis a TEM image as well as electron intensity profile were taken for the $SiO_2/Znq_2(10)$-Co(12)-Al(3.5) stack. It is apparent from the image that there is no substantial intermixing or cluster formation at the interface. The beautiful and sharp interface between Znq_2 and Co can be clearly seen from the picture and this is also confirmed by the electron intensity profile in Figure 3.27. However, we have to keep in mind that these kinds of measurements do not pick up any chemical reaction or single-atom diffusion at the interface. At this point, the magnetic measurements explained

above will be the more reliable way to characterize small-scale atomic diffusions or chemical reaction at the interface.

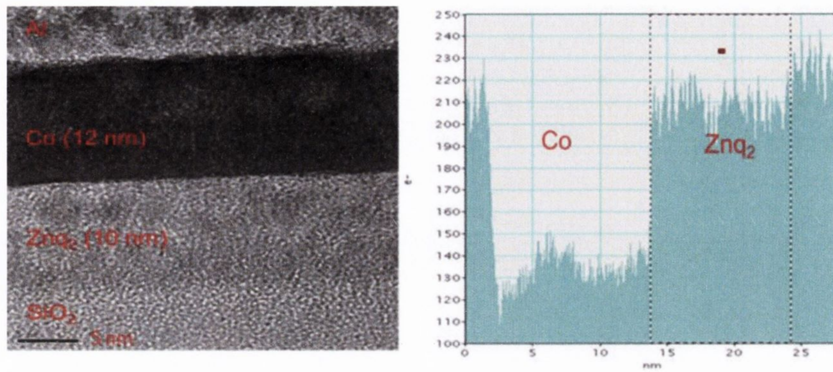

Figure 3.27. TEM and electron intensity profile showing the sharp interface between Znq_2 and Co.

3.6.7 SiO_2/CuPc-CoFe interface

Another promising family of organic compounds are the metal phthalocyanines, thanks to their very large application area such as electro-optic devices, photovoltaic cells, photoconducting agents and other photoelectronic devices [34-36]. So far, various metal- substituted phthalocyanines have been studied in many different fields. Among them Copper (II) phthalocyanine (CuPc) is a well-known p-type organic semiconductor with some of the best properties in the phthalocyanine family [37]. In this thesis we mainly focus on CuPc, studying the CuPc/ferromagnet interface and magnetotransport properties.

3.6.7.1 Magnetic properties of the CuPc-CoFe and CuPc-AlO_x-CoFe interfaces

In order to characterize the CuPc-ferromagnet and CuPc-oxide-ferromagnet interfaces, we deposit a series of multi-layered stacks consisting of CuPc, AlO_x and CoFe in different configurations. The layers were thermally evaporated under UHV conditions without breaking the vacuum and subsequently their magnetic properties were measured in the SQUID magnetometer. Initially, we investigate the effect of an AlO_x layer deposited between CuPc and CoFe, and the related magnetic measurements are summarized in Figure 3.28a and Figure 3.28b for SiO_2/CuPc(5)-CoFe(t)-AlO_x(1.5) and SiO_2/CuPc(5)-AlO_x(1.5)-CoFe(t)-AlO_x(1.5), respectively. For simplicity, both graphs are plotted in the same scale. Comparing the both graphs, the general conclusion is that the presence of the AlO_x layer at the interface results in to increase the magnetic moment of the CoFe layer. There is no a clear sign of magnetic moment up to 2 nm of CoFe in the absence of AlO_x while 0.5 nm CoFe has small magnetic moment in the case it is evaporated on an AlO_x layer. For further analysis the thickness of the CoFe layer is fixed at 3 nm and it is evaporated on SiO_2, CuPc or AlO_x and then it is capped with either CuPc or AlO_x. Magnetisation switching curves were then measured up to 2 Tesla (Figure 3.29a). The results are almost the same for Alq_3 and Znq_2. When it configured between SiO_2 and CuPc, CoFe has the lowest magnetic moment value due to the formation of reacted interface in on both sides. If the top side is isolated from CuPc using a thin layer of AlO_x, the magnetic moment doubles from $4.4x10^{-8}Am^2$ to $8.8x10^{-8}Am^2$. Furthermore, the CoFe layer has the maximum magnetic moment value when it is sandwiched between AlO_x layers ($12.2x10^{-8}Am^2$). In this case, the CoFe layer is isolated from CuPc as well as SiO_2 and formation of a phase with substrate in the bottom side and a metal-organic complex on the top side is eliminated. As a next

step, CoFe is deposited with various thicknesses either on CuPc or AlO_x keeping the same capping layer in order to investigate the magnetic dead layer. The FFTM plot in Figure 3.29b shows formation of ~1.4 nm magnetic dead layer in the absence of AlO_x layer in between CoFe and CuPc. The dead layer reduces to 0.5 nm when AlO_x is introduced at the interface. These results clearly show that CuPc also reacts with ferromagnets, as it has been previously reported based on NEXAFS [38]. A 0.5 nm magnetic dead layer is always seen for any other magnetic material and it reflects the combined magnetic roughness of the top and bottom interfaces. For example, the saturation value of magnetic moment of 3 nm CoFe is 1.22×10^{-8} Am^2 (Figure 3.29a green curve) while the calculated value is 1.42x10-8 Am^2 [39].

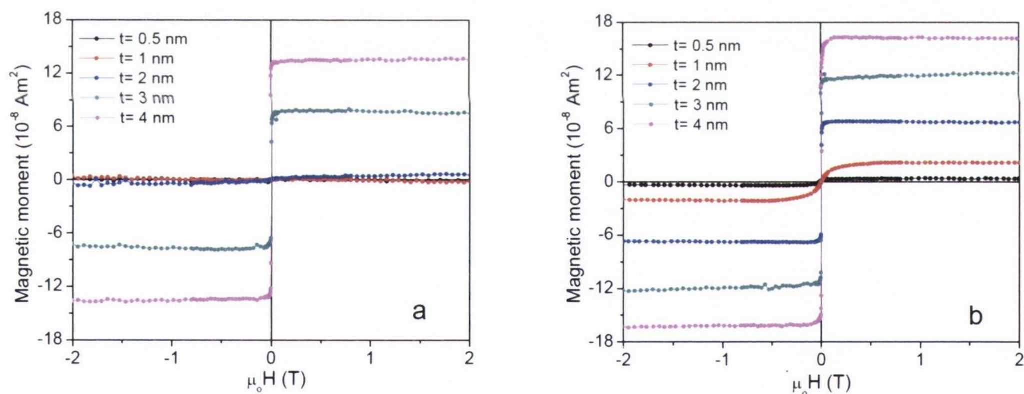

Figure 3.28. Room temperature magnetisation switching curves of SiO_2/CuPc(5)-CoFe(t)-AlO_x(1.5) (a) and SiO_2/CuPc(5)-AlO_x(1.5)-CoFe(t)-AlO_x(1.5) (b).

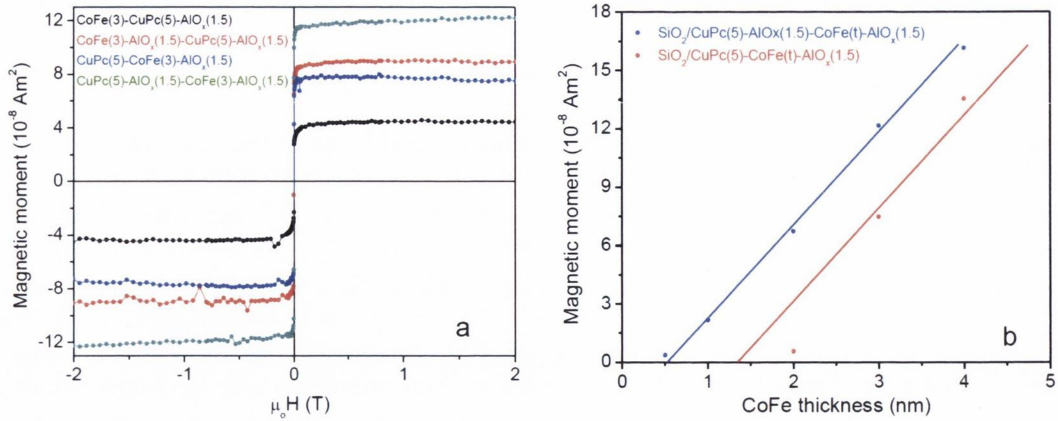

Figure 3.29. Showing the room temperature magnetisation switching curves of CoFe layer with the combination of different bottom and top layers (a) and FFTM plot showing the effect of AlO_X on the formation of the magnetic dead layer (b).

In general, magnetic moment of the ferromagnetic films exhibits linear relationship with the ferromagnetic film thickness. However, the experiments have shown that this linear response shifts slightly from the origin, indicating that the effective magnetic thickness is smaller than the actual ferromagnetic film thickness. This difference is known as magnetic dead layer. It is generally attributed that rough, mixed or chemically reactive interface are the source of magnetic dead layer. For example, in the case of intermixing, ferromagnetic atoms may be surrounded by the other non-magnetic atoms and exchange interaction between the magnetic atoms reduces. This lowers the total magnetic moment of the film. The effect of magnetic dead layer on spin transport may depend on the materials used in the spin electronic devices. The experiments have shown that the TMR in a FM/I/FM structure is inversely proportional to the magnetic dead layer thickness. It is generally accepted that the magnetic dead layer reduces the spin polarisation of the transmitted electrons and acts as a spin flip mechanism. For example, the diffused magnetic atoms may be superparamagnetic at room temperature

and they have a random magnetic orientation with respect to each other. When the spin polarized electrons pass through the magnetic dead layer, their spin orientation may be influenced by the fields originated from the superparamagnetic particle, resulting in reduced spin polarisation. This explanation may cover the FM/organic/FM structure. However, one experiment has shown that the magnetic dead layer has a positive effect on the magnetoresistance [5]. As it is well know that the characteristics of an organic/FM interface is differ than oxide/FM interface, which results in different transport properties in both interfaces. One of the main characteristics of the organic/FM interface is the conductivity mismatch problem. The experiment in ref. x shows that the magnetic dead layer improves the magnetoresistance and this is attributed to overcoming the conductivity mismatch problem between the organic and ferromagnetic layer. Therefore, it can be concluded that the role of magnetic dead layer on the spin polarized transport is material dependent and determined by competition of the spin scattering mechanisms at the interfaces.

3.6.7.2 AFM and TEM studies of CuPc thin films

Figure 3.30 shows the AFM image of SiO_2/CuPc(2nm) single layer taken from 2x2 μm^2 area and the RMS roughness of CuPc layers in a thickness range of 2-8 nm. The RMS roughness of the 2 nm CuPc layer is found to be 0.39 nm and it is nearly independent of thickness. This low roughness in the CuPc layer allows us to make very smooth organic barrier in our devices.

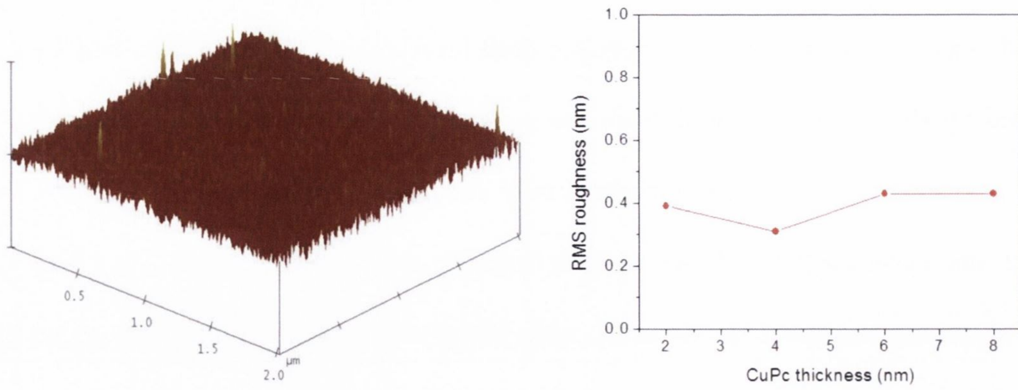

Figure 3.30. AFM image of SiO_2/CuPc(2nm) single layer and RMS roughness of the different CuPc single layers with thickness ranging from 2 to 8 nm.

Figure 3.31 shows the TEM image of one unpatterned stack. Here we used CoFeB and MgO as a bottom or top layer due to our earlier plan to make MgO/CuPc based hybrid spin valves. The CoFeB and MgO layers seem to have a good crystalline structure and a sharp interface. However, the CuPc/CoFe interface is not very clear and it seems to be rougher which might lead to spin scattering at the interface. This rough CuPc/CoFe interface is a critical issue for the spin injection into the CuPc layer.

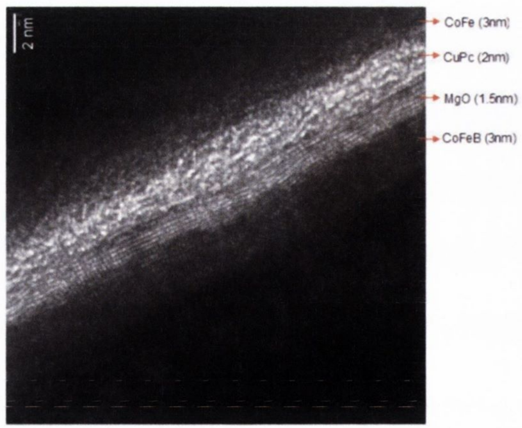

Figure 3.31. TEM image of an unpatterned stack.

3.7 Conclusion

Controlled deposition of metals on top of organic layers and formation of metal-organic contacts are the obvious requirements for many applications of organic semiconductors. In this chapter, physical and magnetic properties of metal-organic and metal-insulator-organic interfaces are studied using mainly the FFTM method, as well as AFM and TEM techniques. The FFTM method clearly indicates that formation of a magnetic dead layer at the metal/organic interface is evidence of reaction between metal atoms and organic molecules and also the creation of a diffusive interface, which is not a desirable result for organic devices or transport studies. However, inserting a thin insulator layer, irrespective of whether it is LiF or AlO_x, reduces the thickness of the magnetic dead layer due to the blocking of interdiffusion and preventing a chemical reaction at the interface. Furthermore, unless it is capping the organic layer, the bottom ferromagnetic layer oxidizes through the organic. At this point, besides using an insulator layer, a series of deposition strategies can reduce the problems related to interdiffusion. Firstly, to *freeze out* the interdiffusion, the substrate can be held at a low temperature during the organic deposition. Secondly, if the metals are deposited at a high rate, they are quickly forming larger aggregates which are then less mobile and diffuse less into the organic film. Thirdly, to reduce the energy of the impinging metal atoms using a noble gas causes a softer metal deposition. The AFM and XRR measurements show that organic materials can form as nice smooth thin films with low RMS roughness, which is also important to reduce the effect of Néel orange peel coupling in magnetic tunnel junction. The main feature of the TEM images and electron intensity profiles are that the interface roughness between organic and metal varies

from point to point indicating different amount of interdiffusion and also that interface roughness depends on the type of organic material.

3.8 Bibliography

[1] S. Sanvito, Nat Phys 6 (2010) 562.

[2] T.S. Santos, J.S. Lee, P. Migdal, I.C. Lekshmi, B. Satpati, J.S. Moodera, Physical Review Letters 98 (2007) 016601.

[3] J.H. Shim, K.V. Raman, Y.J. Park, T.S. Santos, G.X. Miao, B. Satpati, J.S. Moodera, Physical Review Letters 100 (2008) 226603.

[4] T. Ikegami, I. Kawayama, M. Tonouchi, S. Nakao, Y. Yamashita, H. Tada, Applied Physics Letters 92 (2008) 153304.

[5] Y. Liu, S.M. Watson, T. Lee, J.M. Gorham, H.E. Katz, J.A. Borchers, H.D. Fairbrother, D.H. Reich, Physical Review B 79 (2009) 075312.

[6] F.J. Wang, Z.H. Xiong, D. Wu, J. Shi, Z.V. Vardeny, Synthetic Metals 155 (2005) 172.

[7] F.J. Wang, C.G. Yang, Z.V. Vardeny, X.G. Li, Physical Review B 75 (2007) 245324.

[8] W. Xu, G.J. Szulczewski, P. LeClair, I. Navarrete, R. Schad, G. Miao, H. Guo, A. Gupta, Applied Physics Letters 90 (2007) 072506.

[9] V. Dediu, L.E. Hueso, I. Bergenti, A. Riminucci, F. Borgatti, P. Graziosi, C. Newby, F. Casoli, M.P. De Jong, C. Taliani, Y. Zhan, Physical Review B 78 (2008) 115203.

[10] H. Vinzelberg, J. Schumann, D. Elefant, R.B. Gangineni, J. Thomas, B. Buchner, Journal of Applied Physics 103 (2008) 093720.

[11] J.S. Jiang, J.E. Pearson, S.D. Bader, Physical Review B 77 (2008) 035303.

[12] J.-W. Yoo, H.W. Jang, V.N. Prigodin, C. Kao, C.B. Eom, A.J. Epstein, Synthetic Metals 160 (2010) 216.

[13] I.G. Hill, A. Rajagopal, A. Kahn, Y. Hu, Applied Physics Letters 73 (1998) 662.

[14] I.G. Hill, A.J. Makinen, Z.H. Kafafi, Applied Physics Letters 77 (2000) 1825.

[15] L.S. Hung, C.W. Tang, M.G. Mason, Applied Physics Letters 70 (1997) 152.

[16] T. Mori, H. Fujikawa, S. Tokito, Y. Taga, Applied Physics Letters 73 (1998) 2763.

[17] S.M. Sze, Physics of Semiconductor Devices, Wiley, New York, 1981.

[18] W. Brütting, S. Berleb, A.G. Mückl, Organic Electronics 2 (2001) 1.

[19] K. Zhang, PhD Thesis (2006).

[20] W. Xu, J. Brauer, G. Szulczewski, M.S. Driver, A.N. Caruso, Applied Physics Letters 94 (2009) 233302.

[21] N.S. McIntyre, M.G. Cook, Analytical Chemistry 47 (1975) 2208.

[22] P. Wu, E.Y. Jiang, C.D. Wang, Journal of Magnetism and Magnetic Materials 168 (1997) 43.

[23] S. Entani, M. Kiguchi, S. Ikeda, K. Saiki, Thin Solid Films 493 (2005) 221.

[24] L. Smardz, U. Kobler, W. Zinn, Journal of Applied Physics 71 (1992) 5199.

[25] B.D. Schrag, A. Anguelouch, S. Ingvarsson, G. Xiao, Y. Lu, P.L. Trouilloud, A. Gupta, R.A. Wanner, W.J. Gallagher, P.M. Rice, S.S.P. Parkin, Applied Physics Letters 77 (2000) 2373.

[26] Y.J. Lee, X. Li, D.-Y. Kang, S.-S. Park, J. Kim, J.-W. Choi, H. Kim, Ultramicroscopy 108 (2008) 1315.

[27] Z.T. Xie, W.H. Zhang, B.F. Ding, X.D. Gao, Y.T. You, Z.Y. Sun, X.M. Ding, X.Y. Hou, Applied Physics Letters 94 (2009) 063302.

[28] F. Borgatti, I. Bergenti, F. Bona, V. Dediu, A. Fondacaro, S. Huotari, G. Monaco, D.A. MacLaren, J.N. Chapman, G. Panaccione, Applied Physics Letters 96 (2010) 043306.

[29] S. Yuasa, T. Nagahama, A. Fukushima, Y. Suzuki, K. Ando, Nat Mater 3 (2004) 868.

[30] S.S.P. Parkin, C. Kaiser, A. Panchula, P.M. Rice, B. Hughes, M. Samant, S.-H. Yang, Nat Mater 3 (2004) 862.

[31] R.C. Sousa, J.J. Sun, V. Soares, P.P. Freitas, A. Kling, M.F. da Silva, J.C. Soares, Applied Physics Letters 73 (1998) 3288.

[32] J.S. Moodera, L.R. Kinder, T.M. Wong, R. Meservey, Physical Review Letters 74 (1995) 3273.

[33] C.H. Chen, J. Shi, Coordination Chemistry Reviews 171 (1998) 161.

[34] K.P. Krishnakumar, C.S. Menon, Journal of Solid State Chemistry 128 (1997) 27.

[35] G. Baburaya Kamath, C.M. Joseph, C.S. Menon, Materials Letters 57 (2002) 730.

[36] C.M. Joseph, C.S. Menon, Materials Letters 52 (2002) 220.

[37] S.A. Van Slyke, C.H. Chen, C.W. Tang, Applied Physics Letters 69 (1996) 2160.

[38] V.Y. Aristov, O.V. Molodtsova, Y.A. Ossipyan, B.P. Doyle, S. Nannarone, M. Knupfer, Organic Electronics 10 (2009) 8.

[39] V.S.N. Murthy, C. Krishnamoorthi, R. Mahendiran, A.O. Adeyeye, Journal of Applied Physics 105 (2009) 023916.

Chapter 4

MAGNETORESISTIVE CHARACTERISTICS OF ORGANIC/INSULATOR HYBRID DEVICES

4.1 Introduction

In this chapter, transport and in particular, magnetoresistive characteristics of some relatively well studied small-molecule-organic (SMO) semiconductors are presented such as Alq_3, CuPc, ZnPc and Znq_2. Two separate sets of devices are prepared as micron-size junctions using photolithography and shadow masking technique, for comparison. In the photolithography version, standard exchange-biased multi-layered stacks with a crystalline MgO spin filter layer were used, while amorphous AlO_x was chosen as the barrier for the ones prepared by the shadow masking technique. Further, the optimization of the AlO_x barrier and ferromagnetic electrodes in the shadow masking technique is presented, as is the optimization of the MgO cleaning process in the organic UHV chamber. The magnetoresistive characteristics of MgO/LiF based stacks were also studied. We start the description with the optimization experiments.

One of the main objectives of the thesis is to investigate the spin polarized transport in a ferromagnet/organic/ferromagnet organic spin valve structure. In the ideal case,

organic layer acts as a perfect spin transport layer which mediates the spins to travel for long distances due to the low spin scattering mechanisms. Furthermore, a perfect interface between organic layer and ferromagnetic electrode is the desired subject for the efficient spin injection into the organic layer from a spin reservoir. However, there are some experimental or material dependent difficulties such as interfacial problems between the organic and ferromagnetic materials or their electronic structures. For example, high barrier height at the organic/ferromagnet interface, formation of a dipole layer at that interface, conductivity mismatch problem and formation of a buried interface make the organic spin valves far from the ideal case. Experiments show that those problems can be reduced using an insulating layer at the organic/ferromagnet interface. In the case of tunneling, organic MTJs with an insulator/organic hybrid barrier have no greater advantage than the standard FM/I/FM MTJs. Furthermore, to insert an organic barrier into a standard MTJ will cause an extra effort and less TMR yield. In this aspect, using organic barrier together with an insulating layer does not provide a big advantage. So far, the experiments have shown that most of the devices with a bare organic layer (FM/O/FM) short when the thickness of the organic barrier is less than ~ 20 nm due to the pinholes or defects produced during the deposition in the barrier. However, the devices with a thin insulating barrier and an organic barrier show nice tunneling characteristics even the thickness of the organic barrier is only a few nanometres. The device characteristics can be clearly distinguished in the presence or absence of the organic barrier in this kind of hybrid devices. As a result, an insulating layer acts as a good buffer layer for the organics and provides better adhesion on the bottom layer, minimizing the imperfections in the organic barrier. In the case of very thick organic barriers, an insulating layer plays an important role for the spin injection into the organic spacer. First of all, the studies have shown that an oxide layer

introduced between the organic barrier and metal layer improves the electron injection efficiency into the organic layer by reducing the injection barrier height. Fig. 3.2 shows a typical band diagram of metal/organic or metal/insulator/organic structures, where the metal/insulator/organic interface has smaller barrier height than metal/organic interface. In this point of view, an insulating layer acts as an important role for the efficient spin injection. Moreover, organic materials tend chemically to react with the metallic electrodes when they come into contact. This results in to form a dipole layer, magnetically dead layer or an interdiffusion at the organic/metal interface, which may change the spin polarized transport characteristics of the devices. In this point, it is a critical issue to produce a sharp and unreacted interface in a FM/O/FM organic spin valve. For example, formation of a dipole layer at the interface can introduce some states into the organic band gap, which localizes the tunneling spins. OLED studies have proven that the presence of an insulating layer at the organic/metal interface suppresses the formation of these gap states and lowers the electron injection barrier height, resulting in efficient electron injection and enhanced EL output.

4.2 Spin valve test stacks

4.2.1 Calibration of AlO_x barrier prepared by using shadow masking technique

AlO_x is one of the best insulators used in spin electronic devices as a tunnel barrier [1] with a highest reported TMR ratio of 70% [2]. It can be deposited in thin film form directly from an AlO_x target by sputtering or it can be obtained by oxidizing an Al thin

film. Here, we explain the experimental procedures to obtain AlO_x tunnel barrier by oxidizing an Al thin film. The method chosen for oxidation process is a multistep oxidation. This method has been used to obtain dense and uniform AlO_x barriers which can give high TMR response in many spin electronic devices [3-5]. In this thesis, a four-step oxidation process is used to obtain AlO_x barrier for all devices prepared by using shadow masking. Here, a total of 2 nm of Al film was oxidized step by step. Firstly, a bottom ferromagnetic electrode was deposited through the shadow mask which has micron-sized cut-outs on it, ranging from 100 μm to 250 μm. Then, a 0.6 nm or 0.5 nm thin layer of Al was deposited on a whole substrate including the bottom electrode and the sample was then transferred to the load lock to oxidize the Al film in a pure oxygen atmosphere. The pressure in the load lock was 2×10^{-6} mbar before transferring the sample. Then, pure oxygen was injected to the load lock raising the pressure to 150 Torr and the exposure time was kept at 5, 7, 15 or 30 min in the calibration processes to find the optimum thickness and exposure time. Later, the load lock was filled with nitrogen gas until the pressure reaches atmospheric pressure to dilute the oxygen, in an attempt to prolong the service life of the TMP blades during pump down of the oxygen gas from the load-lock. Then, the sample was transferred back to the main chamber to deposit another 0.5 nm or 0.4 nm Al layer. The same oxidation process is repeated for subsequent thin Al layers. The important thing is that 2 nm Al was deposited in total for all samples. We varied either the thickness of the Al layer or the oxidation time. For example, we used a four-step deposition for 2 nm Al with 0.5nm+0.5nm+0.5nm+0.5nm or 0.6nm+0.4nm+0.6nm+0.4nm and oxidized each ultra-thin layer before depositing the next ultra-thin layer, where different oxidation times were used for each ultra-thin Al layers. Figure 4.1 shows the TMR response of 100 x 100 μm^2 devices with different AlO_x tunnel barriers prepared in different

oxidation thickness and time, where the stack is $SiO_2/Co_{50}Fe_{50}$ (12 nm)/AlO_x (A, B, C and D)/Co (18 nm). A, B, C and D represent the preparation conditions of the AlO_x barrier, where the parameters used for Al thickness and oxidation are following:

A: 0.6 nm (15 min) + 0.4 nm (30 min) + 0.6 nm (15 min) + 0.4 nm (30 min)

B: 0.6 nm (30 min) + 0.4 nm (30 min) + 0.6 nm (30 min) + 0.4 nm (30 min)

C: 0.5 nm (5 min) + 0.5 nm (15 min) + 0.5 nm (5 min) + 0.5 nm (15 min)

D: 0.5 nm (7 min) + 0.5 nm (15 min) + 0.5 nm (7 min) + 0.5 nm (15 min).

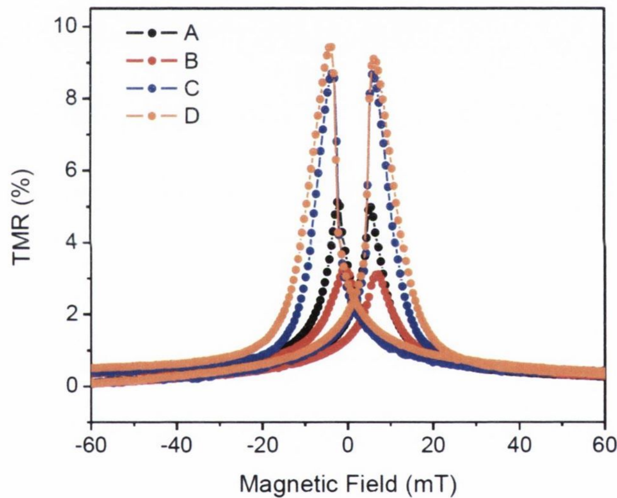

Figure 4.1. TMR response of the AlO_x based MTJ devices, comparing the formation of AlO_x in different preparation conditions.

The key issue is to oxidize the first thin layer of Al without oxidation of the ferromagnetic electrode, which can reduce the spin polarization of the current transmitted through the CoFe/Al interface, thus lowering the TMR ratio. The maximum (~10 %) TMR is observed when the thickness of the first and subsequent ultra-thin Al

layers is 0.5 nm. The TMR did not change so much with the oxidation time, but it dropped by half when the thickness of the first layer was increased from 0.5 nm to 0.6 nm. The reason is presumably the better oxidation of the thin layer than the thick one. Keeping the same parameters as in process D for Al oxidation, we continued the optimization of the stack by playing with the ferromagnetic electrodes. Figure 4.2 shows the TMR response of the three different stacks, where preparation of AlO_x is the same in Figure 4.1 (D) but the electrodes and their positions are different. The graph clearly shows that using CoFe layers on both sides improves the TMR ratio a few per cent. This may be attributed to the higher spin polarization of CoFe, compared to Co, where the spin polarizations of $Co_{50}Fe_{50}$ and Co are 51 % and 45 %, respectively [6].

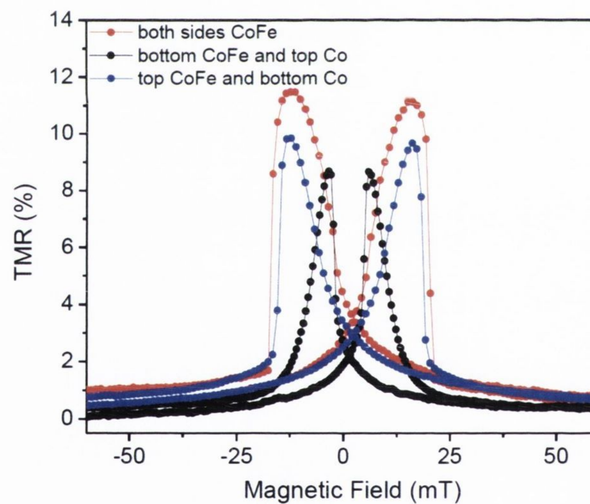

Figure 4.2. TMR response of the stack D, showing the effect of the positions and types of ferromagnetic electrodes in the stack.

To see the reproducibility of the highest TMR in this stack, two more new sets of sample were prepared using the same experimental parameters. The new stacks

confirmed that the approximately 12 % TMR is reproducible. For comparison, the RA and TMR ratio of the samples are summarized in Table 4.1. The TMR response of the samples is consistent, while the RA product shows somewhat bigger variations from sample to sample. The possible reasons may be related to the formation of a non-uniform barrier thickness. The deposition rate of the Al layer was 0.1 Å/sec and the shutter was manually controlled. In this case, it is expected that a few seconds offset for opening or closing the shutter, results in a small variation in the barrier thickness from sample to sample. Also, non-uniform oxidation of Al may be another reason of small variation in RA.

	SET 1		SET 2		SET 3	
	TMR (%)	RA ($M\Omega\mu m^2$)	TMR (%)	RA ($M\Omega\mu m^2$)	TMR (%)	RA ($M\Omega\mu m^2$)
J-1	11.7	39.8	12.8	21.1	11.8	28.0
J-2	9.2	30.6	12.4	21.9	12.5	33.5
J-3	10.4	35.5	11.9	21.9	12.8	31.6
J-4	11.5	44.0	12.9	22.9	11.6	33.6
J-5	11.4	40.7	12.7	22.7	8.5	19.0
J-6	11.0	38.1	11.7	20.4	11.8	29.0

Table 4.1. TMR response and RA product of the three sets of CoFe (10nm)/AlO_x (D)/CoFe (18nm) stack, which is used as a reference stack in AlO_x/organic/AlO_x based hybrid devices. Here, the junction area in set 1 and set 2 is 250x250 μm^2 while it is 100x100 μm^2 in set 3.

To estimate the barrier thickness and barrier height of the devices, Brinkman's equation was used for set 1 and set 2, and the results are quite consistent for each set of the samples [7]. In the small bias region, fitting the conductance curve of the samples for the junctions J-4 in set 1 and J-5 in set 2, the barrier thickness and barrier height were obtained as 31.2 Å and 0.692 eV for J-4 in set 1, and 28.3 Å and 0.672 eV for set 2 (see Figure 4.3).

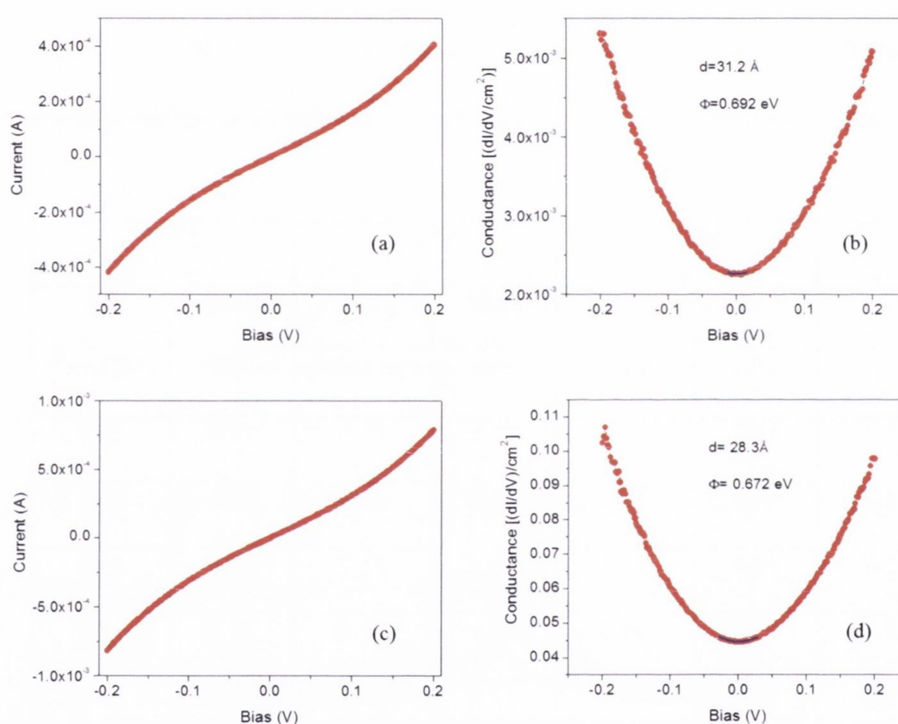

Figure 4.3. The I-V and conductance graphs of the J-4 in set 1 (a,b) and J-5 in set 2 (c,d)

For further analysis of the AlO_x based MTJs, the I-V curve and TMR were measured at various fixed temperatures. The TMR ratio increased with decreasing temperature, which is seen in many MTJs in the literature, and the maximum TMR of ~ 28 % was measured at 20 K. Decreasing TMR with increasing temperature is attributed to two

origins [8]. The dominant mechanism is related to the decreasing spin polarisation with the temperature ($1-\alpha T^{3/2}$) in the direct elastic tunneling process due to the thermally exited spin waves, where α is a material-dependent constant. The second and small mechanism is thermally assisted spin-independent conductance. The I-V curve slightly changed with temperature and the RA increased from 29.0 $M\Omega\mu m^2$ to 42.4 $M\Omega\mu m^2$, which is expected for direct tunneling process. To summarize the above results, Al was successfully oxidized using the multi-step oxidation process and a reasonable room temperature TMR effect was observed in the stack of CoFe (10nm)/AlO_x (D)/CoFe (18 nm). For the remainder of this chapter, this stack is going to be used as a reference layer for the organic-based hybrid devices which are prepared using shadow masking.

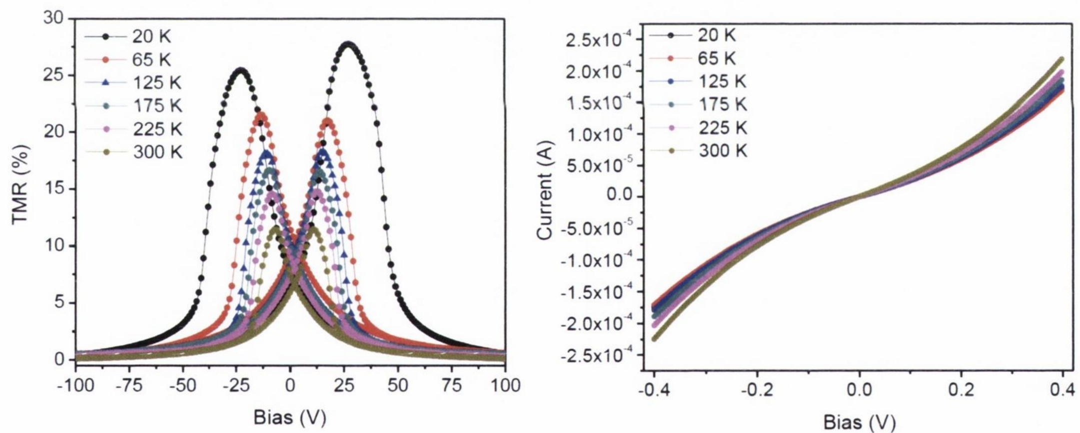

Figure 4.4. TMR and I-V responses of the stack of CoFe (10nm)/AlO_x (D)/CoFe (18nm) as a function of temperature.

4.2.2 Calibration of the MgO cleaning process

MgO has become the favourite tunnel barrier used in MTJ structures due to its spin filtering for the (Δ_1) states which results in impressive room temperature TMR (~ 604%) [9] since its invention at 2001 [10]. In the last decade, research in the spin electronics field was focused on MgO based magnetic tunnel junctions in order to improve the performance of the MTJ devices as it mentioned in Chapter 1. In this thesis, MgO was used in two different types of experiment as a hybrid barrier with organic layers; air exposed MgO/organic or Ar-ion cleaned MgO/organic hybrid barriers.

In the first type of experiments, MgO and bottom stacks were prepared in the Shamrock tool by sputtering and the samples were then transferred to Camellia to deposit organic and top ferromagnetic layers. The disadvantage of this type of experiment was that MgO was exposed to air when the samples were transferred between the deposition chambers, resulting in formation of a magnesium hydroxide layer on the MgO surface, which degrades the quality of MgO. In this type of experiments, MgO based stacks without organic layers show a maximum of ~ 16 % TMR at room temperature. In a second type of experiments, we overcome this problem by cleaning the MgO surface using a low angle Ar-ion etching process. This section is related to the second type of experiment, and the presentation of the optimisation data for the Ar-ion cleaning process.

Figure 4.5 shows the schematic of sample preparation processes. Firstly, the bottom stack including the MgO barrier was deposited by sputtering on a SiO_2 substrate in the Shamrock tool, and it was transferred to the magnetic annealing furnace. Here, the

stack was post annealed at 350 °C for 60 minutes in a field of 800 mT to crystallize the amorphous $Co_{40}Fe_{40}B_{20}$ layer and set the exchange bias. The stack was then moved to the organic UHV chamber and exposed to the Ar-ion beam in order to clean the MgO surface, with the parameters of Ar-ion exposure summarized in Table 2.1 in Chapter 2. In order to obtain the optimum exposure time, the MgO surface was cleaned for 0, 30, 60, 80, 120 and 180 seconds, where new identical fresh stacks were used in each cleaning process. Finally, the stack was completed by depositing 5 nm CoFe and 5 nm Cu, and patterned into micron-size junctions using UV photolithography.

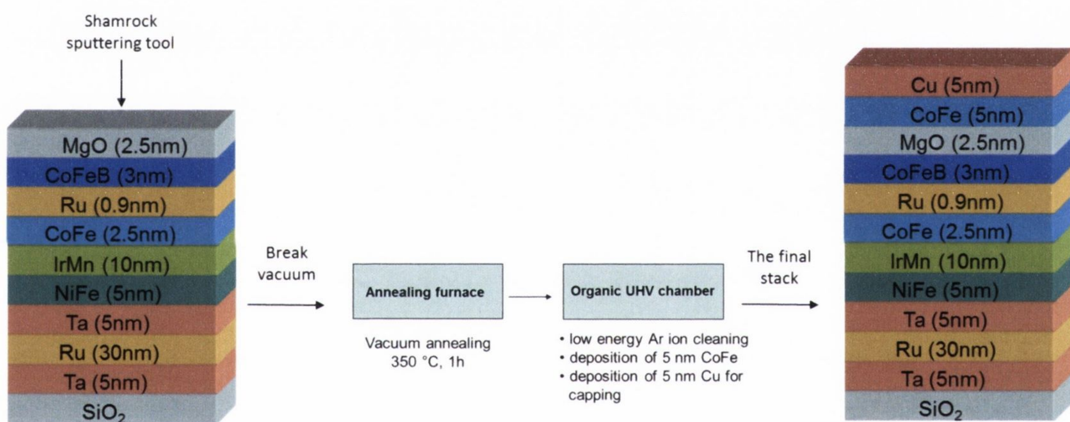

Figure 4.5. Schematic representation of sample preparation using Ar-ion cleaning process

Magnetoresistive characteristics of the samples were measured using standard four-point probe technique and shown in Figure 4.6 as a function cleaning time. The results showed that 16 % of TMR was measured without cleaning. This TMR value is low with respect to the standard fully vacuum-deposited MgO based MTJs due to the formation of the magnesium hydroxide layer on the MgO surface. Then, 30 seconds cleaning doubled the TMR and the TMR increased further with cleaning time. We

measured maximum ~120 % of TMR for a cleaning time of 80 seconds. After this point, the TMR decreased with increasing cleaning time. The reason is over-cleaning, which presumably introduces defects in the MgO barrier. Furthermore, the RA value of the devices which show highest TMR was ~ $1x10^5$ $\Omega\mu m^2$ and this is close to the expected literature value for 2.5 nm thick MgO barrier [11]. The maximum ~ 120 % TMR obtained for 80 seconds etching of the MgO surface and is a good starting point for the MgO/organic based hybrid devices to observe a measurable room temperature MR.

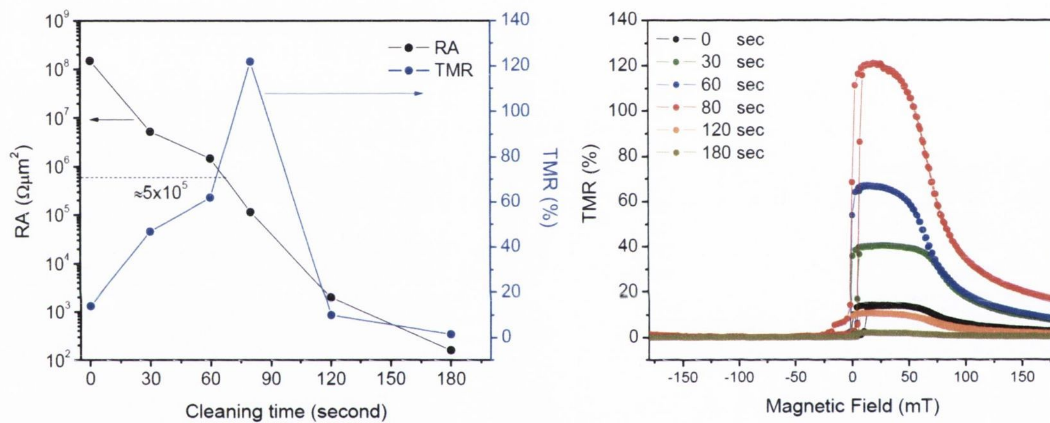

Figure 4.6. RA and TMR response of the samples with different cleaning time for MgO surface.

4.2.3 Magnetoresistive characteristics of MgO/LiF based MTJs

The interface studies in Chapter 3 showed that introducing a thin layer of LiF between Alq_3 and Co provides great structural and magnetic improvement of the organic/Co. However, the important point is to know how the LiF layer affects spin polarized transport. In order to understand whether LiF favours spin polarized transport or not,

we made two sets of exchange-biased MTJ stack with and without the LiF layer. The bottom parts of the stacks were prepared in the Shamrock sputtering tool, where the stacks are SiO_2/Ta (5)/Ru (30)/Ta (5)/NiFe (5)/IrMn (10)/CoFe (2.5)/Ru (0.9)/ CoFeB (3)/ MgO (2.5). Then, the stacks were transferred to the annealing furnace to set the exchange bias and crystalline the CoFeB layer. Here, the stacks were annealed at 350 °C for 1 hour in a field of 800 mT. After that, they were transferred to the organic UHV chamber. Using the same process as in section 4.2.2, the MgO surface was cleaned from the magnesium hydroxide layer. Then, the top stacks, LiF (t=0, 1 nm)/CoFe (5 nm)/Cu (5 nm), were deposited on MgO and the full stacks were patterned into micron-sized junctions using UV lithography.

Figure 4.7 compares the I-V characteristics of the 4 x 12 μm^2 MTJ junctions with and without LiF layer. The I-V curves of the junctions are non-linear, showing that the transport is via tunneling through the barrier, and introducing the LiF layer caused a large jump in the device resistance from 16 kΩ to 49 MΩ. Furthermore, inserting the 1 nm LiF layer reduced the TMR from 120 % to 5 % at room temperature (see Figure 4.8). The data indicates that the LiF layer kills the spin polarization when the electrons tunnel through it. Therefore, our results suggest to use another barrier layer, MgO or AlO_x, between the organic and ferromagnetic materials, which allows the spin polarized transport in spin electronic devices.

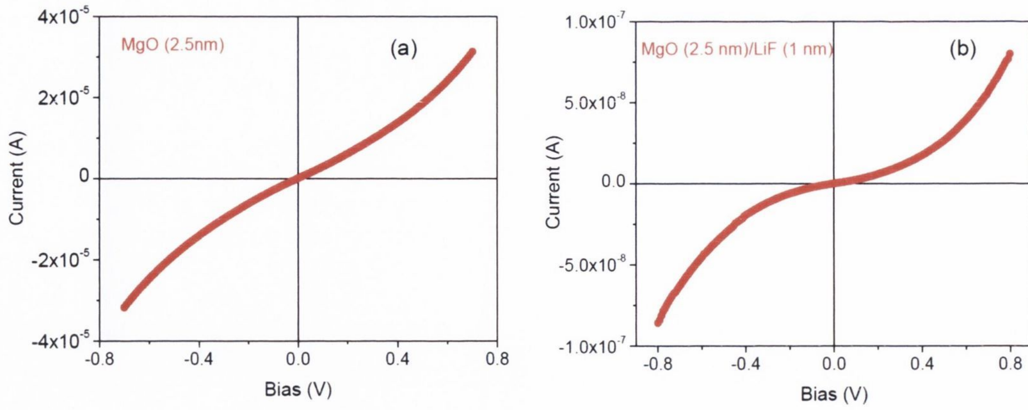

Figure 4.7. I-V characteristics of MgO (2.5 nm)/LiF (t) based hybrid devices when t=0 nm (a) and t=1 nm (b).

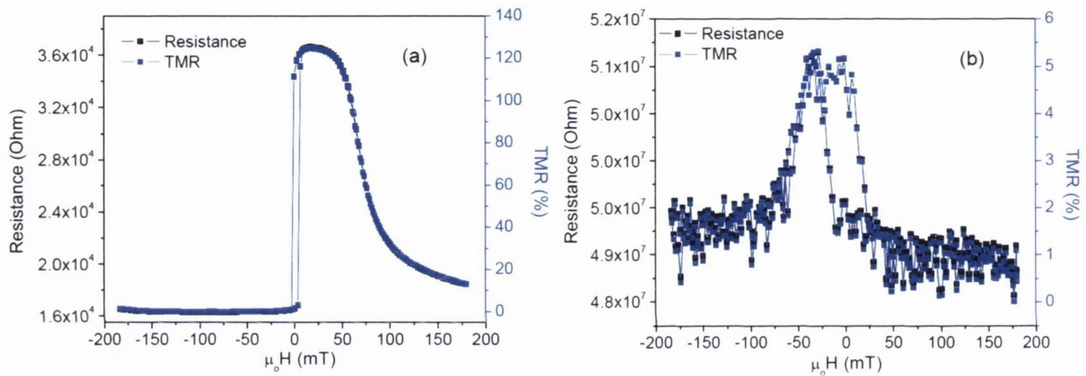

Figure 4.8. TMR characteristics of MgO (2.5 nm)/LiF (t) based hybrid devices when t=0 nm (a) and t=1 nm (b).

4.3 Alq_3 based hybrid organic spin valves

In this section, electrical and magnetoresistive characteristics of Alq_3-based hybrid organic spin valves are investigated combining Alq_3 with either MgO or AlO_x. The hybrid barriers were prepared under different conditions, and there are four types of

those: air exposed MgO/Alq_3 hybrid barrier, cleaned MgO/Alq_3 hybrid barrier and $AlO_x/Alq_3/AlO_x$ hybrid barrier

4.3.1 Magnetoresistive characteristics of air exposed MgO/Alq_3 based hybrid devices

4.3.1.1 Sample preparation

Exchanged-biased bottom stacks were prepared in the Shamrock tool with interconnected chambers for metal and oxide depositions with a base pressure of $2x10^{-8}$ Torr for oxide and $2x10^{-7}$ Torr for metal depositions. First, a Ta/Ru/Ta three-layer stack was deposited to get a thick bottom contact with low resistance and smooth surface. Then, a NiFe layer was deposited on the three-layer stack. The purpose of depositing NiFe is to set [111] crystal structure for the antiferromagnetic IrMn layer because good exchange bias between IrMn and CoFeB layers are achieved when the IrMn layer has [111] texture. After depositing IrMn layer in the metal deposition chamber 'A', the sample was transferred to the oxide deposition chamber 'B' for CoFeB and MgO depositions without breaking vacuum. Later, the sample was moved to the annealing furnace breaking the vacuum. Here, the stack was vacuum annealed at 350 °C during 1 hour in a field of 800 mT, in order to crystallize the amorphous CoFeB layer and set the exchange bias. After that, the stack was transferred to Camellia to deposit Alq_3 and Co layers. Here, the Alq_3 layer was deposited by thermal evaporation with various thicknesses (0-8 nm). The deposition rate was kept at 0.01 nm/s. Then, the 10 nm Co layer was deposited by using electron beam evaporation and the sample was capped with 5 nm Cu. Finally, the full stack was then patterned in micron-size junctions

ranging from 5 x 5 μm^2 to 50 x 150 μm^2. Figure 4.9 shows the evolution of the air exposed MgO/Alq_3 based stack.

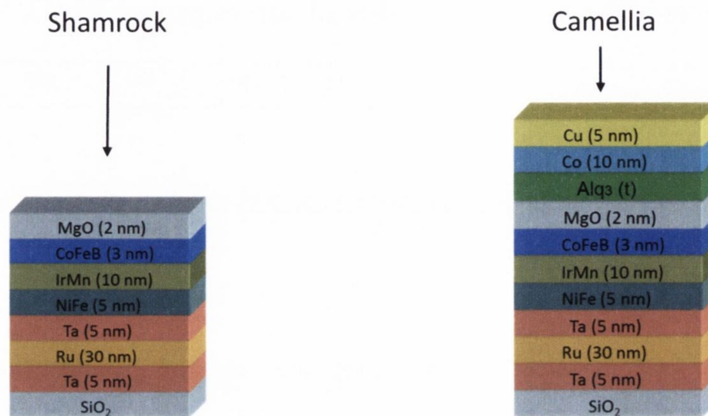

Figure 4.9. Evolution of air exposed MgO/Alq_3 based stack.

4.3.1.2 Results

The process yielded a reasonably high proportion of working junctions with a scatter of TMR values of only ±2% of the average value. The yield of non-shorted junctions was ~40%. Figure 4.10 shows the magnetoresistive characteristics of the MgO/Alq_3 based hybrid devices. The devices showed maximum ~ 16 % TMR at room temperature, for t = 0, which falls to ~ 12 % on inserting the Alq_3 and remains unchanged with increasing barrier thickness. The data indicates that there is no significant reduction of MR in the hopping regime, at least up to 8 nm, and three-quarters of spin polarization is preserved with an Alq_3 layer of whatever thickness.

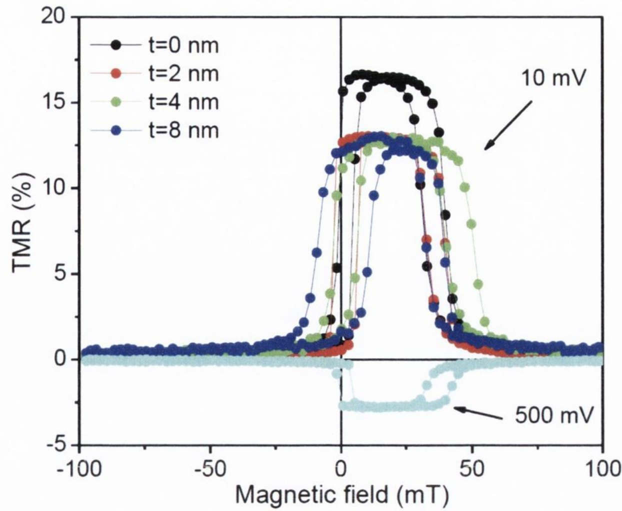

Figure 4.10. TMR characteristics of air exposed MgO (2 nm)/Alq_3 (*t*) based hybrid devices with different thicknesses of Alq_3 at 10 mV. Also, the curve for *t*= 2 nm at 500 mV is included.

The sign change of MR at a positive bias of about 250 mV for the 2 nm Alq_3 tunnel barrier opens a question of imperfections in the barrier. It was demonstrated that imperfections in the barrier lead to imbalance transfer rate between the majority and minority spins in the current through the pinhole channels, introducing inversion of MR sign [12,13]. Also, bias dependent sign change of MR was observed by Yoo et al. [14] and related to the competition of pinhole and TMR channels. Another mechanism which may govern the sign chance of MR is related to formation of hybrid states between the organic barrier and ferromagnetic electrode, resulting in alternation of the sign of the spin polarization of the interface. The mechanism is explained in Chapter 1 or Ref. [15] in this chapter. The critical question is does the observed MR arise from the imperfections in the barrier or spin-conserving transport? To find the answer, low temperature transport measurements are required but variation of RA as a function of organic layer thickness, gives an idea about the transport mechanism.

Figure 4.11 shows the variation of RA with Alq_3 thickness. For example, for the 20 x 20 μm^2 junctions, RA $\approx$ 0.4 MΩ μm^2 for t = 0 nm; 2.8 MΩ μm^2 for t = 2 nm; and 19 MΩ μm^2 for t = 4 nm. It is clear to see from the graph that RA curve has two different slopes, showing that different mechanisms govern the transport in different Alq_3 thickness regimes. We do not expect ballistic tunneling in the 4-8 nm thick films. Initially, the RA increased exponentially with increasing barrier thickness, and then tended to saturate. Assuming the tunneling resistance of the Alq_3 barrier increases exponentially with thickness as $\exp(t/t_0)$, and the resistance in the hopping regime increases as t, the total RA product of the composite barrier is the sum of the resistance of the parallel tunneling and hopping channels

$$RA(t) = \frac{1}{[2RA(0) + \rho t]} + \frac{1}{[2RA(0)exp(t/t_o)]}, \tag{4.1}$$

where RA(0) is the RA product of the MgO barrier and t_o is the characteristic tunnel thickness.

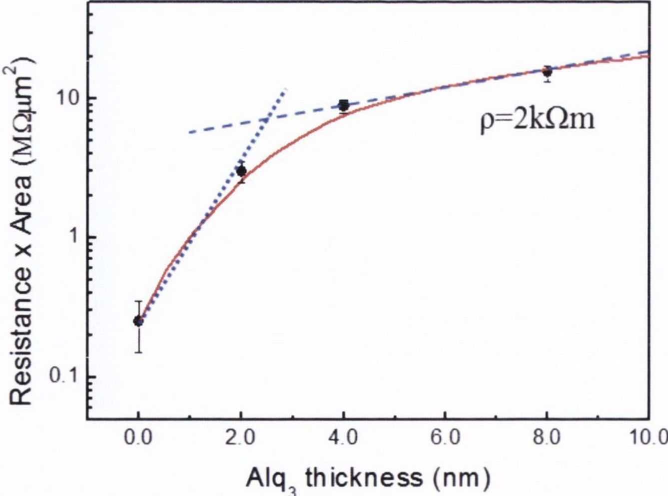

Figure 4.11. Resistance-area product plotted as a function of Alq_3 barrier thickness in MgO/Alq_3 MTJs. The red curve shows the fitting.

The model agrees with the experimental data. The characteristic thickness deduced from the fitting is 0.8 nm and the resistivity of the organic film in the hopping regime is ρ=2.0 kΩ.m, which agrees with a literature value for conducting amorphous films of this material [16]. Now let's turn to the sign chance of MR. If the imperfections in the barrier were the dominant mechanism for the MR sign such as metallic short-circuits or pinholes, a linear RA would be expected with increasing barrier thickness. Therefore, formation of a hybrid state at the organic/ferromagnet interface seems to be the source of sign change mechanism. However, we have to consider the MgO/Co interface as well because the device without organic presents the sign change of MR at about 0.6 V. Figure 4.12 shows the bias dependent TMR curve of the devices. Apart from the sign chance, the bias dependent TMR curves showed two other main features; asymmetric bias-dependent TMR and shifting the centre of TMR. The asymmetric shape of that curves has been observed for organic barriers [17,18] and can be related to the asymmetric nature of the top and bottom interfaces of the barrier in terms of the roughness, structural defects and different electronic structures of the top and bottom interfaces. A more detailed study about the sign change of TMR has been studied for carbon contaminated Fe-C/MgO or oxygen induced Fe-O/MgO interfaces and the results suggested that existing of a specific filtering effect related to the contamination of barrier/ferromagnet interface induces a sign change of TMR [19,20].

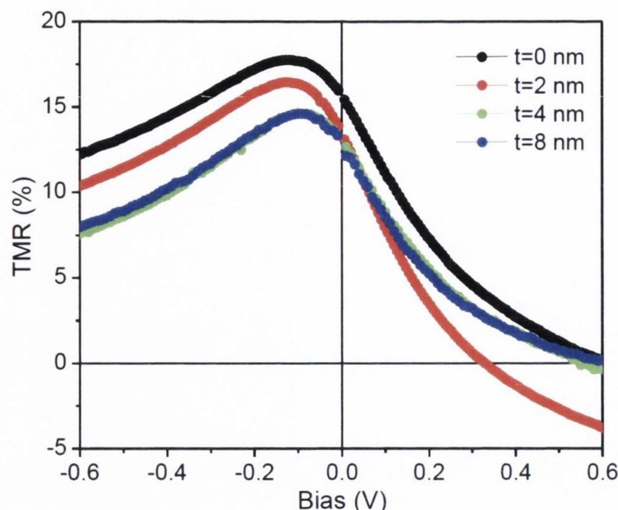

Figure 4.12. Bias dependent TMR characteristics of MgO/Alq_3 based hybrid devices.

4.3.2 Magnetoresistive characteristics of argon ion cleaned MgO/Alq_3 based hybrid devices

4.3.2.1 Sample preparation

In this section, we investigate the magnetoresistive characteristics of hybrid devices with argon ion cleaned MgO and Alq_3 barriers. The purpose of this section is to eliminate the interfacial effects which come from the MgO/air interface and improve the device performance. The exchanged biased and bottom pinned multilayer stacks were deposited in Shamrock tool including the 2.5 nm MgO barrier. The stacks are slightly different from stacks in section 4.3.1. In this case, the bottom ferromagnetic layer was pinned by artificial antiferromagnet depositing CoFe (2.5 nm) and Ru (0.9 nm) layers. This process provides better antiferromagnetic alignment of bottom and top ferromagnetic layers by separating the coercive fields. Then, the samples were transferred to the magnetic annealing furnace by breaking the vacuum. Here, the same

process was applied as in the previous section, annealing at 350 °C for 1 hour in a field of 800 mT. The samples were then moved to organic UHV chamber. Firstly, using the calibrated etching process which is explained in section 4.2.2, MgO surface was cleaned by Ar-ion beam for 80 seconds. Then, Alq_3 layers were deposited on clean MgO surface in various thicknesses (t= 0, 1, 2 and 3 nm), where we could only managed to pattern the samples up to 3 nm thick Alq_3 layer due to the lithography problems. Next, the stacks were completed by depositing CoFe (5 nm) and Cu (5 nm) layers and they were then patterned into the micron-size junctions using UV lithography. Figure 4.13 shows the evolution of cleaned MgO/Alq_3 based stacks.

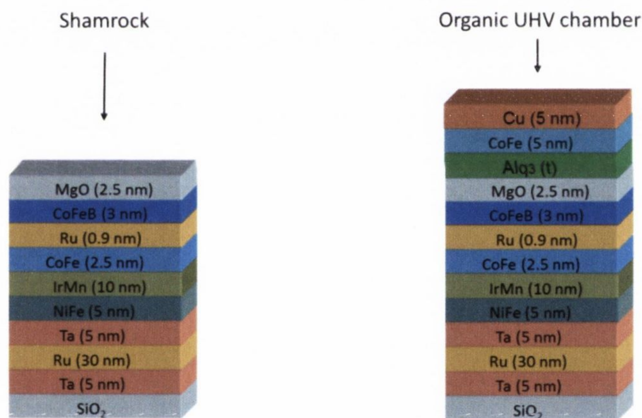

Figure 4.13. Evolution of the cleaned MgO (2.5 nm)/Alq_3 (t) based stacks.

4.3.2.2 Results

This process yielded very high proportion of working junctions (almost 90 %) with a scatter of TMR values of only ±1 %. At 300 K, the TMR characteristics of the stacks are shown in Figure 4.14, where the barrier is argon ion cleaned MgO (2.5 nm)/Alq_3 (t).

The reference stack, for which t= 0 nm, showed ~ 120 % TMR and inserting 1 nm Alq_3 between MgO and CoFe reduced the TMR value to ~ 48 %. Then, TMR decreased for the greater Alq_3 thicknesses, where it is ~ 31% for t=2 nm and ~21% for t=3 nm. The data indicates that Alq_3 layer reduces the TMR ratio but a remarkable TMR value still remains at room temperature.

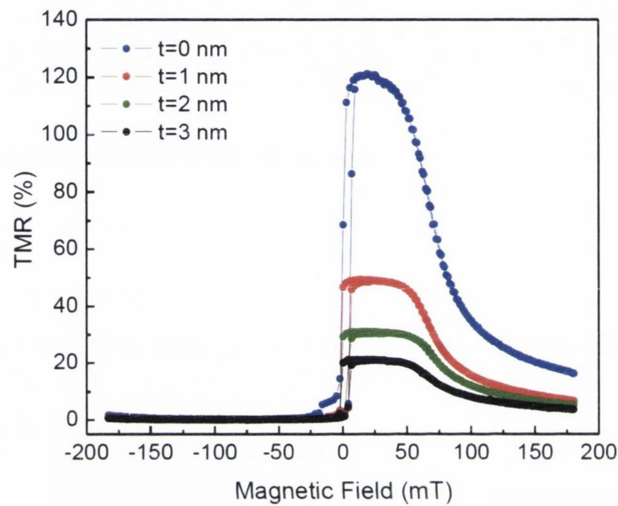

Figure 4.14. Room temperature TMR characteristics of argon ion cleaned MgO (2.5 nm)/Alq_3 (t) based hybrid devices.

We shall now address the variation of RA with increasing Alq_3 thickness. The left panel in Figure 4.15 represents our data and right panel represents the literature data taken from Ref. [21]. The results are consistent with that literature data, where the transport is by tunneling and the sign of MR is positive at low bias (see Figure 4.15 right panel). The RA increases exponentially with increasing Alq_3 thickness. For example, for the 5x5 μm^2 junctions, RA $\approx$ 0.9 MΩ μm^2 for t=0 nm; $\approx$ 2.4 MΩ μm^2 for t=1 nm; $\approx$ 9.4 MΩ μm^2 for t=2 nm; and $\approx$ 40.2 MΩ μm^2 for t=3 nm, which rules out any short-circuits or

pinholes in the barrier. The RA would likely follow a straight line with the Alq_3 thickness if there were pinholes in the barrier, which is shown in the right top panel in Figure 4.15. Furthermore, the resistance of the device slightly changes with increasing Alq_3 thickness.

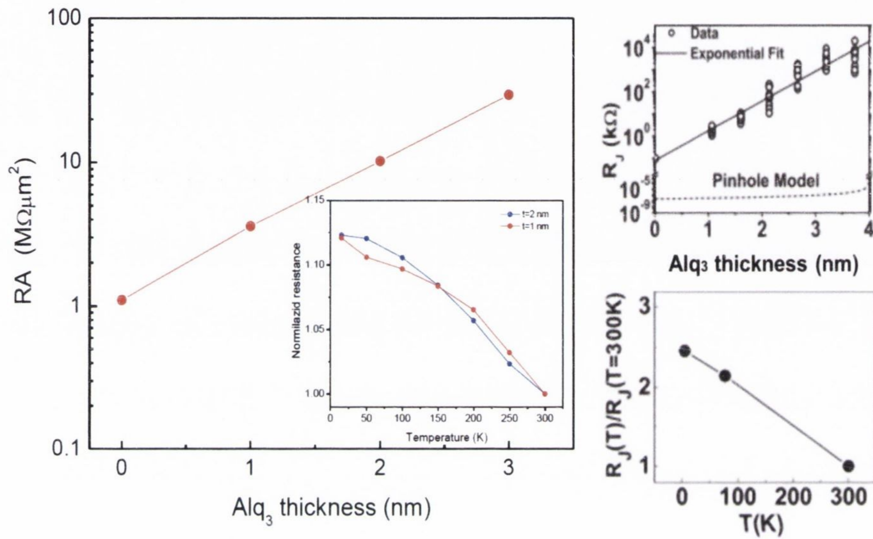

Figure 4.15. The left panel shows our experimental data while the right panels show the data taken from Ref. [21]. In both data, an exponential increase of RA with Alq_3 thickness was seen and the RA changed slightly with temperature. The stack used in Ref. [21] was Co (8 nm)/AlO_x (0.6 nm)/Alq_3 (1.6 nm)/NiFe (10 nm).

The bias dependent TMR curves exhibited results consistent with the literature. Figure 4.16a compares our results, where the effect of air exposed MgO and Ar-ion cleaned MgO on the bias dependent TMR are compared in the absence of an organic layer. Also, literature data taken from Ref. [11] are shown for the comparison in Figure 4.16b, where the stacks are carbon contaminated Fe-C/MgO/Fe or Fe/MgO/Fe. Off course, we expect different TMR response for the different stacks, but we here focus on the general

features in the bias dependent TMR curves. In the case of cleaned MgO barrier in Figure 4.16a, the TMR curve showed a symmetric behaviour and there is no sign change at the any bias regime, reflecting a good MgO barrier. However, in the case of air exposed MgO a large asymmetry and sign change of TMR were observed. The strong asymmetry, sign change of TMR and shifting the centre of maximum TMR have not been clearly explained in terms of the theoretical predictions. However, a possible mechanism is considered to be the modification of interfacial density of states [11,19,20], which changes the propagation of majority and minority spins with the Δ_1 and Δ_5 symmetries. When the top electrode is deposited on a contaminated MgO surface, the interface surface state of ferromagnetic electrode shifts slightly upwards in energy with respect to the clean one and new energetic states are opened for the electrons in the antiparallel configuration, where the new states exhibit symmetry, which is prohibited before contamination. This results in a strong enhancement of the antiparallel conductivity with respect to the parallel one and antiparallel conductance overcomes the parallel one in an applied bias. As a result, a strong asymmetry in Figure 4.12 can be related to the interfacial spin selective density of states of the top electrode when it is deposited either on contaminated MgO or Alq_3 thin films. Furthermore, the organic based stacks showed an inconsistent decay rate in the positive bias in Figure 4.12. This might be due to the competition of both MgO/air/Alq_3 and Alq_3/Co interfaces for the spin selective transport in the devices.

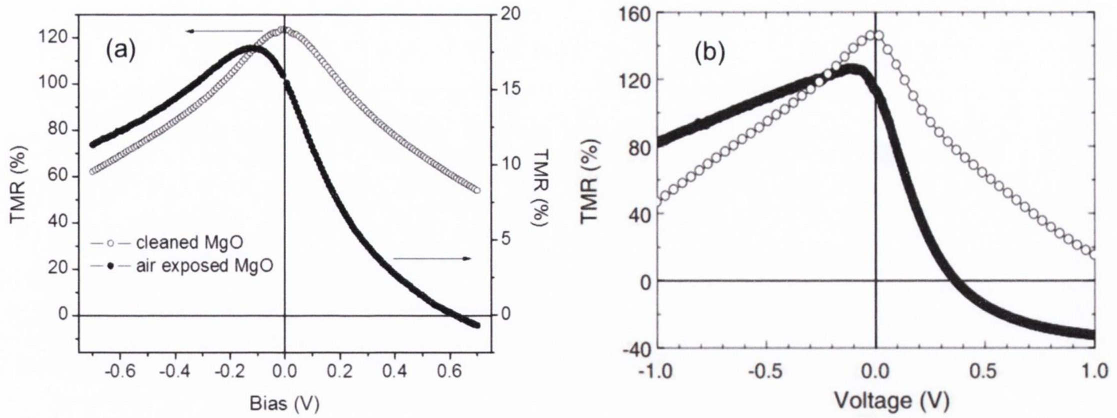

Figure 4.16. Magnetoresistance curves as a function of applied bias measured from contaminated or uncontaminated MgO based tunnel junctions, where the data taken from our study (a) and literature (b) [11] (note that the scales on the graphs are different). The black solid lines in both figures represent the TMR of devices which have contaminated interfaces.

The bias dependent TMR curves of the cleaned MgO (2.5 nm)/Alq_3 (t) based devices are shown in Figure 4.17, which were extracted from parallel and antiparallel I-V. The effect of introducing organic layer at the MgO/CoFe interface can be seen clearly if we compare the TMR curves with and without organic layers. Whereas the cleaned MgO/Alq_3 based devices showed strong asymmetric curves with applied bias and a sign change of MR, the device without organic showed quite symmetric curve without a sign chance. Therefore, we can eliminate the effect of MgO/Alq_3 interface on the transport mechanism and consider that the asymmetric shape originates from the Alq_3/CoFe interface. Unlike the air exposed MgO/Alq_3 based devices in Figure 4.12, the cleaned MgO/Alq_3 based devices showed a systematic decay in the positive bias in Figure 4.17. The bias dependent TMR curves showed a faster decay with increasing organic thickness and the centre of the maximum TMR shifts slightly from zero bias. Here, Alq_3/CoFe interface behaves the same with contaminated Fe-C/MgO or air

exposed MgO/Co interface. Furthermore, the sign change voltage is approximately 1 V for t=1 and 2 nm but 0.35 V for t=3 nm. We always expect a reaction and interdiffusion between ferromagnet and organic, which is confirmed by interface studies in Chapter 3 and some literature works. So, the question is why does the TMR decrease faster for t=3 nm.

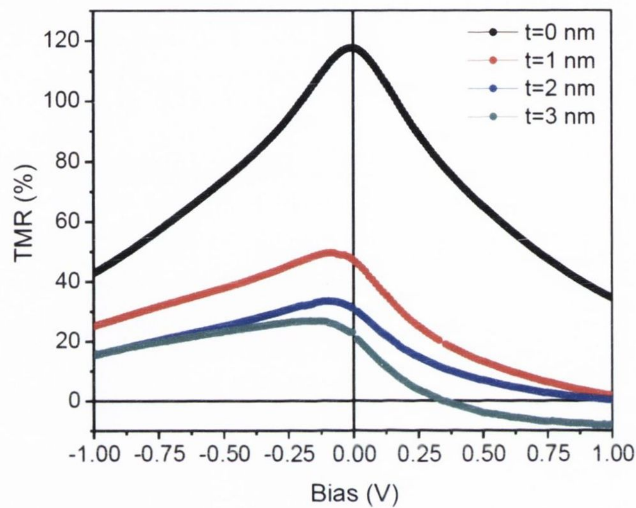

Figure 4.17. Bias dependent TMR curves of the MgO (2.5 nm)/Alq_3 (t=0, 1, 2 and 3 nm) based hybrid devices.

A possible reason can be found in another context. Tran et al. observed the same effect in their organic based stack, where the stack was Co (8 nm)/AlO_x (2 nm)/C_{60} (t = 0-7 nm)/NiFe (15 nm) [22]. To compare our data with theirs, we normalized the bias dependent MR curves of our junction and showed them together in Figure 4.18, where the data in Figure 4.18a and in Figure 4.18b represent the our study and Ref. [22], respectively. One should note that the both figures are in different bias scales. Furthermore, polarity of applied bias was reversed in both cases, where the electrons

are injected from CoFeB/MgO interface at positive bias in Figure 4.18a while the electrons are injected from C_{60}/NiFe interface at positive bias in Figure 4.18b. In both figures, a general trend is that the MR curves decay faster with increasing organic thickness. Tran et al. explained that when the electrons occupy an intermediate state in the thick organic films, inhomogeneous magnetic fields which arise from the finite roughness of the top ferromagnetic layer causes spin precession at the intermediate sites.

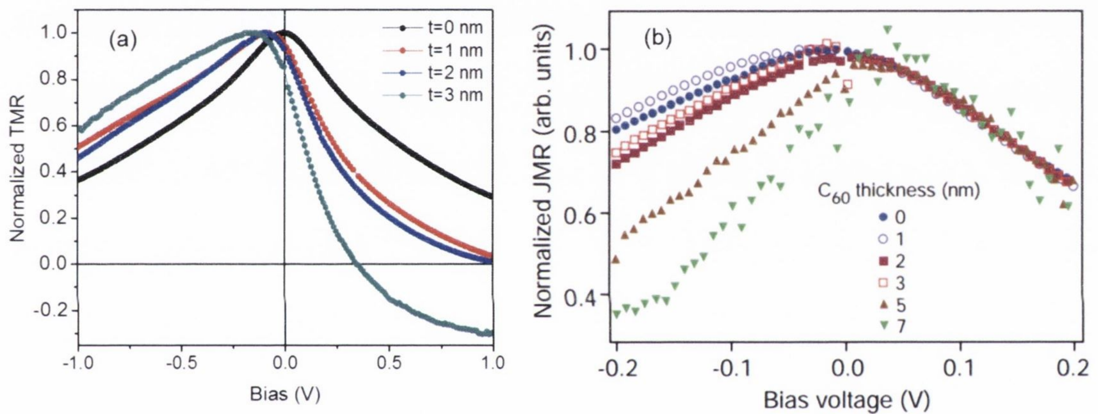

Figure 4.18. Comparison of the normalized bias dependent TMR curves, where the data is taken from our study (a) and Ref. [22] (b). Note that the polarity of the applied bias in both figures is reversed and the bias scales are different.

In order to better understand the mechanism, Figure 4.19 can be considered which shows the schematic representation of two-step tunneling via a Gaussian DOS of intermediate sites for the thicker organic films. If a potential difference is created between the electrodes, the potential within the organic layer is tilted so that the spatial distribution of the DOS of the intermediate sites align with Fermi level of the

electrodes, resulting in shifting the position of Gaussian DOS. Thus, the direction of the shifting depends on the polarity of bias, where applying a negative bias to the bottom electrode expels the intermediate states to the top organic/ferromagnet interface. The top organic/ferromagnetic interface is expected to be rougher than the oxide/organic interface. Then, if the multistep tunneling occurs via those intermediate sites which are shifted towards the organic/ferromagnet interface, the inhomogeneous magnetostatic fields arising from the finite roughness of the organic/ferromagnet interface causes the electron spin precession during the occupation of those intermediate sites in the multi-step tunneling process, resulting in a faster decay in the negative bias. In the opposite case, the Gaussian DOS of the intermediate sites shift towards the bottom AlO_x/organic interface which is far from the rough interface in which the inhomogeneous magnetostatic fields are generated. In this case, electron spin is effected less from the inhomogeneous magnetostatic fields. For the thick organic films, the number of tunnel steps increases and spin precession occurs in each multi-step tunneling event. This model explains well the reason of faster decay of the bias dependent TMR curve for thick organic thickness when the multi-step is considered. However, the RA increases linearly in the exponential scale with organic thickness up to 3 nm in Figure 4.15, suggesting that the transport mechanism is governed by direct tunneling. Therefore, we do not expect a multi-step tunneling in our junctions even though the bias dependent MR curves have the same behaviour in Figure 4.18.

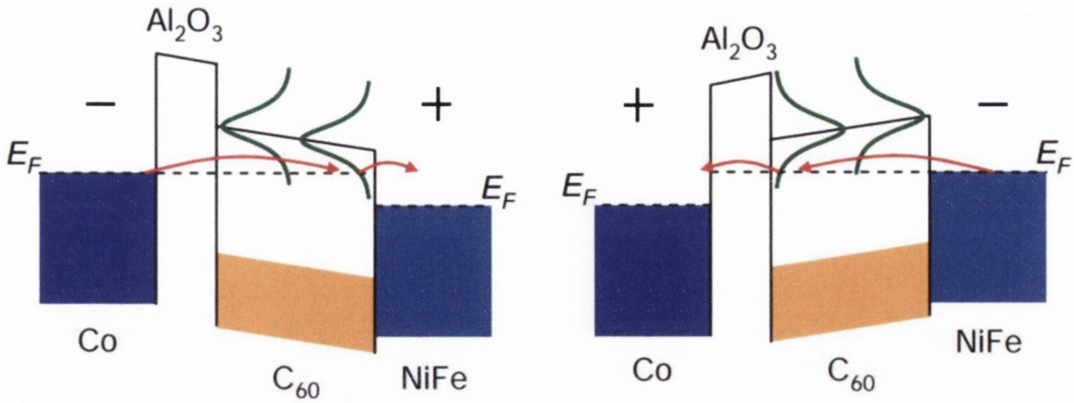

Figure 4.19. Two-step tunneling and spatial distribution of Gaussian DOS of the intermediate sites under an applied bias with different electrical polarity [22].

4.3.3 Magnetoresistive characteristics of $AlO_x/Alq_3/AlO_x$ based hybrid devices prepared by using in-situ shadow masking

4.3.3.1 Sample preparation

Shadow masking is the most commonly used method for the fabrication of organic based devices as it does not involve any wet processing steps. The sample preparation is the same with the section 4.2.1, where the preparation of reference stack, CoFe (10 nm)/AlO_x (3 nm)/CoFe (18 nm), is explained in detail. In this section, we divided the AlO_x into two portions of 1.5 nm AlO_x and inserted the organic layer between these two AlO_x barriers, where the final stack becomes CoFe (10 nm)/AlO_x (1.5 nm)/Alq_3 (*t*)/AlO_x (1.5 nm)/CoFe (18 nm). The shadow masking technique allows us to produce 6 junctions in each batch without breaking vacuum, and the all junctions have the same size, 250x250 μm^2.

4.3.3.2 Results

The devices prepared using shadow masking showed no MR at room temperature when the thickness of the Alq_3 layer was greater than 1 nm, where the barrier is AlO_x (1.5nm)/Alq_3(t=0-20 nm)/AlO_x(1.5 nm). For the comparison, when t=0 nm the device showed 12 % MR at 300 K and 28 % MR at 20 K (see Figure 4.4). Figure 4.20 shows MR and I-V characteristics of the device as a function of temperature when t=1 nm. Introducing 1 nm Alq_3 layer reduced the MR to 2 % at 300 K. The MR increased with decreasing temperature and reached the maximum 17 % at 17 K.

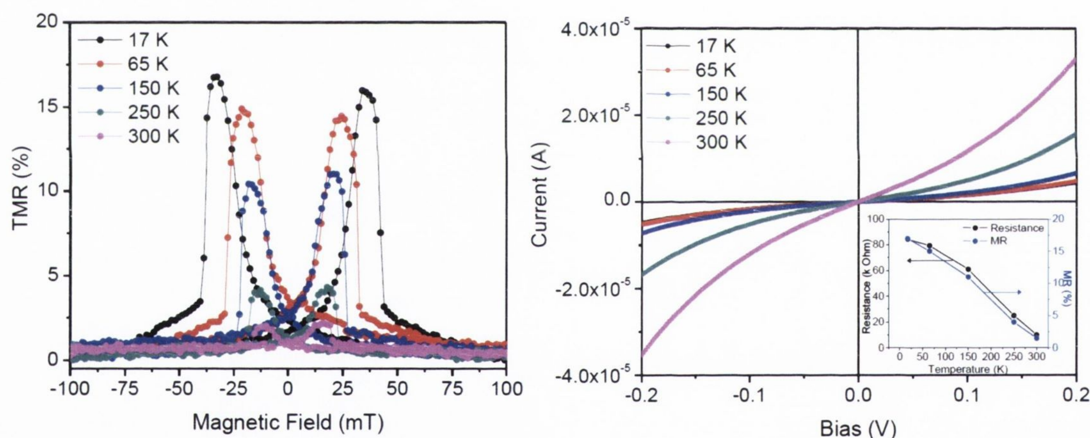

Figure 4.20. MR (a) and I-V (b) curves of the device as a function of temperature when t=1 nm. The inset shows the variation of junction resistance and MR as a function of temperature.

The I-V curve of the device showed a strong temperature dependence and the resistance of the device increased nearly by a factor of 80 with decreasing temperature. However, in the case of direct tunneling (see Figure 4.15), the device resistance was almost independent of temperature, increasing by less than 15 %. Therefore, we can deduce

that another transport mechanism dominates the device current in here. The total barrier thickness increases in the presence of the organic layer and conduction seems to be dominated by either multi-step tunneling or superposition of both multi-step and direct tunneling [23].

For the greater thicknesses $t > 1$ nm, the MR signal completely disappeared at 300 K but a few percent MR was observed at low temperature range for $t = 2$ and 3 nm. Figure 4.21 shows the MR and I-V characteristics of the device when $t = 2$ nm. The device showed maximum ~ 10 % MR at 15 K and the MR vanished when the temperature was around 65 K, where the MR data was in the noise level above the 65 K. The I-V curve of the device showed a strong temperature dependence and the resistance of the device increased nearly two orders of magnitude with decreasing temperature.

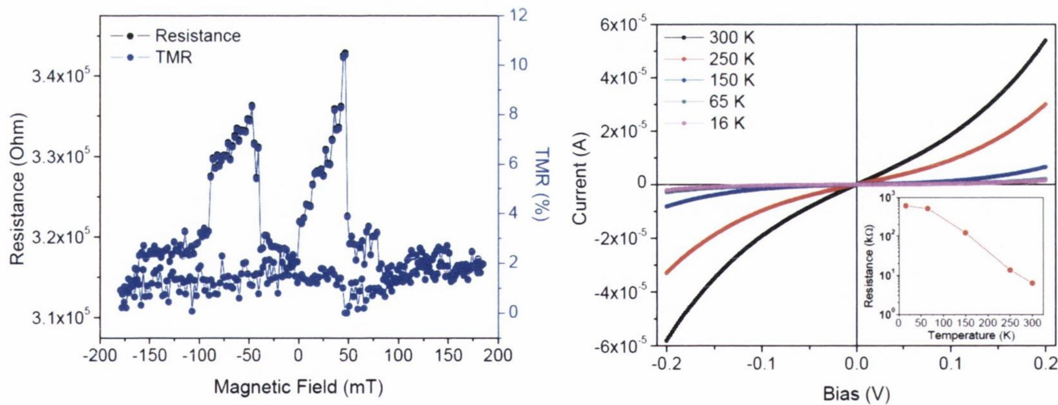

Figure 4.21. MR and I-V characteristics of the device when $t = 2$ nm. The MR data was measured at 15 K and the inset figure shows the variation of device resistance as a function of temperature.

Figure 4.22 shows the MR, I-V and dI/dV characteristics of the device when $t = 3$ nm. Still there was a clear sign of MR when $t = 3$ nm at least up to the 65 K. The device

showed ~ 7% and ~ 4% MR at 15 K and 65 K, respectively. Also, the I-V curve showed a strong temperature dependency and the resistance of the device increased nearly 2 orders of magnitude with decreasing temperature, reflecting a multi-step tunneling process. Furthermore, as was pointed out in the literature, the absence of the zero bias anomaly in the dI/dV curve can be an indication about the barrier quality [21]. The dI/dV characteristic of the device was extracted from the I-V curve measured at 15 K and showed no zero bias dip, indicating a good $AlO_x/Alq_3/AlO_x$ hybrid barrier.

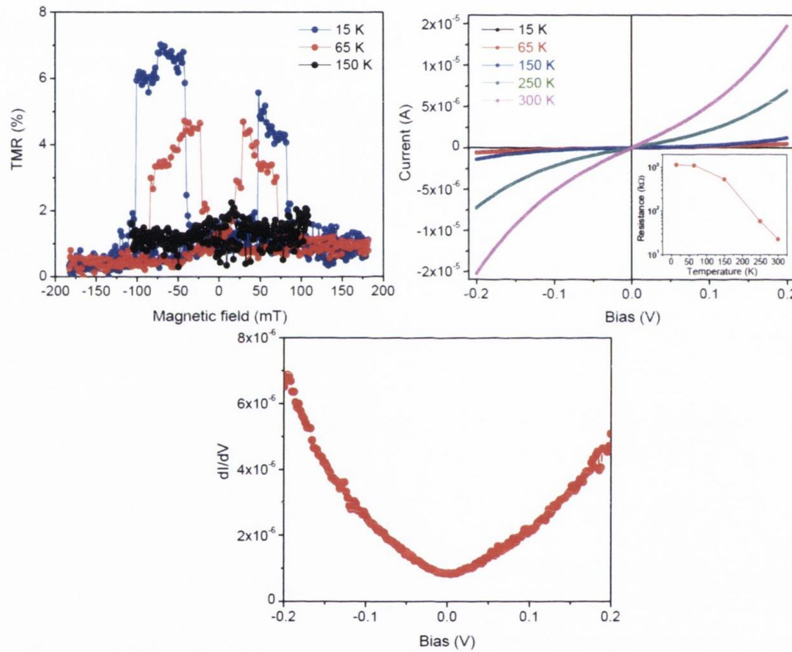

Figure 4.22. MR, I-V and dI/dV characteristics of the device when t=3 nm. The inset shows the variation of device resistance with temperature.

When $t > 3$ nm, we could not observe any sign of MR at any temperature. The remarkable observation was that the device resistance changed with temperature by nearly two orders of magnitude when the organic layer was inserted between the AlO_x

barriers, indicating that the direct tunneling is not the dominant transport mechanism. A multi-step tunneling or superposition of both multistep tunneling and direct tunneling through the Alq_3 layer may govern the transport. We should note that carrier injection process may also play an important role in determining the temperature dependence of the device resistance. At low bias, electrons tunnel through the defect states via multi-step tunneling or hopping in the organic spacer and device current can be manipulated via electric field or thermionic emission. When the temperature goes down, the thermionic emission and hopping mechanism control the device current, which results in strong temperature dependent current [24]. However, we expect that carrier injection is not a problem in our junctions due to the AlO_x barrier at both interfaces, which increases the carrier injection efficiency at organic/metal interface. All these data clearly show that organic layer acts as a good barrier within the device, and also that it changes significantly the MR and device resistance.

The device resistance increased with increasing Alq_3 thickness at 300 K. When the thickness of the Alq_3 layer exceeded the tunnelling thickness, the incremental resistance levels off, which is the expected behaviour for organic based spin valves and it is related to the multi-step tunneling or hopping via the intermediate sites within the Alq_3 layer Figure 4.23 [22,23]. The figure compares the our data and a literature data taken from Ref. [23]. In Ref. [23], the device resistance behaves differently in three different characteristic regimes with respect to Alq_3 thickness; direct tunneling regime, onset of two step tunneling regime and multi-step tunneling regime. The solid or dashed black curves in (b) represent the theoretical model in [23].

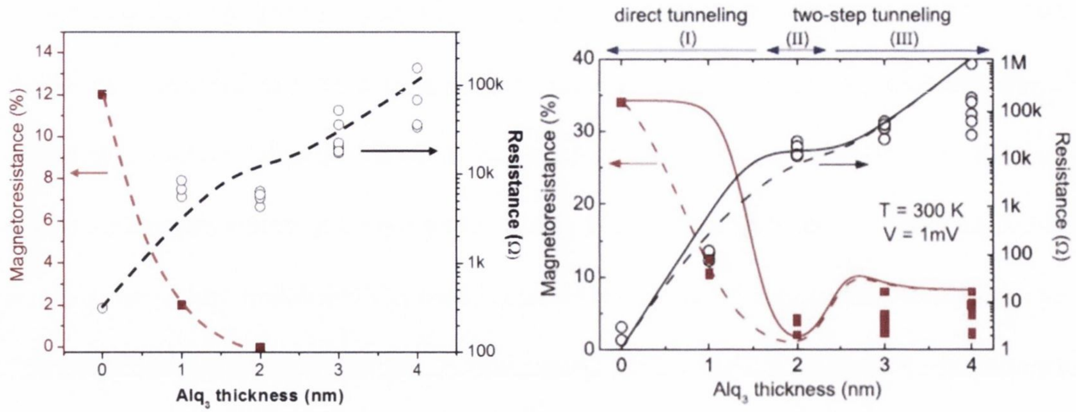

Figure 4.23. Thickness dependent resistance of organic devices, where the data in (a) represent our study while the data in (b) is taken from Ref. [23]. The dashed line in (a) is an eyes-to-guide plot. The stack in (b) is Ta (2)/CoFeB (2)/AlO_x (~ 1.5)/Alq_3 (t)/Co (20), where the numbers in parentheses are the layer thicknesses in nanometre. The junction size in (a) and (b) is 250x250 μm^2 and 300x300 μm^2, respectively.

As expected for direct tunneling, the device resistance increases linearly on a logarithmic scale in the direct tunneling regime for the both graphs and the slope levels and then drop at the onset of the two-step tunneling regime. For the greater Alq_3 thicknesses, the device resistance increases with a lover slope than the slope which is in the direct tunneling regime. Our data shows the same behaviour as the Ref. [23] and the mechanism behind this behaviour is shown in Figure 4.24. Depending on the organic thickness, the device current can be dominated by direct or two-step tunneling. If the thickness of the organic layer is in the tunneling regime, electrons tunnel through the barrier and the tunnel current density becomes proportional to the exp[$-\kappa d$], where $\kappa = 2[(2mU)^{0.5}]/\hbar$ and d is the thickness of the organic barrier, leading to a linear increment of current with increasing barrier thickness on a logarithmic scale. If the barrier thickness is beyond the tunnelling regime, an intermediate energy site located at d_1 within the organic layer assists to the injected electrons to reach the other side of the

barrier, results in two-step tunneling. In this case, the extinction of the wave function is proportional to the $\exp[\kappa(d-d_1)]$. In the case of maximum transmission, the exponential term becomes $\exp[\kappa(d/2)]$, where $d_1 \approx d/2$. This means that the total resistance increases with half of the slope of the resistance level in the direct tunneling regime. For greater thicknesses, the resistance level continues to increase with a lower slope governed by the reduction of the tunnel thickness between the two intermediate sites. So, the question is, how does this process affect the spin polarized transport in the organic layers? Figure 4.23b compares the variation of MR with respect to transport mechanisms. It can be clearly seen that the MR drops abruptly if the multi-step tunneling dominate the transport mechanism. The multi-step tunneling process is considered one of the spin relaxation mechanisms, resulting in to reduce MR in organic semiconductors. In the multi-step tunneling process, an electron occupies a localized molecular site in the organic barrier before tunnelling from one site to another. This occupation is relatively long and the spin of electron can be influenced by the randomly oriented local hyperfine fields. As a result, the spin precession in the presence of hyperfine field in those intermediate sites within the organic layer may be considered as a main spin scattering mechanism as reported in Ref. [23].

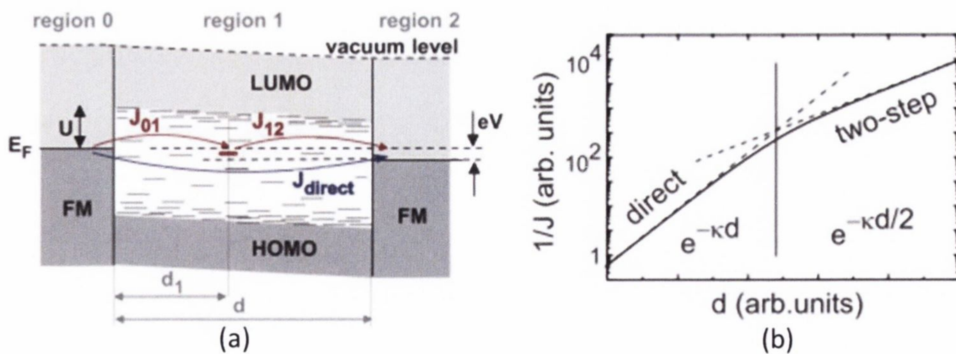

Figure 4.24. Schematic band diagram ferromagnet/Alq_3/ferromagnet structure (a) and inverse current density as a function of Alq_3 thickness (b) [23].

Our results indicate that spin polarized transport is diminished in the presence of Alq_3 layer. In the direct tunneling process, electrons lose spin polarisation in some extent but still it is possible to see a remarkable room temperature MR in the organic based devices, meaning that organic layer certainly allows the spin polarized tunneling. However, when two-step or multi-step tunneling processes play a significant role, the electrons lose a great amount of spin polarization when they occupy the molecular sites, leading to loss of MR in the organic based devices. The small magnitude of the MR in the thick organic layer might be related to some other important spin scattering mechanisms. First of all, for the thick organic barriers the number of intermediate sites will increase, resulting in different tunnelling thicknesses and different tunneling rates between the molecular sites in the organic spacer. If the numbers of incoming and outgoing spins are different for an intermediate site, the polarization of the spin current might be destroyed due to spin accumulation. Besides this, the occupation time of the intermediate sites by an electron might be much higher than the spin relaxation time so the electrons may lose their spin orientation before they reach the FM electrode. Furthermore, another mechanism that may affect the spin polarization in the intermediate site was proposed by Tran *et al.* who believe that orange peel coupling arises from the interface roughness causes the spin precession in the intermediate sites [22].

4.4 CuPc based hybrid organic devices

4.4.1 Magnetoresistive characteristics of MgO/CuPc based hybrid devices prepared using UV lithography

4.4.1.1 Sample preparation

The stack which we used for CuPc is almost the same with the cleaned MgO/Alq_3 based stack, where the bottom CoFeB layer was pinned by making an artificial antiferromagnet. This type of structure is suggested to prevent the boron diffusion into IrMn layer during the annealing process because boron can modify the [111] orientation of IrMn, reducing the strength of exchange bias. The bottom stack with MgO (2 nm) barrier was prepared in Shamrock tool and transferred to the annealing furnace by vacuum breaking. Here, the sample was annealed at 350 °C during 1 hour with a field of 800 mT. Then, it was transferred to bell jar system for CuPc deposition (0, 1 and 2 nm). After that, the sample was transferred to Shamrock breaking the vacuum again and the stack was completed by depositing CoFe (3 nm) layer and capping layers of Ta (5 nm)/Ru (5 nm) by sputtering. Figure 4.25 shows the evolution of MgO/CuPc based stacks.

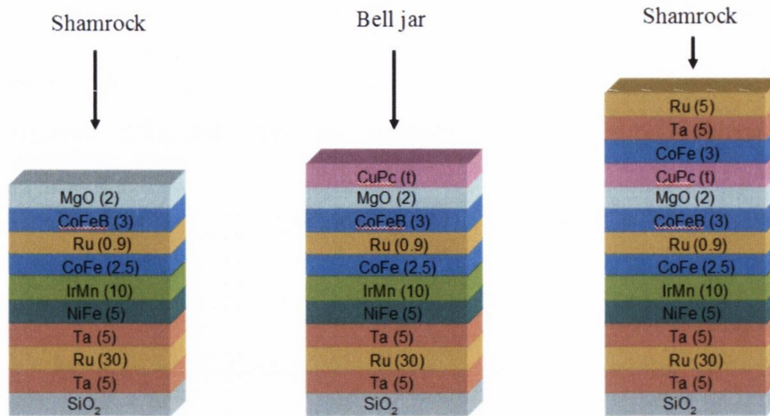

Figure 4.25. Evolution of MgO/CuPc based MTJ stacks.

4.4.1.2 Results

In this section we present the TMR characteristics of the two sets of data for the comparison. The both samples were prepared in the same experimental conditions. Figure 4.26a and b show the TMR characteristics of the first set of MgO/CuPc based MTJs at 300 K and 50 K, respectively. Here, the junction sizes are 50x150 μm^2. The data showed that TMR depends on the thickness of the CuPc layer as well as temperature. At room temperature, inserting 1 nm CuPc layer between MgO and CoFe layer destroyed nearly 10% MR in the tunnelling regime. The further increase of the thickness of CuPc layer (t = 2 nm) caused to lose another 7 % MR. The MR showed a faster decay with increasing temperature in the presence of thick CuPc.

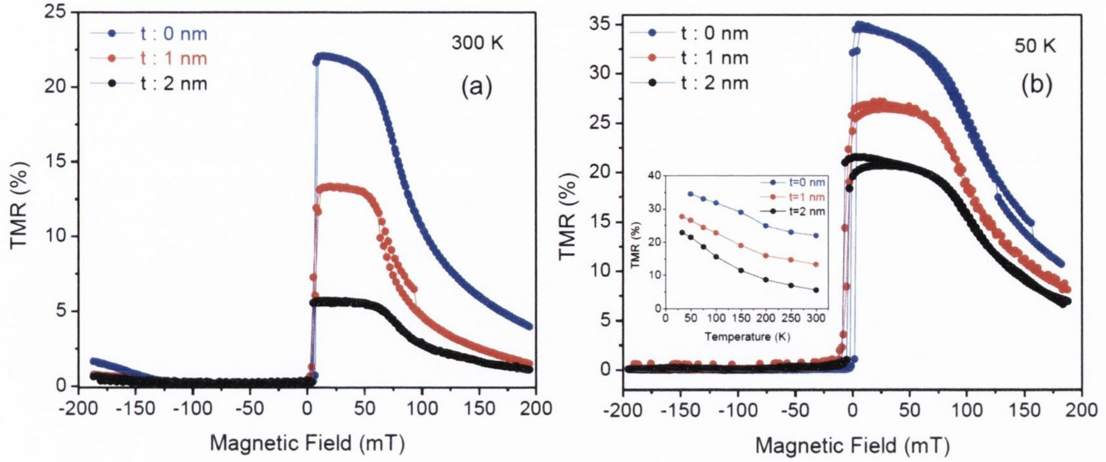

Figure 4.26. TMR characteristics of the first set of sample at 300 K (a) and at 50 K (b). The inset in (b) shows the variation of TMR with temperature for all samples.

Figure 4.27 shows the temperature device resistance as a function of temperature. When t = 1 nm, the resistance was nearly independent of temperature as expected for the direct tunnelling. However, when t = 2 nm, resistance changes nearly by a factor of 2 over the temperature range, which is typical for semiconductor barriers. RA versus the square root of area of the MgO (2 nm)/CuPc (0 nm) samples is plotted in Figure 4.27. RA changes with area, unlike the second set where RA was nearly constant. We attribute this difference to a non-uniform barrier in the first set of samples. The stack was exposed to air after depositing of organic layer and the FFTM studies showed that bottom ferromagnetic layer can be oxidized through the organic layer. Here, we expect that the quality of MgO barrier may change in each vacuum breaking even in the presence of CuPc layer. Furthermore, there is an open question to what extent the organic layer is contaminated by ferromagnetic metal when the top electrode was deposited by sputtering.

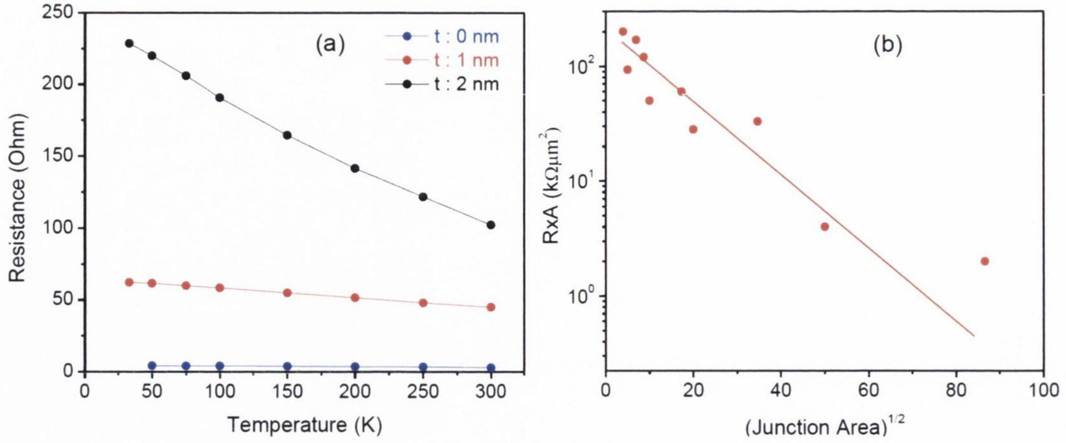

Figure 4.27. Temperature dependent resistance behavior of the first set of sample (a) and RA product versus square root of area plot (b).

The TMR characteristics of the second set of CuPc based junctions are shown in Figure 4.28a and Figure 4.28b. Here, the junction sizes are 10x10 μm^2 and 50x50 μm^2 for the MgO(2nm)/CuPc(2nm) and MgO(2nm)/CuPc(0nm) samples, respectively. In this set, the MR values are bigger than for the first set and the RA is approximately 1 $M\Omega\mu m^2$ for t = 0 nm, regardless of junction area. There is still a reduction of the MR nearly 10% at 300 K, when 2 nm CuPc is inserted between MgO and CoFe. One can compare these results with Ref. [25], where the stack is Fe/CuPc (~ 100 nm)/Co and there is no MR at 300 K.

Organic materials exhibit different growth characteristics with respect to inorganic counterparts due do the some specific issues. For example, they have orientational degrees of freedom which makes a transition from lying-down to standing-up configuration (or vice versa) during the film growth. Also, the substrate roughness plays an important role for the molecular orientation which affects the adsorption growth geometry. In the case of CuPc, if the substrate roughness is larger than the molecular size, a standing-up geometry becomes favourable due to the weak substrate-

molecule interaction. On the other hand, CuPc has a lying-down geometry for atomically flat substrates. Moreover the molecular orientation of the CuPc is effected by inertness of the substrate. For the thicker films, CuPc molecules tend to grow in a standing-up configuration. In general, surface of the oxide substrates are charge balanced and relatively inert, which makes them favourable for growth studies. Therefore, the thickness dependent resistance and MR may be originated from the molecular orientation of the CuPc barrier in MgO/CuPc based hybrid organic devices. Also, the initial disorder in the first a few monolayer may affect the device electronic properties.

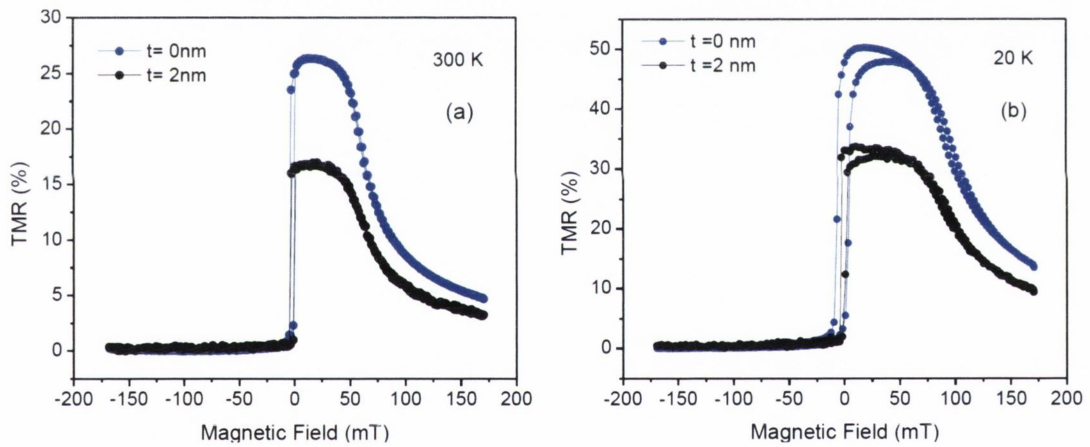

Figure 4.28. MR characteristics of the second set of samples at 300 K (a) and at 20 K (b).

4.4.2 Magnetoresistive characteristics of AlO_x/CuPc/AlO_x based hybrid devices prepared by in situ shadow masking

4.4.2.1 Sample preparation

In this section, device fabrication process for CuPc based junctions is the same as the one described in section 4.2.1. The CuPc layer was deposited in various thicknesses in between the AlO_x layers, within the stack: CoFe (10 nm)/AlO_x (1.5 nm)/CuPc (t)/ AlO_x (1.5 nm)/CoFe (18 nm). Here, we present the data when t = 1 and 2 nm. The junction area is 100 x 100 μm^2. We could not get a reproducible result for the other thicknesses.

4.4.2.2 Results

Figure 4.29 shows MR, I-V and dI/dV characteristics of the device when t=1 nm. The device showed maximum ~ 16 % of MR at 18 K, then, further increase in temperature decreased the MR and the MR signal became in the noise level above 175 K (see the inset in Figure 4.29b). Furthermore, the I-V characteristic of the device showed a strong temperature dependency and the resistance increased nearly by a factor of 50. The strong temperature dependency of the device indicates that the transport mechanism is not only the direct tunneling. The two-step tunneling process or a parallel channel of two-step tunneling and direct tunneling may govern the transport mechanism. The dI/dV data was calculated from the I-V curve of the device measured at 18 K and

showed a nice parabolic behaviour, reflecting a good barrier between the ferromagnetic layers.

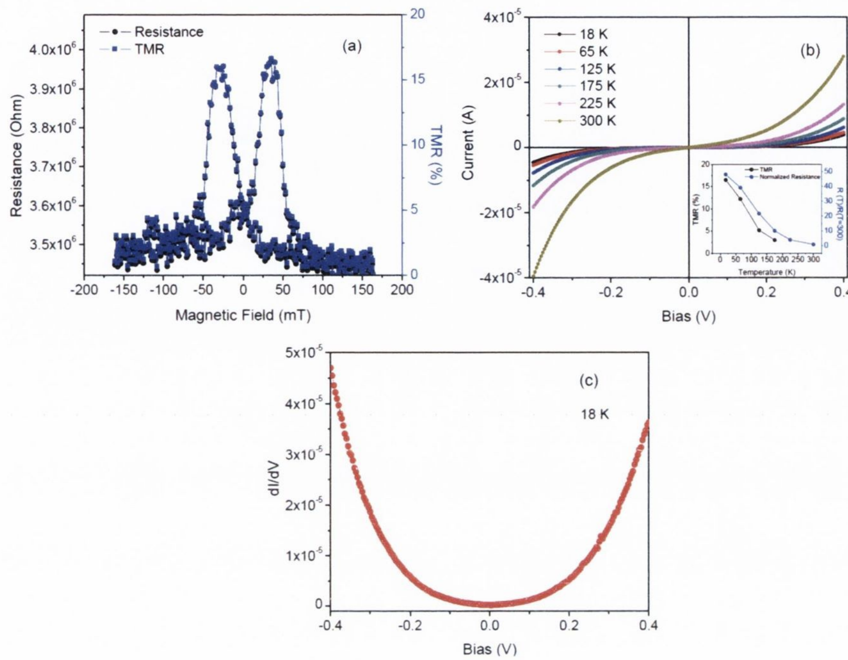

Figure 4.29. TMR characteristic at 18 K (a) and the temperature dependent I-V characteristics (b) of CuPc based device when t=1 nm. The dI/dV curve was calculated from the I-V data measured at 18 K (c). The inset in figure (b) shows the variation of MR and resistance as a function of temperature.

For t = 2 nm, MR, I-V and dI/dV characteristics of the device are shown in Figure 4.30. We could not observe any sign of magnetoresistance at 300 K or at 17 K. The device showed a strong temperature dependent I-V characteristic and device resistance increased by a factor of ~ 90 with decreasing temperature, where the resistance was 67 kΩ at 300 K and 6034 kΩ at 17 K. The device did not survive for a long time at 17 K so the I-V and MR characteristics of the device could be measured only at 17 K and 300 K. The strong temperature dependency of the device resistance rules out any pinholes or short circuits in the barrier. Also, dI/dV curve showed a nice parabolic behaviour at 17 K. These results can be compared with the characteristics of 1 nm thick CuPc based

device. For t = 2 nm, more than one intermediate sites may assist to the hole transport and holes may lose their spin polarisation in multi-step tunneling process. Furthermore, MR decreased faster than the Alq_3 based devices, indicating another spin scattering mechanism. Here, ions may be the source of spin chattering mechanism. The results indicate that MR depends on the thickness of the CuPc layer as well as temperature and we infer that multi-step tunneling and paramagnetic Cu^{2+} ions in CuPc diminished the spin polarized transport in CuPc layer.

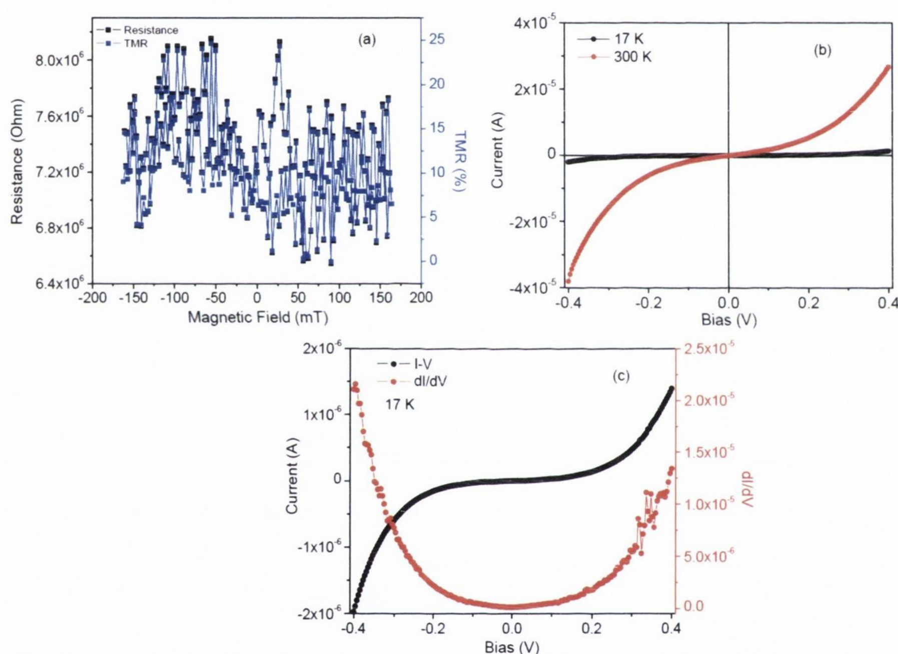

Figure 4.30. MR (a), I-V (b) and dI/dV (c) characteristics of 2 nm thick CuPc based device, where the MR curve was measured at 17 K.

4.5 Magnetoresistive characteristics of $AlO_x/ZnPc/AlO_x$ based hybrid devices prepared by in situ shadow masking

In this section, magnetoresistive characteristics of ZnPc based hybrid devices were studied as a function of temperature and layer thickness to compare the results with the CuPc based devices. The samples were prepared by shadow masking. We want to see the effect of central metal ion in the PC molecule in terms of the spin transport properties. In contrast to the CuPc molecule, there are no paramagnetic scattering centres in ZnPc. Therefore, it would be a nice point to compare the MR and I-V characteristics of these two molecules. Here, we describe the successful structuring of ZnPc based hybrid devices in various layer thicknesses (t=1, 3, 5 and 10 nm), where the junction size is 100x100 μm^2 and the stack is CoFe (10 nm)/AlO_x (1.5 mn)/ZnPc (t)/AlO_x (1.5 nm)/CoFe (18 nm)

Figure 4.31 shows the MR, I-V and dI/dV characteristics of the ZnPc based device when t=1 nm. The device showed maximum ~ 18% of MR at 15 K, which is slightly larger than the MR measured for CuPc. Then, the MR decreased with increasing temperature and there was a clear sign of MR up to 225 K (~ 2%). However, the MR disappeared completely at 300 K. These results can be compared with the results obtained for CuPc based junctions, where the MR decreased faster in the case of CuPc. Furthermore, the device showed a temperature dependent I-V characteristic and the resistance of the device increased nearly by a factor of 12 with decreasing temperature, where the device resistance is 224 kΩ for 300 K and 2671 kΩ for 15 K. The dI/dV curve was calculated from the I-V measured at 15 K and a nice parabolic behaviour was observed, indicating a good barrier.

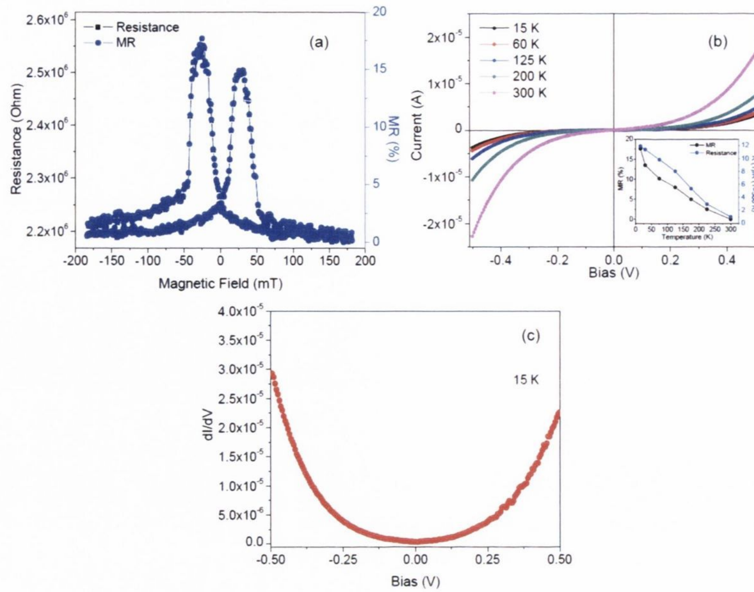

Figure 4.31. MR (a), I-V (b) and dI/dV (c) characteristics of 1 nm thick ZnPc based device, where the MR curve was measured at 15 K. The inset in figure (c) shows the MR and normalized resistance of the device as a function of temperature.

For t = 3 nm, we could not observed a clear sign of MR at 15 K (see Figure 4.32). The R-H curve fluctuates too much and the MR may become within the noise level or MR completely disappeared due to the multi-step tunneling. In the case of 3 nm thick ZnPc layer, the total barrier thickness becomes 6 nm and we do not expect the direct tunneling for this thickness. The I-V curve showed a strong temperature dependence and the device resistance increased nearly by a factor of 25 with decreasing temperature, where the resistance of the device was calculated from the fitting the I-V cure around the zero bias. The dI/dV curve still preserved the parabolic behaviour with a little noise. A large fraction of the noise is due to the current fluctuations produced by the Keithley sourcemeter.

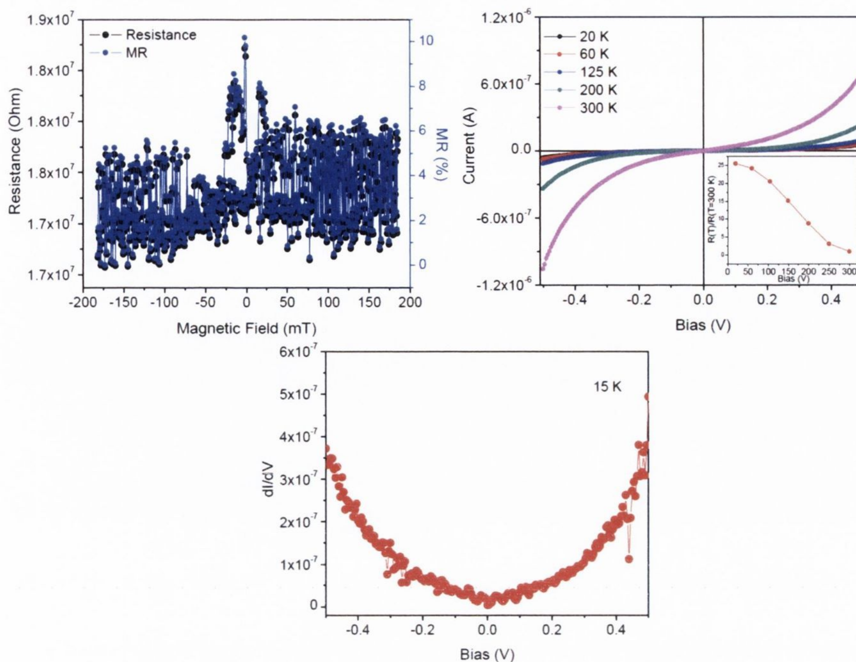

Figure 4.32. MR (a), I-V (b) and dI/dV (c) characteristics of 3 nm thick ZnPc based device, where the MR curve was measured at 15 K. The inset in (c) shows the normalized resistance of the device as a function of temperature.

For the thick ZnPc layer (t = 5 or 10 nm), we could not observe any sign of MR in all temperature range and in different biases up to 1 V. On the other hand, device resistance increased exponentially with increasing ZnPc thickness and tended to saturate for the thick ZnPc layers (see Figure 4.33). This behaviour is generally observed in organic semiconductor devices when the multi-step tunneling via intermediate sites becomes the dominant mechanism instead of instead of direct tunneling between the electrodes. In this point, we can infer that the lack of MR in thick ZnPc based organic hybrid devices is due to the multi-step tunneling.

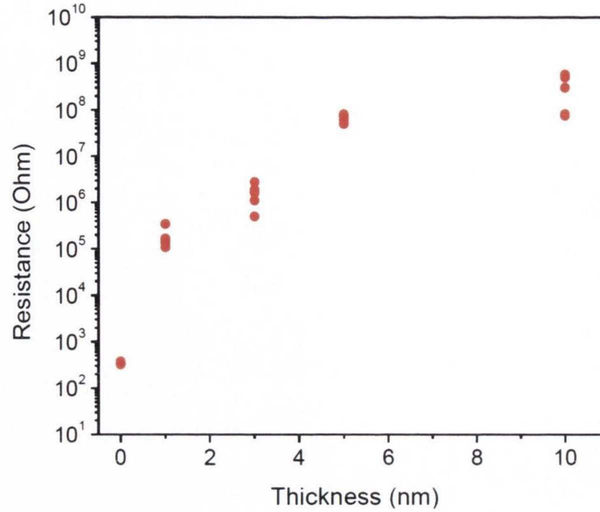

Figure 4.33. Resistance of a set of junctions with increasing ZnPc thickness.

4.6 Znq_2 based hybrid organic devices

4.6.1 Magnetoresistive characteristics of MgO/Znq_2 based hybrid devices prepared using UV lithography

4.6.1.1 Sample preparation

The stacks which we used for Znq_2 based MTJs are nearly the same with CuPc based MTJ stacks except for the top ferromagnetic electrode. The bottom stacks were prepared in Shamrock tool and transferred to annealing furnace. After the same annealing process like CuPc, the samples were then transferred to organic evaporator to deposit organic layer and Co electrode. After that, samples were transferred to Shamrock tool. Here, top surface of the Co layer was cleaned with Ar ion etching for 2 minutes to remove any oxide layer from the surface and the process was finished by adding Ta (5 nm) and Ru (5 nm) capping layers. In the final step, the samples were

patterned into micron-size junctions. Figure 4.34 shows the evolution of Znq_2 based stack.

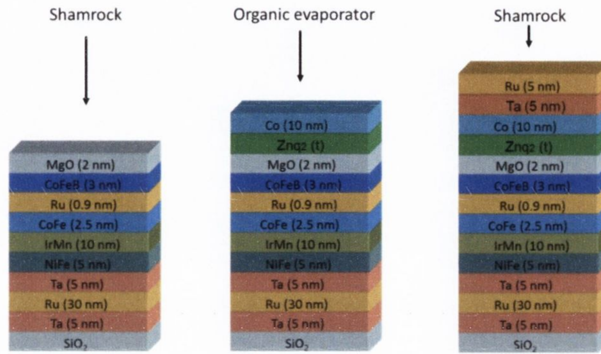

Figure 4.34. Evolution of MgO/Znq_2 based MTJ stacks.

4.6.1.2 Results

Figure 4.35a shows the TMR characteristics of the Znq_2 based MTJs. Here, the junctions have the same sizes and it is 20x20 μm^2. The TMR ratio remained almost constant even when t=2 nm, and it was ~ 15 % at room temperature. Figure 4.35b shows the resistance area product vs. temperature plot of Znq_2 based junctions. When t =1 nm, RA was nearly flat and the same in the case of t=0 nm, indicating that 1 nm Znq_2 did not form as a good barrier in this sample. However, when t=2 nm, the RA increased rapidly with Znq_2 thickness and it changed slightly with temperature, reflecting a nature of semiconductor tunnel barrier. It is obvious that electrons keep their spin polarization while they are tunnel across the organic barrier.

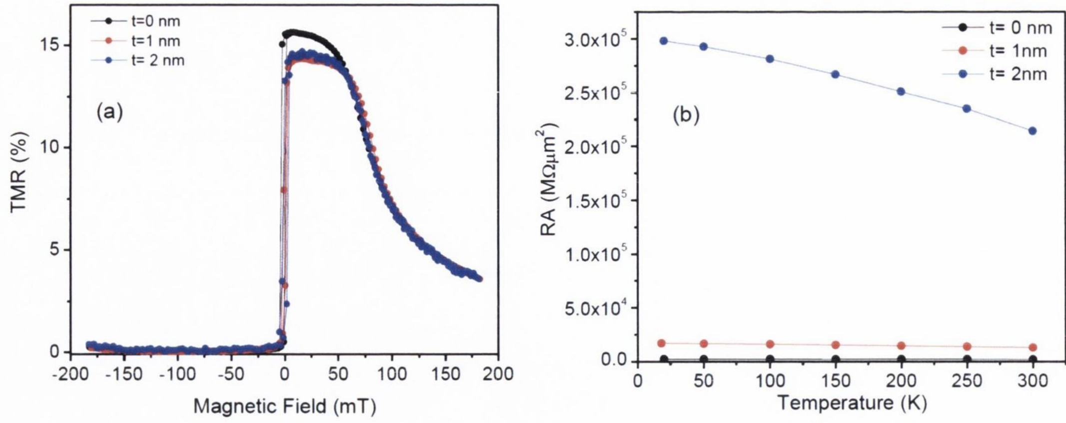

Figure 4.35. TMR characteristics of MgO (2 nm)/Znq_2 (t) based MTJs (a) and variation of RA as a function of temperature (b).

The interesting point is that we observed a sign chance of TMR in the positive bias like Alq_3 based samples. As it was explained in section 4.3.1.2, air exposed MgO and organic/ferromagnet interface play an important role for the sign change of TMR. Figure 4.36 shows the bias dependent TMR curve of the Znq_2 based junctions.

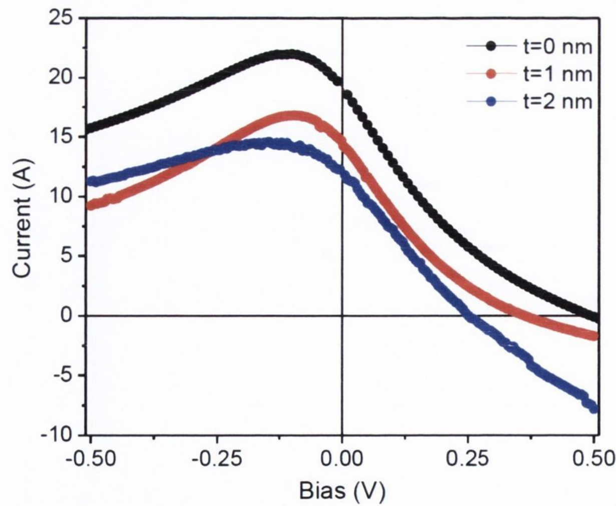

Figure 4.36. Bias dependent TMR curves of MgO (2 nm)/ Znq2 (t) based junctions.

4.6.2 Magnetoresistive characteristics of $AlO_x/Znq_2/AlO_x$ based hybrid devices prepared by using in-situ shadow masking

4.6.2.1 Sample preparation

In this section, we investigate the magnetotransport properties of Znq_2 based devices prepared using shadow masking. The sample preparation process is the same with the previous sections, where the stacks were prepared in organic UHV chamber without breaking vacuum. The stack was CoFe (10 nm)/AlO_x (1.5 nm)/Znq_2 (t)/AlO_x (1.5 nm)/CoFe (18 nm), where t = 1, 2, 10 nm. The junction size for all samples is 100x100 μm^2.

4.6.2.2 Results

Figure 4.37 shows the MR and I-V characteristics of Znq_2 based device when t=1 nm. The device showed maximum ~ 23 % of MR at 20 K and the MR decreased with increasing temperature and vanished above 225 K (see the inset in Figure 4.37b). Furthermore, the I-V characteristic of the device was strongly temperature dependent and the device resistance increased nearly by a factor of 20 with decreasing temperature.

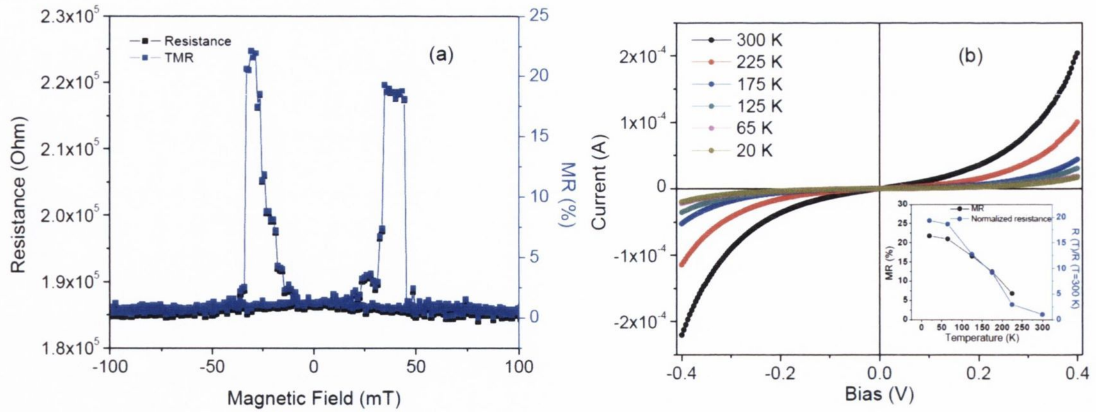

Figure 4.37. MR (a) and I-V (b) characteristics of Znq_2 based device when t=1 nm, where the MR curve in (a) was measured at 20 K.

For the greater thicknesses (t > 1), we could not get nice junctions which were stable against the electrical measurements. For t=2 nm, we could only manage to measure a few MR curve at 18 K for 50 mV and 100 mV. In both biases, we could not observe any sign of MR. Figure 4.38 shows the MR curves of the device for t=2 nm at different biases.

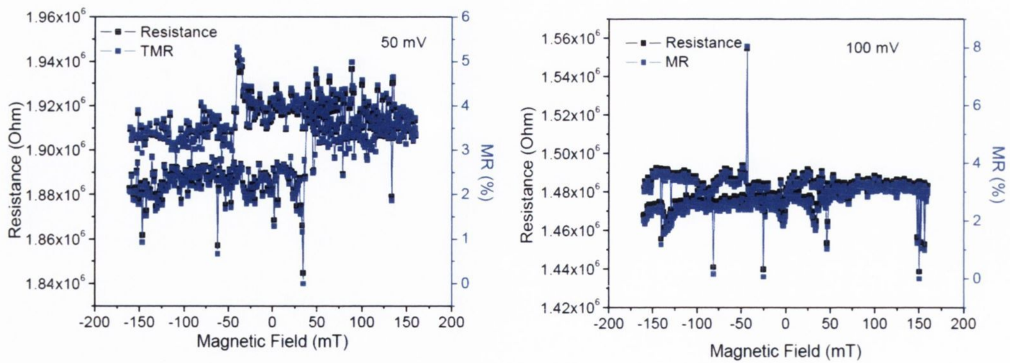

Figure 4.38. MR curves of Znq_2 based device when t=2 nm at 18 K for 50 mV (a) and 100 mV (b).

As a last step, we present some data for t=10 nm. The I-V and MR curves of this device were measured successfully at low temperatures. The results showed that there was no MR at 5 K and the I-V characteristic was strongly temperature dependent. Figure 4.39 shows the MR and I-V characteristics of the device when t=10 nm.

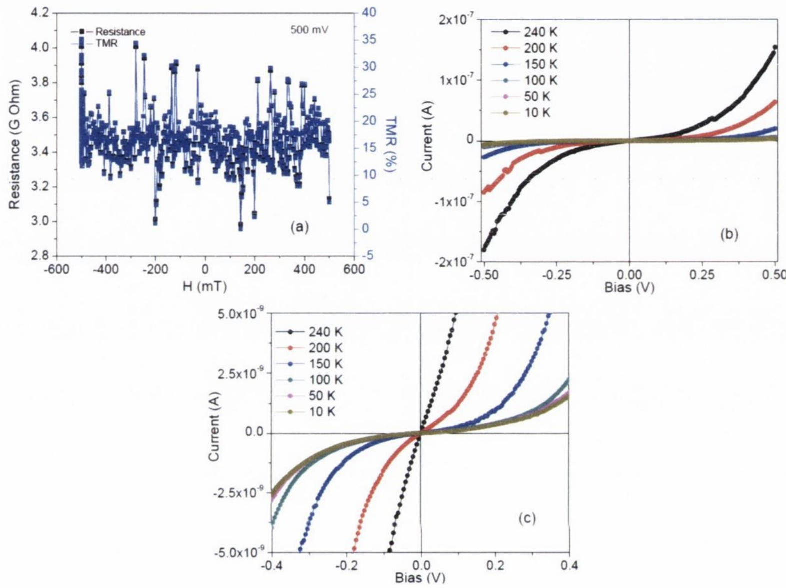

Figure 4.39. MR (a) and I-V (b) characteristics of Znq_2 based device when t=10 nm, where R-H curve was measured at 18 K applying 500 mV. Also, a zoom in view of the I-V curve is shown in (c).

In this thesis, we present some new approaches for the device fabrication process. First of all, we suggest to use an exchange-biased stack with an MgO spin filter and to develop a photo lithography patterning process. This kind of stack presents very high room-temperature magnetoresistance which is a desired parameter for organic spin valves. In addition, we suggest to use a thin layer of AlO_x at the both sides of the organic barrier, which improves the interfacial characteristics of the organic/FM structure.

Our transport data suggest that penetration of metal atoms into the organic barrier is only limited by a few nanometres. This is in contrast to the Vinzelberg's data which show ~ 50 nm thick diffusive layer at the Alq_3/Co interface [26]. Moreover, the tunneling thickness of the organic barriers in our study is less than the many of the literature works which shows that the devices present tunneling characteristics across the thick organic barriers (10-50 nm). Furthermore, one of the main differences between our and literature data is that our devices always show positive magnetoresistance which is consistent with the Santos's study. This may be related to the choice of the FM electrodes and sign change of MR is not an intrinsic property of the organic barrier itself. Then, the MR in our devices disappears quickly when the thickness of the organic barrier is in the multi-step tunneling regime which is in contract to the Epstein's [14] and Vardeny's [18] studies. Next, In the case of formation a magnetic dead layer at the organic/FM interface, our data is consistent with the Dediu's [27] and Szulczewski's [28] studies which show that a chemical reaction exists between the organic and ferromagnetic layers.

4.7 Conclusion

In conclusion, we have studied the magnetoresistive response of the Alq_3, CuPc, ZnPc and Znq_2 based organic spin valves prepared by using UV lithography or in-situ shadow masking. The results show that spin polarized tunneling is possible in these organic semiconductors and a remarkable room temperature magnetoresistance can be observed in organic based spin valves. However, the devices did not show any

measurable magnetoresistance at room temperature when the barrier thickness beyond the single-step tunneling regime except for Alq_3 (~ 2 %). At low temperatures, the MR disappeared quickly with increasing organic thickness. The maximum organic thickness which showed a reasonable MR was 3 nm for Alq_3 based junctions. We infer that spin diffusion length in organic semiconductors is a few nm at low temperature range and the multi-step tunneling is the source of spin relaxation mechanism. In the multi-step tunneling process, an electron occupies a localized molecular site in the organic barrier before tunnelling from one site to another. This occupation is relatively long and the spin of electron can be influenced by the randomly oriented local hyperfine fields. As a result, the spin precession in the presence of hyperfine field in those intermediate sites within the organic layer may be considered as a main spin scattering mechanism as reported in the Ref. [23].

4.8 Bibliography

[1] J.S. Moodera, L.R. Kinder, T.M. Wong, R. Meservey, Physical Review Letters 74 (1995) 3273.

[2] W. Dexin, C. Nordman, J.M. Daughton, Z. Qian, J. Fink, Magnetics, IEEE Transactions on 40 (2004) 2269.

[3] O. Song, Y.M. Lee, K. Lee, C.S. Yoon, C.K. Kim, Met. Mater. Int. 9 (2003) 421.

[4] Y.M. Lee, O. Song, C.S. Yoon, C.K. Kim, Y. Ando, H. Kubota, T. Miyazaki, Microelectronics Journal 34 (2003) 805.

[5] H. Meng, J. Wang, Z. Diao, J.-P. Wang, Journal of Applied Physics 97 (2005) 10C926.

[6] J.S. Moodera, G. Mathon, Journal of Magnetism and Magnetic Materials 200 (1999) 248.

[7] W.F. Brinkman, R.C. Dynes, J.M. Rowell, Journal of Applied Physics 41 (1970) 1915.

[8] C.H. Shang, J. Nowak, R. Jansen, J.S. Moodera, Physical Review B 58 (1998) R2917.

[9] S. Ikeda, J. Hayakawa, Y. Ashizawa, Y.M. Lee, K. Miura, H. Hasegawa, M. Tsunoda, F. Matsukura, H. Ohno, Applied Physics Letters 93 (2008) 082508.

[10] M. Bowen, V. Cros, F. Petroff, A. Fert, C.M. Boubeta, J.L. Costa-Kramer, J.V. Anguita, A. Cebollada, F. Briones, J.M. de Teresa, L. Morellon, M.R. Ibarra, F. Guell, F. Peiro, A. Cornet, Applied Physics Letters 79 (2001) 1655.

[11] C. Tiusan, F. Greullet, M. Hehn, F. Montaigne, S. Andrieu, A. Schuhl, Journal of Physics: Condensed Matter 19 (2007) 165201.

[12] T.-S. Kim, Physical Review B 72 (2005) 024401.

[13] S. Mukhopadhyay, I. Das, Physical Review Letters 96 (2006) 026601.

[14] J.-W. Yoo, H.W. Jang, V.N. Prigodin, C. Kao, C.B. Eom, A.J. Epstein, Synthetic Metals 160 (2010) 216.

[15] S. Sanvito, Nat Phys 6 (2010) 562.

[16] A.K. Mahapatro, R. Agrawal, S. Ghosh, Journal of Applied Physics 96 (2004) 3583.

[17] W. Xu, G.J. Szulczewski, P. LeClair, I. Navarrete, R. Schad, G. Miao, H. Guo, A. Gupta, Applied Physics Letters 90 (2007) 072506.

[18] Z.H. Xiong, D. Wu, Z. Valy Vardeny, J. Shi, Nature 427 (2004) 821.

[19] C. Tiusan, M. Sicot, M. Hehn, C. Belouard, S. Andrieu, F. Montaigne, A. Schuhl, Applied Physics Letters 88 (2006) 062512.

[20] X.G. Zhang, W.H. Butler, A. Bandyopadhyay, Physical Review B 68 (2003) 092402.

[21] T.S. Santos, J.S. Lee, P. Migdal, I.C. Lekshmi, B. Satpati, J.S. Moodera, Physical Review Letters 98 (2007) 016601.

[22] T.L.A. Tran, T.Q. Le, J.G.M. Sanderink, W.G. van der Wiel, M.P. de Jong, Advanced Functional Materials 22 (2012) 1180.

[23] J.J.H.M. Schoonus, P.G.E. Lumens, W. Wagemans, J.T. Kohlhepp, P.A. Bobbert, H.J.M. Swagten, B. Koopmans, Physical Review Letters 103 (2009) 146601.

[24] J.-W. Yoo, H.W. Jang, V.N. Prigodin, C. Kao, C.B. Eom, A.J. Epstein, Physical Review B 80 (2009) 205207.

[25] Y. Liu, T. Lee, H.E. Katz, D.H. Reich, Journal of Applied Physics 105 (2009) 07C708.

[26] H. Vinzelberg, J. Schumann, D. Elefant, R.B. Gangineni, J. Thomas, B. Buchner, Journal of Applied Physics 103 (2008) 093720.

[27] F. Borgatti, I. Bergenti, F. Bona, V. Dediu, A. Fondacaro, S. Huotari, G. Monaco, D.A. MacLaren, J.N. Chapman, G. Panaccione, Applied Physics Letters 96 (2010) 043306.

[28] W. Xu, J. Brauer, G. Szulczewski, M.S. Driver, A.N. Caruso, Applied Physics Letters 94 (2009) 233302.

Chapter 5

CONCLUSION AND FUTURE WORK

5.1 Conclusion

Magnetotransport properties of Alq_3, CuPc, ZnPc and Znq_2 based hybrid organic spin valves and the interfacial quality of the organic/ferromagnet and organic/insulator ferromagnet multilayers have been studied. The magnetotransport studies showed that the MR observed in organic based devices is due to the tunneling. In the tunneling process, electrons lose their spin polarization in some extent as they pass in and out of the organic barrier but the devices still exhibit useful MR at room temperature. However, spin polarized transport is reduced whenever the multi-step tunneling occurs in the organic layer. Alq_3-based devices showed only a few percent MR at room temperature in this regime, whereas CuPc, ZnPc and Znq_2 based devices did not yield any MR at room temperature when t = 1 nm. At low temperature, down to ~ 15 K, the spin diffusion length in these organic materials was found to be a few nanometres (~ 3 nm) due to the multi-step tunneling in the thick organic barriers.

The FFTM studies showed that there was a magnetic dead layer between the organic/ferromagnet interface, which can change the interface spin polarization of the ferromagnetic layers. However, thickness of the dead layer can be reduced when a thin

insulator layer is introduced between the organic and ferromagnetic layers. Also, the results showed that bottom ferromagnetic layer can be oxidized through the organic layer when the ferromagnetic/organic layer is exposed to air atmosphere. This is a crucial point as far as the performance of organic based devices is concerned, suggesting that UHV conditions in the thin film deposition process provides better device performance.

5.2 Future work

The field of organic spin electronics still in its early stage. Discrepancies between the literature data in terms of the spin injection, detection and dynamics have not yet been clearly understood. More reproducible data are needed in order to better understand the spin dynamics in organic semiconductors. Improving the spinterface science plays an important role for the future research. The major problem is to inject the spin polarized carriers from a buried interface. If the electrons were injected from a smooth interface, the spin dynamics would then be investigated in a more reliable way.

In terms of the future work, our first aim is to improve the organic/ferromagnet or organic/insulator/ferromagnet interfaces. There are different strategies to accomplish this. Firstly, in order to produce a good interface the substrate must be cooled before depositing the ferromagnetic electrode on the organic barriers. In this method, the aim is to freeze the metal atoms on the organic layer, which blocks the interdiffusion. We are currently redesigning the substrate holder in the organic UHV chamber to enable substrate cooling. Furthermore, some calibration experiments are planned to deposit the

metal layers at high deposition rates. Here, the aim is to form the metal layer with larger aggregates which are less mobile and diffuse a little into the organic barrier. Also, soft deposition of the metal layers onto the organic barrier in argon atmosphere is the other strategy which we need to try. In addition, we are planning to fabricate organic spin valves in a lateral geometry instead of vertical one, which eliminates the metal diffusion problem into the organic layer. Here, the basic idea is to create a nano gap between the ferromagnetic electrodes and deposit organic film on that gap. Finally, to study the spin polarized transport in the organic single crystals is the most attractive future work.